Advances in Single-Sided NMR of Polymer and Cultural Heritage Science

Von der Fakultät für Mathematik, Informatik und Naturwissenschaften der RWTH Aachen University zur Erlangung des akademischen Grades eines Doktors der Naturwissenschaften genehmigte Dissertation

vorgelegt von

M.Sc. Antonio Marchi Netto
aus São Carlos, Brasilien

Berichter:
Universitätsprofessor Dr. rer. nat. Dr. h.c. Bernhard Blümich
Universitätsprofessor Dr. rer. nat. Marcel Liauw

Tag der mündlichen Prüfung: 26. September 2014

Berichte aus der Chemie

Antonio Marchi Netto

Advances in Single-Sided NMR of Polymer and Cultural Heritage Science

Shaker Verlag
Aachen 2014

Bibliographic information published by the Deutsche Nationalbibliothek

The Deutsche Nationalbibliothek lists this publication in the Deutsche Nationalbibliografie; detailed bibliographic data are available in the Internet at http://dnb.d-nb.de.

Zugl.: D 82 (Diss. RWTH Aachen University, 2014)

Printed in Germany.

ISBN 978-3-8440-3554-4

Shaker Verlag GmbH • P.O. Box 101818 • D-52018 Aachen
Phone: 0049/2407/9596-0 • Telefax: 0049/2407/9596-9
Internet: www.shaker.de • e-mail: info@shaker.de

I hereby declare that I have created this work completely on my own and used no other sources or tools than the ones listed, and that I have marked any citations accordingly.

Hiermit versichere ich, dass ich die vorliegende Arbeit selbständig verfasst und keine anderen als die angegebenen Quellen und Hilfsmittel benutzt sowie Zitate kenntlich gemacht habe.

Porto Alegre, Rio Grande do Sul, Brazil - 23 July 2014

Antonio Marchi Netto

"The pursuit of truth and beauty is a sphere of activity in which we are permitted to remain children all our lives."

Albert Einstein

Abstract

The advent of mobile and single-sided NMR enabled performance of non-destructive and non-invasive analysis, boosting NMR experiments in polymer and cultural heritage sciences. Relying on arrangements of permanent magnets, this technology is not as expensive as conventional NMR and supports possibilities of measuring different parts of a heterogeneous sample. The available techniques for assessment of re-crystallization as evidence of thermal fusion in joints of PE pipes or the evaluation of polymer cross-link density heretofore required sample destruction or expensive methodology in order to generate accurate conclusions; unilateral NMR can easily provide good results. The depth-dependent monomer mobility in a photo-curing reaction could also be explored with single-sided sensors to probe the reaction kinetics with spatial resolution. Many studies in the field of cultural heritage, such as the evaluation of damaged stone artifacts, must be carried out *in situ,* which is possible using single-sided NMR devices. Analysis of the degradation state of ancient paper and parchment, as well evaluations of canvas conditions from easel paintings and studies of ancient pottery, require fully non-invasive methodology. This work proposes innovative utilization of a single-sided sensor, the *NMR-MOUSE,* to ascertain crystallization, cross-linking and real-time curing observations of polymers and to evaluate a new self-developed inorganic dispersion solution for restoring degraded stones, to detect elementary composition in old pottery, to characterize the damage level of parchments and handmade Chinese paper and, finally, to characterize techniques for canvas reinforcement. It was possible to detect the increase of crystallization generated by a cold-fusion process and the increase in cross-link density of polyethylene created by absorption of β radiation, and also understanding spatiotemporally the photo-curing process of dental resins. Another result indicates changes in porosity of stones due to consolidation and helps to identify the optimum treatment. Furthermore, the transverse magnetization decay in ancient pottery showed excellent correlation with the iron quantity and good correlation with the carbon content. Experiments with damaged parchment revealed details of aging, particularly through the use of an innovative two-dimensional NMR experiment. Through a relaxation experiment, it was noted that ancient hemp paper is the kind of paper least sensitive to aging, followed by rice paper and bamboo paper, the most aging-sensitive. Several analyses were made with the help of multivariate data analysis, mainly partial least square (PLS), a robust method that reduces the number of variables. In sum, this thesis explores the NMR-MOUSE sensor as a tool for studying spin relaxation of polymer and cultural heritage samples and supports the feasibility of data processing by exponential curve-fitting, inverse Laplace transformation and multivariate data analysis.

key-words: *NMR-MOUSE*; *single-sided NMR*; *polymers*; *cultural heritage.*

"A saudade que se guarda das coisas da vida,

que a gente gozou,

pode inté se arrelembrar,

tantas coisas velhas que já se passou,

quanto mais passado o tempo,

mais o amor aumenta,

mais saudade vem,

mode a gente arrelembrar,

dos amor querido que a gente quis bem."

Dominguinhos

not dedicated to the saudade...

Contents

1. Introduction

Since the discovery of *spin* by Stern and Gerlach [1] and with improvements in measuring magnetic moments made by Bloch [2] and Purcell [3], nuclear magnetic resonance (NMR) has achieved fundamental importance in science. NMR has already been recognized in conjunction with four Nobel prizes: Bloch and Purcell, in 1952; Ernst in 1991; Wüthrich in 2002 and Mansfield and Lauterbur in 2003.

In the early 1990's, almost all NMR researchers were working on techniques to increase magnetic field homogeneity, designing more and more complex NMR systems. Taking the opposite direction, two researchers at the Max Planck Institute for Polymer Research in Mainz (Germany), Blümler and Blümich, in 1993 returned to the work of Jackson et al. [4] and took the first steps toward building a portable NMR device [5]. They realized that homogenous fields were sometimes not required, and even an inhomogeneous magnetic field could distinguish among heterogeneous regions of soft matter. Such a system was born at the Rheinisch-Westfälische Technische Hochschule Aachen (RWTH Aachen University, Germany) in 1996. For its resemblance to a computer mouse in its mobility for scanning objects, it was baptized NMR-MOUSE, for *n*uclear *m*agnetic *r*esonance *mo*bile *u*niversal *s*urface *e*xplorer [5, 6].

The great advantage of their discovery was the possibility of non-destructive exploration inside arbitrary-sized objects. Now the magnet could be taken to the sample, rather than the sample to the magnet, as in conventional NMR. However, the inhomogeneous magnetic field would provide relaxation analysis of the magnetization in materials [5–7].

The sensitive volume of an NMR-MOUSE is well defined, so layers at different depths can be accessed, up to few centimeters deep. By shifting the relative MOUSE-sample distance, different layers of a sample can be revealed with different magnetization characteristics [8]. More recently, advances in the NMR-MOUSE magnetic field have enabled acquisition of sample chemical information [9] and imaging [10].

Different domains of a semi-crystalline polymer have different behaviors in a magnetic field [11, 12]. Such capacity can provide information about cross-link densities in rubber or the degree of environmental degradation of polymers. This work will present

new results from measuring NMR relaxation; evaluating the re-crystallization degree of the heat fusion joining process, used to connect two different pipes' ends (section 4.1.1); ascertaining differences in cross-link density of polyethylene samples with few differences of absorbed β-radiation (section 4.1.2) and judging capabilities of the NMR-MOUSE following depth and time-dependent photo-polymerization reactions (section 4.1.3).

Working with samples of interest to cultural heritage science requires non-destructive analysis, minimal human intervention and no changes in the material. Single-sided NMR sensors easily meet these conditions [13]. With the help of the NMR-MOUSE, painting layers could be explored with non-invasive methodology [14–17], and degraded paper and photo-papers [18–20] and parchments [21–23] could be analyzed without damaging fragile materials. Also, significant results were obtained evaluating preservation methodology for sculptures [24–27] and investigating a well-preserved Neolithic mummy, Oetzi, the Iceman [28]. The coming chapters will describe some new investigations in the cultural heritage field, such as evaluation of a new re-filling consolidation process for remedying damaged sandstones (section 4.2.1), correlation of elementary composition with magnetization decay in ancient potteries (section 4.2.2), a study of NMR relaxometry in damaged parchments (section 4.2.3), a discriminate experiment in ancient Chinese paper (section 4.2.4) and identifying the lining or reinforcement with canvas of easel paintings from a second layer (section 4.2.5).

All the experiments were performed with the NMR-MOUSE, so they were non-invasive and did not require sample destruction. The acquired data were explored using methods such as data fitting, inverse Laplace transform and robust data evaluation provided by multivariate data analysis (Appendix A).

1.1 NMR

1.1.1 Overview

In 1922, while conducting an electron scattering experiment, Otto Stern and Walther Gerlach realized that a gradient magnetic field could induce level separation in an electron beam. A new physical quantity of angular momentum was found and labeled *spin*. This experiment is called the *Stern-Gerlach* experiment [1]. Three years later, Wolfgang Pauli announced his exclusion principle and introduced the spin concept [29].

In the following years, researchers made great strides in evaluating magnetic moments. Isidor Isaac Rabi and collaborators noticed in 1939 that some hydrogen nuclei,

in the presence of a gradient magnetic field and a high vacuum, had an absorption preference for particular radio frequencies. This experiment is considered to constitute the discovery of nuclear magnetic resonance (NMR), and for this reason Rabi was awarded the Nobel Prize in Physics for the year 1944 [30].

Further, Felix Bloch [2], independently and simultaneously with Edward Purcell [3], worked on improving techniques to measure nuclear magnetic moments in condensed matter. They developed an accurate, purely electromagnetic procedure for measuring nuclear induction, which earned them a shared Nobel Prize in Physics for the year 1952. However, the effect called chemical shift had already been reported in 1950, by Dickinson [31] and Proctor and Yu [32]. Bloch spent the rest of his life developing understanding of the NMR phenomenon.

During the second half of the twentieth century NMR sensitivity greatly increased with the advent of pulsed NMR with the use of the Fourier transform, realized by Ernst and Anderson in 1965 [33]. For this work, Ernst was honored with the Nobel Prize in Chemistry for the year 1991. Subsequently, Kurt Wüthrich refined a multidimensional approach that found success in evaluating protein structures [34], earning half of the Nobel Prize in Chemistry for the year 2002. Moreover, Peter Mansfield and Paul Lauterbur explored magnetic gradients, discovering magnetic resonance imaging (MRI) [35], and were together awarded the Nobel Prize in Physiology or Medicine in 2003. MRI represents the greatest advance in medical imaging since the discovery of X-rays by Wilhelm Roentgen in 1895.

Today NMR is well established, although still developing. New talents regularly appear in the NMR research field. NMR applications are notable in physics, chemistry, pharmacy, medicine, biophysics and biochemistry, and include applications for solid, liquid and gas states. These applications can be divided into three large sub-areas of NMR:

- *Spectroscopy*: provides chemical information about the sample;
- *Imaging*: explores heterogeneity on a macroscopic scale;
- *Relaxometry*: gives information about the physical properties of the sample at the molecular level.

Even though all sub-areas arose from Bloch's work [2], relaxometry is the oldest. However, with new developments in recent years and applications to porous media and the oil industry, it has experienced a revival, and is now the sub-area with the highest increment rate of works and publications [36].

1.1.2 Classical view of NMR

As mentioned in section 1.1.1, Bloch and Purcell verified that some nuclei absorbed only a certain radio frequency ω_0, called the *Larmor* frequency, the nuclei are aligned to the magnetic field $\mathbf{B}_0$ in a frequency proportional to the nucleus-dependent constant γ. With μ_0 as the respective magnetic momentum, the Hamiltonian of the interaction is [37, 38]:

$$\widehat{\mathcal{H}}_0 = -\mu_0 \cdot \mathbf{B}_0 \tag{1.1}$$

The magnetic momentum can still be replaced in terms of γ, the Planck constant $\hbar$ and the spin vector to $\mathbf{B}_0$ ($\mu_0 = \gamma\hbar\mathbf{I}_z$), resulting in:

$$\widehat{\mathcal{H}_0} = -\gamma\hbar\mathbf{I_z} \cdot \mathbf{B}_0 \tag{1.2}$$

In case of spin $1/2$, the eigenvalues suggest the following transition energy:

$$\Delta\mathtt{E} = -\gamma\hbar\,|\mathbf{B_0}| \tag{1.3}$$

from which, applying the Bohr condition:

$$\omega_0 = \gamma\,|\mathbf{B_0}| \tag{1.4}$$

The Larmor frequency is the NMR resonance frequency. Spin degeneration is induced by $\mathbf{B}_0$, then forced to transition between the energy levels by a second magnetic field, $\mathbf{B}_1$, with the same frequency. If $\mathtt{k_B}$ is the Boltzmann constant and T the temperature, the ratio between the spin population at the high (α) and low (β) energy levels is calculated through Boltzmann statistics:

$$\frac{N_\alpha}{N_\beta} = \mathtt{exp}\left(-\frac{\gamma\hbar\,|\mathbf{B_0}|}{\mathtt{k_B}T}\right) \tag{1.5}$$

The magnetic fields in NMR are usually a few Tesla in strength, which determine the range of radio frequency waves (RF) and several special characteristics. Radio waves can be created using simple electronics while still maintaining precision. As a consequence, the uncertainty in the wave frequency must be less than the width of the induced transition levels $\Delta\mathtt{E}/2\mathtt{h}$. The low energy of each photon $\mathtt{h}\nu$ and the narrow spectral width $\Delta\nu$ obtained make a low RF power enough to generate an astronomical number of photons per frequency unit. This means that NMR is basically governed by induced emission, which does not require quantum treatment [37, 38].

Moreover, each component of the RF electrical-magnetic field has a well-defined phase ϕ. Being $\mathtt{n}$ the respective number of photons, high for the radio waves, the uncertainty principle implies $\Delta\mathtt{n}\Delta\phi \approx 1$. This fact enables us to define the amplitude and phase of a RF wave together without contradicting the uncertainty principle.

Felix Bloch introduced an interpretation based on classical mechanics, the *Bloch equations*, in which the macroscopic magnetization $\mathbf{M}$ is understood as a sum over all the microscopic magnetic moments μ_0. The potential energy and torque are, respectively:

$$\mathtt{V} = -\mathbf{M} \cdot \mathbf{B_0} \tag{1.6}$$

$$\tau = \mathbf{M} \times \mathbf{B_0} \tag{1.7}$$

Including the relaxation effects to Eq. 1.7, and after some replacements, the differential Bloch equation at the laboratory frame is:

$$\frac{\mathbf{d}M}{\mathbf{dt}} = \gamma\left(M \times \mathbf{B_0}\right) - \left(\frac{M_\mathtt{x}\mathbf{x} + M_\mathtt{y}\mathbf{y}}{T_2} + \frac{M_\mathtt{z} - M_0}{T_1}\mathbf{z}\right) \tag{1.8}$$

where $M_\mathtt{x}$ and $M_\mathtt{y}$ are the transverse magnetization components at the respective axes $\mathbf{x}$ and $\mathbf{y}$, $M_\mathtt{z}$ is the component at the longitudinal axis $\mathbf{z}$ and M_0 is the magnetization of thermal equilibrium.

In 1948, Bloembergen and co-authors described the existence of two independent relaxation processes in magnetization [39], which need to be included in Eq. 1.7. They are:

- The *longitudinal* or *spin-lattice* relaxation time T_1, which characterizes the returning of the magnetization to the thermal equilibrium, in the direction of $\mathbf{B}_0$. This is an enthalpy phenomenon.
- The *transverse* or *spin-spin* relaxation time T_2, which relates to the loss of magnetization in the directions perpendicular to $\mathbf{B}_0$. This is an entropic phenomenon.

They proposed a model, known as the Bloembergen-Purcell-Pound model, or by the acronym *BPP model*, that can predict relaxation times depending on a correlation time characteristic of Brownian motion, $\tau_\mathtt{c}$ [39]:

$$\frac{1}{T_1(\tau_c)} = \frac{3}{10}\left(\frac{\mu_0}{4\pi}\right)^2 \frac{\gamma^4\hbar^2}{r^6}\left[\frac{\tau_\mathtt{c}}{1+\omega_0^2\tau_\mathtt{c}^2} + \frac{4\tau_\mathtt{c}}{1+4\omega_0^2\tau_\mathtt{c}^2}\right] \tag{1.9}$$

$$\frac{1}{T_2(\tau_\mathtt{c})} = \frac{3}{20}\left(\frac{\mu_0}{4\pi}\right)^2 \frac{\gamma^4\hbar^2}{r^6}\left(\frac{3\tau_\mathtt{c}}{1+\Delta\omega^2\tau_\mathtt{c}^2} + \frac{5\tau_\mathtt{c}}{1+\omega_0^2\tau_\mathtt{c}^2} + \frac{2\tau_c}{1+4\omega_0^2\tau_c^2}\right) \tag{1.10}$$

where r means the distance between two nuclear magnetic moments. This model is able to predict both relaxation times: T_1 has a minimum value when τ_c^{-1} is equal to the Larmor frequency; T_2 only decreases when decreasing the movement. The relaxation time's dependence on τ_c is plotted according to Fig. 1.1.

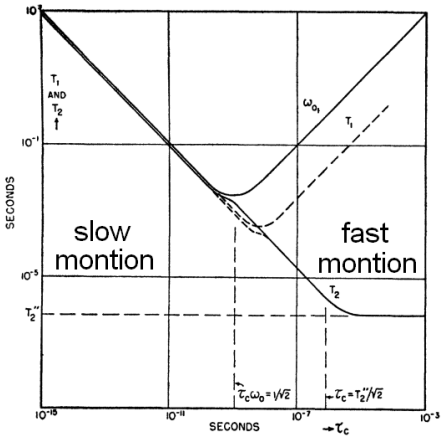

FIGURE 1.1: T_1 and T_2's dependence on τ_c following the BPP theory[39].

A simplification in the Bloch equations comes when Eq. 1.8 is seen through a rotational frame, with frequency $\mathbf{\Omega}$:

$$\frac{\mathbf{d}M_{\mathtt{rot}}}{\mathbf{d}t} = \gamma\left(M \times \mathbf{B_{eff}}\right) - \left(\frac{M_{\mathtt{x}}\mathbf{x} + M_{\mathtt{y}}\mathbf{y}}{T_2} + \frac{M_{\mathtt{z}} - M_0}{T_1}\mathbf{z}\right) \tag{1.11}$$

with the new effective magnetic field being $\mathbf{B}_{\text{eff}} = \mathbf{B}_0 + {}^{\mathbf{\Omega}}/_{\gamma}$. Supposing the second magnetic field $\mathbf{B}_1$ is in the direction $\mathbf{x}$, Peter Mansfield [40] suggests more substitutions:

$$\mathbf{B_{eff}} = \mathbf{B}_1\mathbf{x} + \mathbf{B}_0\mathbf{z} \tag{1.12}$$

$$\Delta\omega = \gamma\left|\mathbf{B_0} - \frac{\mathbf{\Omega}}{\gamma}\right| = \left|\omega_{\mathbf{0}} - \mathbf{\Omega}\right| \tag{1.13}$$

$$\omega_1 = \gamma\left|\mathbf{B_1}\right| \tag{1.14}$$

leading to a vectorial form of the Bloch equations:

$$\frac{\mathbf{d}M}{\mathbf{d}t} = \widehat{\mathtt{D}}M + \frac{\mathbf{M_0}}{T_1} \tag{1.15}$$

with the vectors and matrix given by:

$$M = \begin{pmatrix} M_{\mathtt{x}} \\ M_{\mathtt{y}} \\ M_{\mathtt{z}} \end{pmatrix} \tag{1.16}$$

$$M_{\mathbf{0}} = \begin{pmatrix} 0 \\ 0 \\ M_0 \end{pmatrix} \tag{1.17}$$

$$\widehat{\mathtt{D}} = \begin{pmatrix} -1/T_2 & \Delta\omega & 0 \\ -\Delta\omega & -1/T_2 & \omega_1 \\ 0 & -\omega_1 & -1/T_1 \end{pmatrix} \tag{1.18}$$

Considering relaxation, precession and pulse as independent phenomena, and defining:

$$E_{1,2}(t) = \mathtt{exp}\left(\frac{-t}{T_{1,2}}\right) \tag{1.19}$$

Equation 1.15 is solved, resulting in:

$$M(t) = \mathtt{exp}\left(\widehat{A}t\right)\mathtt{exp}\left(\widehat{T}t\right)M(0) + M_{\mathbf{0}}\left(1 - E_1(t)\right) \tag{1.20}$$

where

$$\widehat{A} = \begin{pmatrix} 0 & \Delta\omega & 0 \\ -\Delta\omega & 0 & \omega_1 \\ 0 & -\omega_1 & 0 \end{pmatrix} \tag{1.21}$$

$$\widehat{T} = \begin{pmatrix} -1/T_2 & 0 & 0 \\ 0 & -1/T_2 & 0 \\ 0 & 0 & -1/T_1 \end{pmatrix} \tag{1.22}$$

By simplicity, a real approximation is arrived at by considering very short radio-frequency pulses with a time $T_{\mathtt{p}}$, resulting in a flip angle α ($= \omega_1 \mathtt{T_p}$), independent of relaxation or precession effects. This leads to independent matrices for pulsing $\widehat{R}_{\mathtt{x}}(t)$, precessing $\widehat{R_{\mathtt{z}}}(t)$ and relaxation $\widehat{E}(t)$:

$$\widehat{R}_{\mathtt{x}}(\alpha) = \begin{pmatrix} 1 & 0 & 0 \\ 0 & \cos(\alpha) & \sin(\alpha) \\ 0 & -\sin(\alpha) & \cos(\alpha) \end{pmatrix} \tag{1.23}$$

$$\widehat{R}_{\mathtt{z}}(t) = \begin{pmatrix} \cos(\Delta\omega t) & \sin(\Delta\omega t) & 0 \\ -\sin(\Delta\omega t) & \cos(\Delta\omega t) & 0 \\ 0 & 0 & 1 \end{pmatrix} \tag{1.24}$$

$$\widehat{E}(t) = \begin{pmatrix} E_2(t) & 0 & 0 \\ 0 & E_2(t) & 0 \\ 0 & 0 & E_1(t) \end{pmatrix} \tag{1.25}$$

This group of equations is enough to describe any phenomenon dependent only on excitation, relaxation and precession. Diffusion can be easily added to the transverse components. The case of a single RF pulse followed by precession and relaxation (free induction decay - FID) is written:

$$M(t) = \widehat{R}_{\mathtt{z}}(\Delta\omega t)\,\widehat{E}(t)\,\widehat{R}_{\mathtt{x}}(\alpha)\,M(0) + M_0(1 - E_1(t)) \tag{1.26}$$

Solved to:

$$\begin{pmatrix} M_{\mathtt{x}}(t) \\ M_{\mathtt{y}}(t) \\ M_{\mathtt{z}}(t) \end{pmatrix} = \begin{pmatrix} M_0 \mathtt{exp}\left(-t/T_2\right)\sin(\Delta\omega t)\sin(\alpha) \\ M_0 \mathtt{exp}\left(-t/T_2\right)\cos(\Delta\omega t)\sin(\alpha) \\ M_0\left[1 + \mathtt{exp}\left(-t/T_1\right)(\cos(\alpha) - 1)\right] \end{pmatrix} \tag{1.27}$$

An FID for T_1 of 100 s, T_2 of 50 ms, $\Delta\omega$ of 50 Hz and pulse α of 90° RF pulse in a homogeneous magnetic field results in the decay of magnetization as presented in Fig. 1.2.

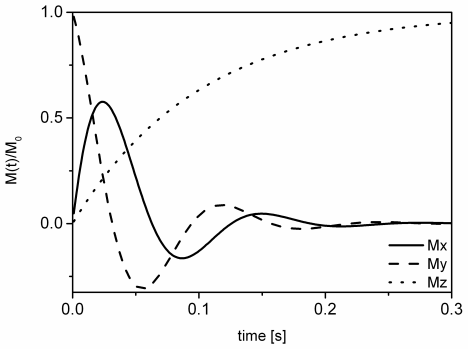

FIGURE 1.2: Free induction decay.

In real experiments, the FID decays faster due to inhomogeneities in $\mathbf{B}_0$. The characteristic time is called T_2^*, defined as:

$$\frac{1}{T_2^*} = \frac{1}{T_2} + \Delta\left|\mathbf{B}_0\right| \tag{1.28}$$

where $\Delta\mathbf{B_0}$ is the inhomogeneity across a voxel.

1.1.3 Relaxation

Different relaxation times allow for several sequences for measuring within the scope of NMR relaxometry. The success of these measurements arises from the possibility of *echo* formation. Historically, T_2 was initially more explored. Examples of pulse sequences are the spin-echo, the Carr-Purcell (CP [41]), the Carr Purcell Meiboom Gill (CPMG [42]) and the Ostroff-Waught (OW4 [43]) pulse sequences. Inversion recovery (IR [44]) and

saturation-recovery (SR [45]) are examples of pulse sequences for T_1 measurements. The following paragraphs present a short discussion focused on sequences of interest in NMR relaxometry.

T_2

Experiments for determining the transverse magnetization rate constant have become increasingly sophisticated. Hahn documented the spin-echo phenomenon; Carr and Purcell explained the feasibility of multi-echo acquisition in a single experiment and Meiboom and Gill changed a pulse phase, improving the accuracy of the Carr and Purcell sequence. Ostroff and Waugh proposed a particular case of the Meiboom and Gill sequence with benefits to experiments in the solid state of matter.

Hahn-echo sequence

Hahn noticed that applying a second RF pulse could compensate for inhomogeneity effects (Eq. 1.28) by refocusing the lost coherence of the magnetization [46]. The Hahn-echo (or spin-echo) sequence (SE) consists of two RF pulses with duration $\mathtt{t_w}$ and phase $\mathbf{x}$ spaced by a time τ. The echo is formed at a time τ after the second pulse (Fig. 1.3(a)). Through private communication, Purcell proposed a three-dimensional model of the echo. If the magnetization is in thermal equilibrium (Fig. 1.3(b) A) and $\omega_1\mathtt{t_w}$ results in a 90° pulse (Fig. 1.3(b) B), the magnetization spreads over a time τ (Fig. 1.3(b) C); the second 90° pulse (Fig. 1.3(b) D) after another time τ (Fig. 1.3(b) E) recovers the coherence (Fig. 1.3(b) F), similar to a figure eight. T_2 values could be extracted by measuring echoes at different values of τ. In the formulation of Eqs. 1.23 to 1.25, the magnetization resulting from a Hahn-echo pulse sequence is:

$$M_{\mathtt{SE}}\left(2\tau\right) = M_0 \mathtt{exp}\left(\frac{-2\tau}{T_2}\right) \tag{1.29}$$

Carr-Purcell sequence

In 1954, Carr and Purcell realized that the long time needed between each measurement with the Hahn-echo sequence ($5T_1$) could be avoided. They proposed a new methodology for measuring (T_2), today know as the Carr-Purcell (CP) pulse sequence, which is based on the application of a first 90° pulse at $t = 0$ and a second 180° pulse at a time $t = \tau$, leading to an echo generation at $t = 2\tau$. Their improvement came by inserting a third 180° RF pulse $t = 3\tau$, which refocuses the magnetization at $t = 4\tau$, generating the second echo. This method is repeated until the transverse magnetization vanishes (Fig. 1.4) [41]. In the formulation of Eqs. 1.23 to 1.25, and with $T_{\mathtt{E}}$ being the time between two sequent echoes, or echo time ($T_{\mathtt{E}} = 2\tau$), the magnetization value for the n$^{\mathrm{th}}$ echo is:

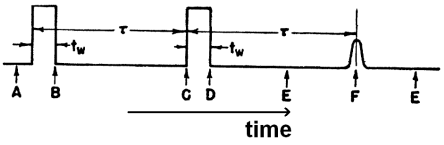

(a)

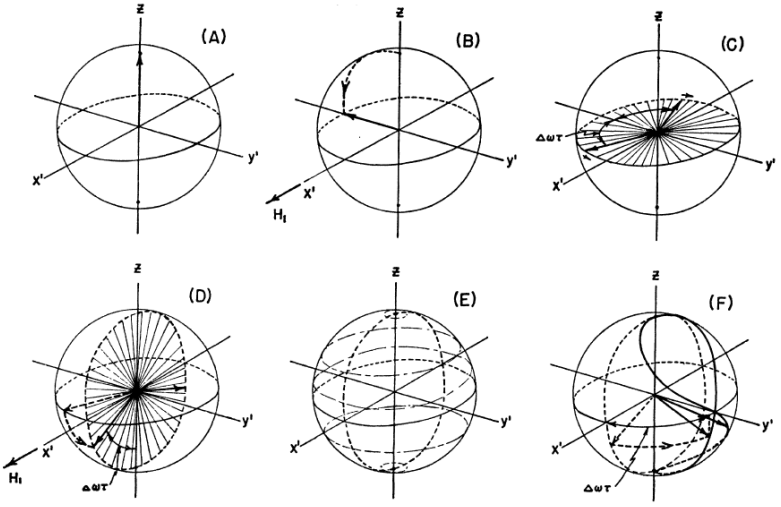

(b)

FIGURE 1.3: The Hahn-echo [46]. (a) Hahn-echo pulse sequence. (b) Eight-ball echo pattern.

$$M_{\mathtt{CP}}\left(nT_{\mathtt{E}}\right) = (-1)^n M_0 \mathtt{exp}\left(\frac{nT_{\mathtt{E}}}{T_2}\right) \tag{1.30}$$

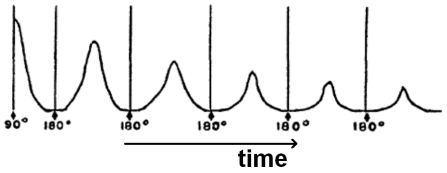

FIGURE 1.4: The Carr-Purcel (CP) pulse sequence [41].

Meiboom-Gill modification

While exploring the CP sequence in 1958, Meiboom and Gill realized that such a sequence had low reproducibility, mainly due to imperfections in the 180° RF pulse, where a small deviation would bring cumulative errors. As a remedy, they suggested a 90° phase shift between the 90° and the 180° RF pulse in the CP sequence, so all the echoes became positive and formed at the same axis (as seen in Fig. 1.5) [42]. The modified sequence is known as the Carr-Purcell-Meiboom-Gill (CPMG) pulse sequence and provides magnetization of the form:

$$M_{\mathtt{CPMG}}\left(nT_{\mathtt{E}}\right) = M_0 \mathtt{exp}\left(\frac{nT_{\mathtt{E}}}{T_2}\right) \tag{1.31}$$

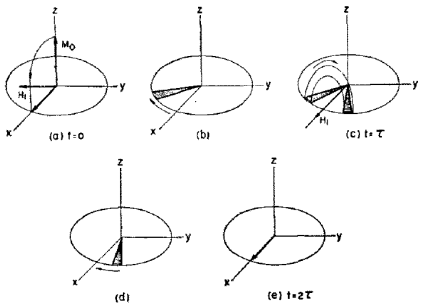

FIGURE 1.5: The Carr-Purcell-Meiboom-Gill (CPMG) pulse sequence [42].

Ostroff-Waught sequence

After perceiving the existence of an anomalous effect when studying a long train of CPMG echoes applied in ^{19}F resonance for a K_2SiF_6 solid sample, which was maximized when all the CPMG pulses were 90°, Ostroff and Waugh [43] understood the experiment as a train of solid-echoes (also called quadrupole-echoes) previously explained by Powles and Strange [47]. This sequence is called the OW4 pulse sequence and provides magnetization with modulus similar to the CPMG pulse sequence:

$$\mathbf{M}_{\mathtt{OW4}}\left(nT_{\mathtt{E}}\right) = \mathbf{M}_0 \mathtt{exp}\left(\frac{nT_{\mathtt{E}}}{T_2}\right) \tag{1.32}$$

$\boldsymbol{T}_1$

Pulse sequences for measuring T_1 mainly consist of a preparation time, allowing the spins to recover their thermal equilibrium, followed by an encoding pulse, when the spins are labeled, followed by a third RF pulse, applied in order to read the previous encoding. Two sequences to measure T_1 are cited: the inversion-recovery and the saturation-recovery pulse sequence.

Inversion-recovery sequence

Vold, Waugh, Klein and Phelps proposed the inversion-recovery (IR) pulse sequence, which consists of a first inversion RF pulse (180°) that brings the magnetization from the thermal equilibrium $\mathbf{M_0}$ to its opposite direction [44]. After an encoding time τ, a second 90° pulse is applied, enabling the evolution of the magnetization to be detected, with value:

$$M_{\mathtt{IR}}\left(\tau\right) = M_0\left(1 - 2\mathtt{exp}\left(\frac{\tau}{T_1}\right)\right) \tag{1.33}$$

Due to the exponential behavior of the recovery magnetization, it is suggested to use N logarithmic increments of the time τ until $5T_1$ [48]:

$$\tau_i = -T_1 \ln\left[1 - \frac{1 - \exp(-5)}{N-1} i\right] \tag{1.34}$$

Including the time needed to bring all the magnetization back to the thermal equilibrium, an IR experiment set with the time increments as Eq. 1.34 takes a time of $6T_1N$ [48].

Saturation-recovery sequence

Markley, Horsley and Klein realized an alternative method to the IR pulse sequence [45]. They substituted a saturation pulse (90°) for the initial inversion pulse (180°), creating the saturation-recovery (SR) pulse sequence. The measurement time is reduced and the signal-to-noise ratio is doubled because the magnetization needs only to recover from 0 to the initial value:

$$M_{\mathrm{SR}}(\tau) = M_0\left(1 - \exp\left(\frac{\tau}{T_1}\right)\right) \tag{1.35}$$

Better saturation is achieved with an odd number of saturation pulses separated by times smaller than T_2^*. Considering the possibility of recycle delay absence and time spaced as Eq. 1.34, the SR sequence takes a time T_1N. However, to reach the same signal-to-noise ratio, the SR pulse sequence is three times faster than the IR sequence in a T_1 measurement [48].

1.1.4 Laplace NMR

At the beginning of the 1990s, multidimensional Fourier NMR was well established [33, 34]; however, only in early 90's was the first work with multidimensional Laplace NMR published. This tool is able to invert relaxation curves with one or more relaxation distributions [49, 50]. With $g(R)$ as the distribution of relaxation rates ($R_n = 1/T_n$) and defined only for $R > 0$, its Laplace transform (LT) is:

$$\mathcal{L}(g(-R_n)) = \int g(R_n) \exp(R_n t)\, \mathrm{d}R_n \tag{1.36}$$

A first observation is that LT possesses stability with noise; in other words, a bit of random noise does not change the LT. A second observation is that the inverse operation, the inverse Laplace transform (ILT), is highly unstable.

One-dimensional Laplace NMR

For example, the ILT distributions $\mathcal{L}(T_1)$ of T_1 (SR experiment) and $\mathcal{L}(T_2)$ of T_2, both of them with an experimental noise $E(t)$, are given by:

$$M_{\mathtt{SR}}(t) = \int \mathcal{L}(T_1)\left[1 - \mathtt{exp}\left(\frac{-t}{T_1}\right)\right] \mathtt{d}T_1 + E(t) \tag{1.37a}$$

$$M_{\mathtt{CPMG}}(t) = \int \mathcal{L}(T_2)\,\mathtt{exp}\left(\frac{-t}{T_2}\right) \mathtt{d}T_2 + E(t) \tag{1.37b}$$

Computational algorithms can process the Inverse Laplace Discrete Transformation (ILDT), solve Eq. 1.37 and provide the $\mathcal{L}(T_1)$ and $\mathcal{L}(T_2)$ [51, 52].

Multi-dimensional Laplace NMR

The kernel distributions $\left[1 - \mathtt{exp}^{-t/T_1}\right]$ and $\left[\mathtt{exp}^{-t/T_2}\right]$ may have several relaxation time dependence in 2D Laplace NMR, resulting in multi-dimensional relaxometry, a case in which the spin system is prepared in one time variable during an encoding time and acquired in another variable [53].

Examples of bi-dimensional experiments are the Relaxation-Relaxation COrrelation SpectroscopY (RRCOSY, or T_1-T_2 correlation [49, 54]) and the Relaxation-EXchange SpectroscopY (REXSY, or $T_2 - T_2$ exchange [49, 55]). For RRCOSY, with the SR sequence encoded in τ_1 and CPMG (or OW4) encoded in τ_2, the inverse Laplace equation to be solved is:

$$M_{\mathtt{RRCOSY}}(\tau_1, \tau_2) = \int\int \left(1 - \mathtt{exp}\left(\frac{-\tau_1}{T_1}\right)\right) \mathtt{exp}\left(\frac{-\tau_2}{T_2}\right) \mathcal{L}(T_2, T_1)\,\mathtt{d}T_1\mathtt{d}T_2 + E(t) \tag{1.38}$$

The transformation algorithm was complicated and time-consuming until the advent of a fast 2D-ILT code created by Venkataraman and co-authors [56]. Figure 1.6(a) shows an example of a RRCOSY experiment and the corresponding 2D-ILT, presented in Fig. 1.6(b).

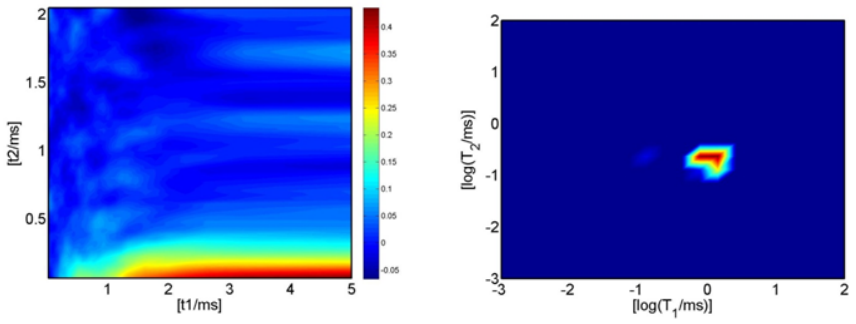

(a) (b)

FIGURE 1.6: RRCOSY data simulated with signal-to-noise ratio of 5 and T_1/T_2 of 10. (a) The simulated data. (b) The corresponding inverse Laplace transform.

1.1.5 Single-sided NMR

The first inside-out NMR experiment was reported by Jackson and co-authors in 1980. In this work the signal was collected from a toroidal region outside the NMR coil similar to Fig. 1.7 [4]. Using echoes generated by a Carr-Purcell pulse sequence, field inhomogeneity effects were reduced [41]. They also predicted several potential applications for the new well-logging NMR. Oil companies quickly recognized the potential of such a technique and developed their own devices.

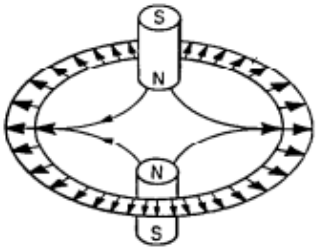

FIGURE 1.7: Jackson's magnet configuration [4].

In the course of few time, researchers had worked to improve measurements in inhomogeneous $\mathbf{B}_0$ and $\mathbf{B}_1$ and to reduce image distortions, originating, for example, the stray-field imaging (STRAFI) [57], in which the samples are analyzed in a uniform static field gradient created outside of a superconducting magnet.

The stray-field concept of well-logging NMR gained popularity for materials testing with the advent of a stray field device called MObile Universal Surface Explorer, the NMR-MOUSE [6], made with permanent magnets. Its portability enabled investigation of arbitrarily large objects in a fully non-destructive way. The first NMR-MOUSE consisted of two semi-cylindrical permanent magnets separated by 13 mm (however, this gap could be varied), fixed over an iron yoke, weighting 2.5 kg (Fig. 1.8(a)). In that configuration, $\mathbf{B}_0 = 0.5$ T and the $\mathbf{B}_1$ field were generated by a four-layer solenoid surface coil with eight turns per layer, resulting in an inductance of 3 μH.

Due the presence of many off-resonance spins, special spin dynamics characteristics come into play when measuring in an inhomogeneous field [7]. A very important characteristic is the contamination of relaxation times measured through the CPMG-like multi-echo sequences by T_1, from flip-angle distribution due to resonance offset in the inhomogeneous stray field of the sensor. With $\langle n_z^2 \rangle$ as the average projection of the magnetization vector to the z-axis during an echo time and the 180° inversion pulse ($0 \leq \langle n_z^2 \rangle \leq 1$), the measured transverse relaxation time $T_{2_{\text{eff}}}$ is:

$$\frac{1}{T_{2_{\text{eff}}}} = \frac{1}{T_2} + \left\langle n_z^2 \right\rangle \left(\frac{1}{T_1} - \frac{1}{T_2} \right) \tag{1.39}$$

Later, a second gap was inserted in the NMR-MOUSE geometry, so that the sensor was composed of four permanent magnets, with a small gap of 2 mm (d_S) between magnets with the same polarization and 14 mm of separation from the others (d_B). This new configuration generated a magnetic field of 0.4 T at 10 mm distance above the NMR-MOUSE surface (Fig. 1.8(b)), with a gradient of about 20 T/m, producing spacial resolution smaller than 5 μm [8].

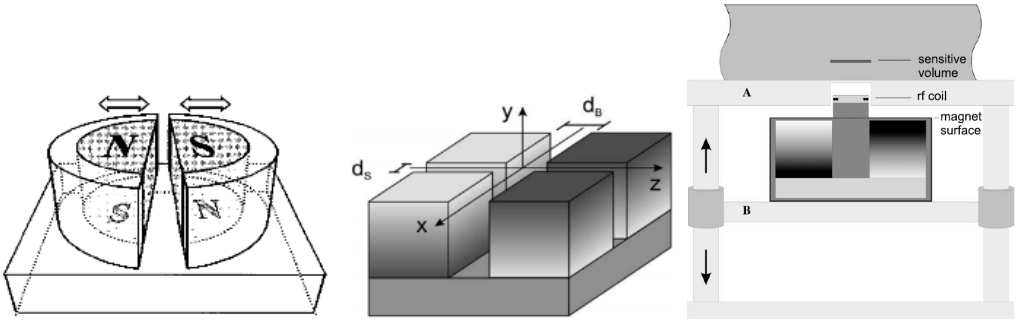

(a) (b) (c)

FIGURE 1.8: The NMR-MOUSE. (a) The first NMR-MOUSE [6]. (b) New magnet geometry [8]. (c) On a lift [8].

The sensitive volume can be moved inside the sample by keeping the NMR-MOUSE fixed and moving the sample or by keeping the sample fixed and moving the NMR-MOUSE, revealing inhomogeneity in the matter. Usually this second option makes more sense, so the NMR-MOUSE is situated on an automatic or manual lift and moved (Fig. 1.8(c)). Automatic lifts are more accurate in their step size because a computer is programmed to move the lift precisely. Furthermore, with an automatic lift a profile can be obtained over several hours without need of supervision, while a manual lift requires the user to turn a screw and move the sensor position.

The strong field inhomogeneity makes a considerable part of the magnetization relax in a short time (Eq. 1.28). Together with a delay time for acquisition, called dead time (discussed in section 3.1), the magnetization requires a single echo or a train of echoes in order to be read, leading to the known dead time weighting of the relaxation experiments. This effect is illustrated in Fig. 1.9 for an SR experiment, where the simulated magnetization is the result of a single echo or an average of four echoes, with an echo time of 0.050 ms. The experimental and predicted T_1 values are presented in Table 1.1 and clearly indicate more discrepancy in amplitude values for long averaged acquisitions and short values of T_2. It should be underlined that in inhomogeneous NMR devices it is not possible to acquire zero transverse magnetization amplitude, so the T_1 values acquired are also contaminated by field inhomogeneity.

There is also weighting in T_1 when a multi-scan experiment does not allow the repetition time (also called recycle delay) of $5T_1$ for the magnetization to return to the

TABLE 1.1: SR experiment weighted by dead time

Parameter	predicted	
	after 1 echo	mean of the 1^{st} to the 4^{th} echo
A [% of M_0] ($T_2 = 0.50$ ms)	0.90484	0.78368
T_1 [ms] ($T_2 = 0.50$ ms)	1.00	1.00
A [% of M_0] ($T_2 = 0.25$ ms)	0.81873	0.6218
T_1 [ms] ($T_2 = 0.25$ ms)	1.00	1.00

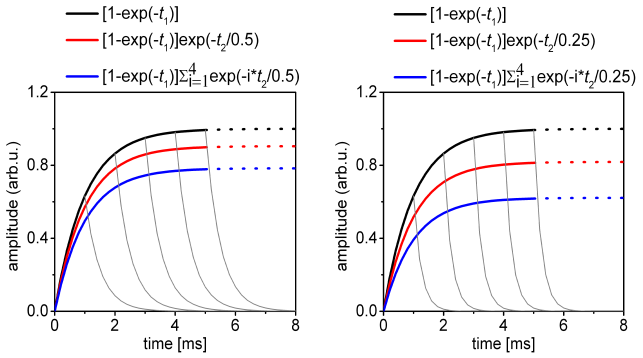

(a) (b)

FIGURE 1.9: Dead time effects in an SR experiment. (a) Weighting with $T_2 = 0.50$ ms. (b) Weighting with $T_2 = 0.25$ ms.

thermal equilibrium value. An example of this is given in Fig. 1.10, where five different CPMG trains with echo time of 0.050 ms and amplitude as mean of the first four echoes were simulated for different repetition times for two samples with the same T_2=0.5 ms but T_1= 1 or 2 ms. After many scans the magnetization is considered in a perfect steady state. Table 1.2 presents the different amplitudes weighted by the repetition times. This shows that the repetition times must be precisely set if no weighting by T_1 is desired. On the other hand, performing the same experiment with different repetition times may be useful for providing T_1 contrast, such as in the case of profiling samples with the CPMG pulse sequence.

TABLE 1.2: Amplitudes weighted by the repetition time

Rep. time [ms]	amplitude predicted [% of M_0]	
	for $T_1 = 1$ ms	for $T_1 = 2$ ms
1	54.748	34.079
2	74.888	54.748
3	82.298	67.285
4	85.023	74.888
5	86.026	79.501

If exploring a low-viscosity fluid, for example, water, a new term needs to be

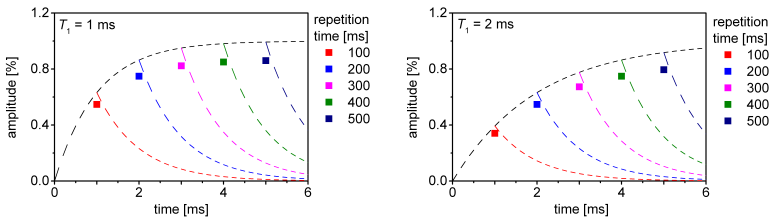

(a) (b)

FIGURE 1.10: Recovery time effects in an amplitude experiment with several scans. (a) Weighting with $T_1 = 1.00$ ms. (b) Weighting with $T_1 = 2.00$ ms.

accounted for in its transverse relaxation. With $T_{2_{\mathtt{eff}}}$ being the effective transverse relaxation time of the bulk liquid, γ being the isotope gyromagnetic constant, G being the magnetic field gradient, $T_{\mathtt{E}}$ being the calibrated echo time and D being the liquid diffusion coefficient, the transverse relaxation rate for a diffusive material $T_{2\mathtt{eff}_{\mathtt{D}}}$ is written by:

$$\frac{1}{T_{2\mathtt{eff}_{\mathtt{D}}}} = \frac{1}{T_{2\mathtt{eff}}} + \frac{1}{12}\gamma^2 G^2 T_{\mathtt{E}}^2 D \tag{1.40}$$

In the case of porous materials, an echo train is applied to acquire the transverse relaxation time that also reveals information about the liquid diffusion in the porous medium. Furthermore, a porosity term related to the surface-to-volume ratio needs to be inserted. Small pores lead to short relaxation times. With ρ being the relaxivities of the surface, S and V the porous surface and volume (respectively), this relation is represented as:

$$\frac{1}{T_{2\mathtt{eff}_{\rho}}} = \frac{1}{T_{2\mathtt{eff}}} + \rho_n \frac{S}{V} \tag{1.41}$$

The decay contribution due to the surface is much higher than the one coming from the bulk fluid, so the second term can be neglected [58].

Commonly the T_2 sequences are used to solve contrast in unilateral NMR profiles. The data can be fitted by a modelling function or parts of a pulse train can be co-added, resulting in weighted profiles. Adding echoes increases the signal-to-noise ratio and speeds up the data processing, so it is a suitable solution for complicated decays or very short relaxation times. NMR scientists proposed to sum over l echoes during a profiling experiment, as suggested in Eq. 1.42 [8]. Assuming a n phases system, if the number l of averaged echoes is few ($l = a << T_{2\mathtt{eff}}/T_{\mathtt{E}}$), Eq. 1.42 can be approximated by a Taylor series until first order and the result S_a are proportional to the magnetization (Eq. 1.43). On the other hand, if the echoes are summed until a time proportional to

five times $T_{2\mathtt{eff}}$ ($l = b >> T_{2\mathtt{eff}}/T_{\mathtt{E}}$), the quantity S_b produced is proportional to the average $T_{2\mathtt{eff}}$ (Eq. 1.44):

$$S_l = \sum_{x=1}^{l} \sum_{\mathtt{n}} M_{0_n} \exp\left(\frac{-xT_{\mathtt{E}}}{T_{2\mathtt{eff}_n}}\right) \tag{1.42}$$

$$\frac{S_a}{a} = \sum_{\mathtt{n}} M_{0_{\mathtt{n}}} \tag{1.43}$$

$$\frac{S_b}{M_0} = \frac{1}{T_{\mathtt{E}}} \sum_{\mathtt{n}} \mu_{\mathtt{n}} T_{2\mathtt{eff}_{\mathtt{n}}} \tag{1.44}$$

where $\mu_{\mathtt{n}}$ indicates the respective molar ratios:

$$\mu_{\mathtt{n}} = \frac{M_{\mathtt{n}}}{\sum_{\mathtt{n}} M_{\mathtt{n}}} \tag{1.45}$$

Another suggestion made by Perlo et al. [8] is the weighting function (Eq. 1.46), where $i_{\mathtt{i}}$ and $i_{\mathtt{f}}$ are echo time number limits of a region at the beginning of the decay, called density, $j_{\mathtt{i}} = i_{\mathtt{f}}+1$ and $j_{\mathtt{f}}$ are the limits of the the end of the decay, called contrast, and they are adjusted to have optimum contrast in the profile:

$$w(i_{\mathtt{i}}, i_{\mathtt{f}}; j_{\mathtt{i}}, j_{\mathtt{f}}; t_{\mathtt{E}}) = \frac{i_{\mathtt{i}} - i_{\mathtt{f}}}{j_{\mathtt{i}} - j_{\mathtt{f}}} \frac{\sum_{j=j_{\mathtt{i}}}^{j_{\mathtt{f}}} S(jt_{\mathtt{E}})}{\sum_{i=i_{\mathtt{i}}}^{i_{\mathtt{f}}} S(it_{\mathtt{E}})} \tag{1.46}$$

Figure 1.11 confirms the possibility of using the weighting function as a tool to easily get contrast in expontential decays. Decay constants of 1.00 (1.11(a)), 0.75 (1.11(b)) and 0.50 ms (1.11(c)) were simulated and co-added over the first 4 and the last 28 echoes in a train. The resulting weight function is present in Fig. 1.11(d), where the profiled sample was supposed to have 3 different layers with 4 mm of thickness. This example validates Eq. 1.46 as a good approach to examining weighted profiles.

Though they have several limitations, unilateral NMR sensors have plenty of benefits that justify their importance. Furthermore, among other improvements, single-sided NMR is now able to measure spectroscopic information [9] and perform imaging [10], and is well established in the NMR market. Sensors with different magnet sizes and configurations can produce depths ranging from micrometers to several millimeters, with different gradients and Larmor frequencies.

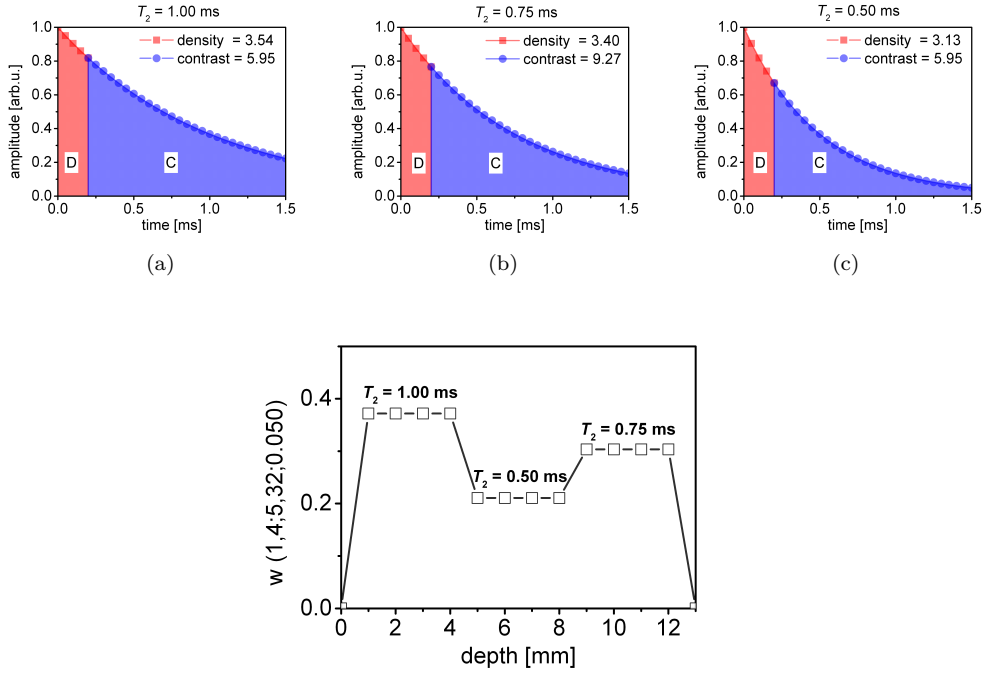

FIGURE 1.11: Exponential decays and a profile with the respective weighting functions. (a) Decay with $T_2 = 1.00$ ms. (b) Decay with $T_2 = 0.75$ ms. (c) Decay with $T_2 = 0.50$ ms. (d) Weighting function.

1.2 Topics in polymer science

Polymers are present in a huge diversity of materials, often in the day-to-day stuff of modern society. They are classified as organic or inorganic, are often studied in biology (DNA and RNA), pharmacy or materials science, and are found in materials such as rocks, diamonds, bones, muscles, skin, cotton, silk, wood and wool. Polymer morphology depends on the chemical group present; for example, the simplest polymer is the polyethylene, which has the repeat unit $(\text{-CH}_2)_n$. Each polymer has particular mechanical and chemical properties and features, providing several different applications.

The concept of the polymer was introduced by Hermann Staudinger in 1920 [59], who earned the Nobel Prize in Chemistry in 1953 for the discovery. Today the original molecule is called a *monomer* and the repeating structure is called a *chemical repeat unit*. Unless it is a cyclic molecule, the terminal group is not repeated (Fig. 1.12). A polymer macro-molecule typically forms from thousands to millions of monomer units [60]. This section briefly discusses NMR relaxation in polyethylene with applications in heat fusion of pipes and detecting polyethylene cross-link density (subsection 1.2.1) and following visible light curing of acrylic resins (subsection 1.2.2).

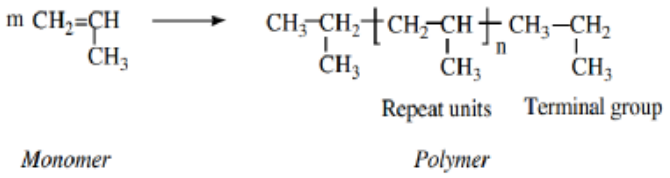

FIGURE 1.12: Monomer and Polymer.

1.2.1 Polyethylene

Polyethylene can be synthesized at high pressure and high temperature; however, this process generates short-chain branching, and the result is called low-density polyethylene (LDPE). Polyethylene can also be prepared at low pressure with a Ziegler-Natta catalyst (Nobel Prize in Chemistry for 1963), which provides a high degree of crystallinity and stiffness, producing what is called high-density polyethylene (HDPE) [61]. Other thermoplastics with a broad range of applications are, for example, polypropylene (PP), polystyrene (PS), polyvinyl chloride (PVC), polyamide (PN) and polybutylene telephthalate (PET) [60].

Polymers are subject to exclusive transitions over changes in temperature. Below the glass transition temperature $T_{\mathtt{g}}$ (different for each polymer), polymers are in the glassy state, hard and brittle; above $T_{\mathtt{g}}$, they are soft and flexible. This transition is a feature of the amorphous phase of polymers. The melting transition, characterized by the collapse of a polymer's chain crystal structure when the temperature exceeds the melting temperature $T_{\mathtt{m}}$, affects only crystalline polymers [62].

High-Density Polyethylene is a semi-crystalline material; i.e., it possesses a multiphase structure of mobility that includes rigid (crystalline), semi-rigid (interface) and soft (amorphous) fractions, with lengths of approximately of 6.5, 0.8-1.3 and 5 nm, respectively [11]. Above the $T_{\mathtt{g}}$, solid state NMR suggests a particular T_2 for each phase component [11]. Assuming $A_{\mathtt{s}}$, $A_{\mathtt{i}}$ and $A_{\mathtt{l}}$ for the respective mass fractions and $T_2^{\mathtt{s}}$, $T_2^{\mathtt{i}}$ and $T_2^{\mathtt{l}}$ for the respective T_2 of the different phases, the transverse magnetization decays are given in Fig. 1.13 and are mathematically explained by one Abragam (rigid phase) and two exponential (semi-rigid and soft phase) functions:

$$A(t) = A(0)^{\mathtt{s}} \exp\left[\frac{t}{2T_2^{\mathtt{s}}}\right]^2 \left[\frac{\sin(\mathtt{a}t)}{\mathtt{a}t}\right] + A(0)^{\mathtt{i}} \exp\left[\frac{t}{T_2^{\mathtt{i}}}\right] + A(0)^{\mathtt{l}} \exp\left[\frac{t}{T_2^{\mathtt{l}}}\right] \qquad (1.47)$$

Polyethylene pipes

High-density polyethylene (HDPE) piping requires low-cost yet durable materials. There are two main kinds of PE pipe connection: the heat fusion and the electrofusion couplings. The definition of heat fusion varies across the plastic industries; the most

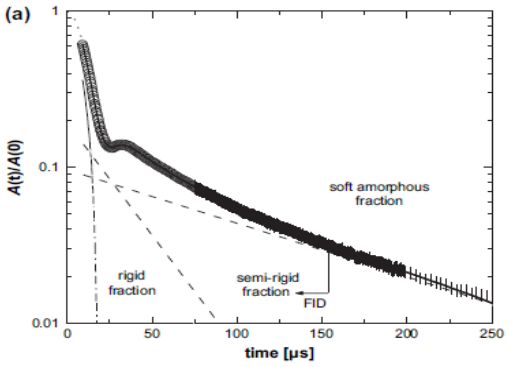

FIGURE 1.13: T_2 for HDPE at 100°C [11].

accepted is that heat fusion is the incomplete fusion of two polymer parts, at a level less complete than that of a molecular bond [63]. The heat fusion joining process for pipes essentially consists of touching two smooth piping ends together, facing and heating them until the melting point, then putting pressure on the join. This process produces defects such as mechanical damage, contamination, lack of fusion and sites with differing morphologies. Failures can be expected after some use [64].

The relaxation time T_2 of an NMR signal depends on molecular mobility and, therefore, on crystallinity. For semi-crystalline polymers at temperatures between the glass transition temperature and the melting temperature, the signal acquired with the NMR-MOUSE derives mainly from amorphous regions, while the signal from the crystals has a short T_2 and decays considerably within the dead time of the instrument [12].

Annealing by heating the sample below the melting temperature invokes recrystallization processes. With slow cooling, the proportion of material in the crystalline phase is higher after recrystallization than it was before. As the total amount of material within the sensitive volume of the sensor is about the same, the amount in the amorphous phase (which gives rise to the detected signal) is smaller, so the signal intensity is less.

Polyethylene samples treated with β-radiation

Beta particles, or β-radiation, first detected by Ernest Rutherford in 1899 [65], are generated by the nuclear fission of unstable atomic nuclei. This particles have the required energy to break the covalent bonds of a polymer chain, increasing the cross-linking of the molecules (Fig. 1.14); i.e., the alkene groups become cross-linked alkane. This fact can be easily observed in the vibrational modes of the alkene groups, which fall between 1700 and 1600 cm^{-1}, as measured by infrared-spectroscopy [66].

The unit of absorbed β-radiation is the *Gray* (a tribute to the British physicist Louis Harold Gray), or Gy, and is defined as the absorption of one joule of ionizing

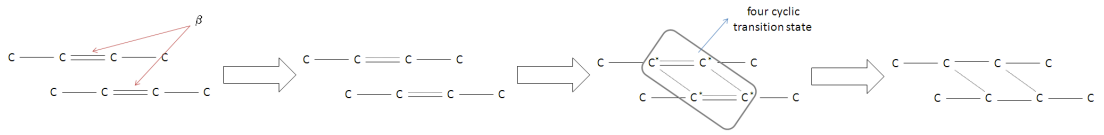

FIGURE 1.14: Increasing the cross-link density in PE due to absorption of β-radiation.

radiation by one kilogram of matter (1 Gy = 1 J/kg). A few radiation doses (kGy) improve mechanical and chemical material properties for an inexpensive price.

1.2.2 Acrylic resins

Visible light curing (VLC) dental composites made of highly filled acrylic resins have been successfully replacing amalgam fillings in tooth restoration over the last three decades. These resins are polymerized in about 20-40 s using a photo-initiator (camphor quinone, CQ, Fig. 1.15) amine accelerator system that is activated by an LED light curing unit (LCU) typically having a wavelength range of 440-480 nm and irradiances of 600-2000 $\mathtt{mW/cm^2}$.

Besides polymerization shrinkage, bio-compatibility and wear resistance, one of the most frequently discussed issues in VLC resin composite development is the general question of how fast and at what maximum thickness a light-cured material can be processed properly in dental applications [67–69]. Since the development of these materials a vast number of studies have investigated the curing kinetics [70–72] degree of cure (DC) [73, 74], and depth of cure (DoC) [74–76]. To characterize the curing process in order to optimize medical applications by predicting curing parameters like curing time, optimum light intensity and resin formulation, various test methods have been introduced and evaluated for time-resolved monitoring of the curing process. The curing-enthalpy has been analyzed with Differential Scanning Calorimetry (DSC) [77], the DC with Fourier Transform Infrared Spectroscopy (FTIR) [69, 73, 74], the shrinkage strain with dilatometric devices [71, 72, 78], the shrinkage stress with stress-analyzers [73, 79, 80], the light transmission with radiometer measurements [70, 81], and the ionic conductivity with dielectric analysis (DEA) [81, 82]. All of these methods, amongst others, provide time-dependent data and allow for kinetic modeling of the curing process and for predicting the progress of the polymerization reaction.

Depth-dependent curing of VLC composites is usually examined through the depth of cure (DoC) parameter evaluated with FTIR, mechanical (hardness and scraping tests) and optical measurements [70, 74–77]. In the case of hardness or scraping tests, the DoC can only be obtained subsequent to the light-curing procedure. These results are always influenced by continuing diffusion-controlled polymerization and cross-linking

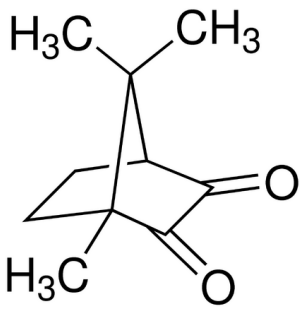

FIGURE 1.15: Camphorquinone molecule.

as well as termination of radicals, which together govern post-curing behavior and lead to time-dependent material properties. An optical or FTIR method allows measurement of the curing behavior of composite samples with different layer thicknesses; however, the DoC cannot be evaluated using a single bulky specimen. The kinetics of photo polymerization have been successfully studied using T_2 relaxation analysis [83].

A polymerization reaction encompasses three stages: initiation, propagation and termination [84, 85]. In the initiation stage the reaction is started, for example, by photo decomposition of an initiator into radical pairs. These radicals react with the first monomer. In the propagation stage, macromolecular chains are formed through successive reactions with monomers until the reaction is terminated, typically by combination, disproportionation or lack of monomers. The reaction kinetics are as follows:

1. Initiation

   The initiator I (possibly the camphorquinone (CQ), Fig. 1.15), is activated by light irradiation hν either to a singlet, with a life time in the nano-second range, or a triplet state, with a life time of 50 ms [72]. Triplet-activated CQ molecules I^* may react with accelerator molecules A, forming two radicals (Eqs. 1.49 and 1.49),

$$\mathrm{I} + \mathrm{h}\nu \Rightarrow \mathrm{I}^*_{\mathrm{triplet}} \tag{1.48}$$

$$\mathrm{I}^*_{\mathrm{triplet}} + \mathrm{A} \rightarrow \mathrm{I}^{\bullet +}\mathrm{R}^{\bullet} \tag{1.49}$$

   The polymerization rate is determined by the accelerator radical $R^{\bullet}$ reacting with the first monomer M, as the CQ radical $I^{\bullet}$ shows little reactivity,

$$\mathrm{R}^{\bullet +}\mathrm{M} \xrightarrow{\mathtt{k_i}} \mathrm{RM}^{\bullet} \tag{1.50}$$

If φ denotes the initiator efficiency, I_0 the intensity of the absorbed light at the surface and α the extinction coefficient (assuming an infinite reservoir of accelerator molecules), the depth-dependent rate of the two-step initiation reaction is given by [85]:

$$v_{\mathtt{i}}(d,t) = \mathtt{k_i}\varphi \mathtt{I}_0 t \mathtt{e}^{-\alpha d} = -\frac{\mathtt{d}[M]}{\mathtt{d}t} \tag{1.51}$$

with d being the depth of the reaction in the resin layer and $[M]$ being the monomer concentration.

2. Propagation

$$\mathrm{RM}_{\mathrm{n}}^{\bullet} + \mathrm{M}_1 \xrightarrow{\mathtt{k_p}} \mathrm{RM}_{\mathrm{n+1}}^{\bullet} \tag{1.52}$$

Approximating the rate of the bi-molecular propagation reaction to be independent of the chain length, and denoting the concentration of growing chains by $[RM^{\bullet}]$:

$$v_{\mathtt{p}} = \mathtt{k_p}[M][RM^{\bullet}] = -\frac{\mathtt{d}[M]}{\mathtt{d}t} \tag{1.53}$$

3. Termination

$$\mathrm{RM}_{m}^{\bullet} + \mathrm{RM}_{m}^{\bullet} \xrightarrow{\mathtt{k_t}} \mathrm{M}_{\mathrm{m+m}} \tag{1.54}$$

The combined reaction rate for termination by combination and/or disproportionation is by convention written as

$$v_{\mathtt{t}} = 2\mathtt{k_t}[RM^{\bullet}][RM^{\bullet}] \tag{1.55}$$

In these reactions $\mathtt{k_i}$, $\mathtt{k_p}$, $\mathtt{k_t}$ denote the reaction rate constants of the initiation, propagation and termination stages. At constant temperature, most monomers are consumed in the steady state when the initiation and termination reaction rates are identical, i.e., $v_{\mathtt{i}} = v_{\mathtt{t}}$. Then the steady state propagation rate of a radical photopolymerization is given by:

$$\frac{\mathtt{d}[M]}{\mathtt{d}t} = -K\sqrt{t}[M] \tag{1.56}$$

where

$$K(d) = \mathtt{k_p}\sqrt{\frac{\mathtt{k_i}\varphi \mathtt{I}_0}{2\mathtt{k_t}}\mathtt{e}^{-\alpha d}} \tag{1.57}$$

This leads to the time-dependent monomer concentration

$$[M](t) = [M]_0 \exp\left[\frac{2}{3}\left(\frac{t - t_0}{\tau}\right)^{3/2}\right] \tag{1.58}$$

with the initial time t_0 and the initial monomer concentration $[M]_0$, and

$$\tau(d) = K^{2/3}(d) \tag{1.59}$$

Note that Eq. 1.58 is not the stretched exponential function commonly known as the Kohlrausch-Williams-Watts (KWW) function [86], but rather the function proposed by Kohlrausch in his original work in 1854 [87].

1.3 Topics in cultural heritage

Humans have always tried to understand the past to avoid errors when constructing the future. Looking to the past brings the concept that transformations in a society are not spontaneous, but rather the consequence of many factors. It becomes very important to find proper tools to analyze objects that may explain or suggest new comprehension of some fact. These cultural artifacts are normally heterogeneous systems like textiles, wood, stones, paper, parchment, leather, resins, glass or pottery [13].

Developments in solid and liquid state high field NMR have found many applications in the cultural heritage field; however, the possibilities for experiments have sharply increased with the advent of open sensors, their capacity for evaluating objects of arbitrary size non-destructively [6]. Many areas of cultural heritage science have already been explored using single-sided sensors, for example analyzing frescoes (Fig. 1.16(a)) and mummies (Fig. 1.16(b)) [13–17, 20, 28].

In the present section, some applications of NMR open sensors are reviewed. They encompass the use of the NMR-MOUSE as: a sensor for evaluation of a new inorganic consolidation process (section 1.3.1), ascertaining elementary composition in potteries (section 1.3.2), a tool to understand the deterioration of writing materials such as parchment or paper (section 1.3.3) and evaluating layers of multi-laminated canvas samples used as painting substrate (section 1.3.4).

1.3.1 Consolidation of stones

An important element of East Asian culture, art in religious buildings, is manifested in temple architecture. Chinas's temple culture flourished in the 5^{th} century, during the

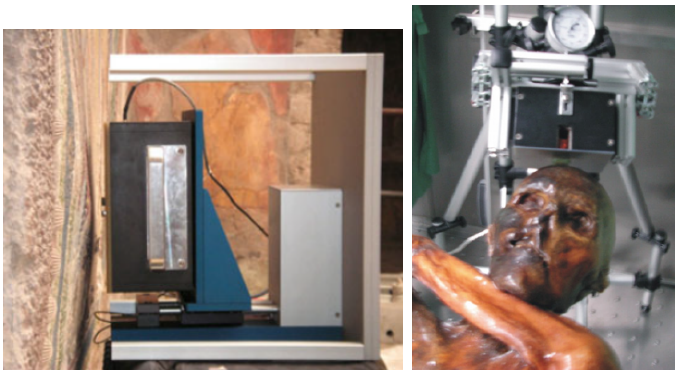

(a) (b)

FIGURE 1.16: NMR-MOUSE as a measuring tool for cultural artifacts. (a) Depth profile of frescoes at Herculaneum [15]. (b) *In situ* analysis of the Iceman (3300 BC) [28].

Northern Wei Dynasty, in the Yungang Grottoes, today listed as a UNESCO world heritage site. Its statues combine the Buddhist tradition of India with traditional Chinese elements.

These sandstone statues have suffered high degradation and destruction during the past thousand years, mainly due to water action. New methodologies have been studied for protecting and preserving such materials. In this context, the reinforcement of stones became an important issue in art conservation.

Conservation techniques have been developed following the principle of minimum human intervention and no changes in the historic condition. Open-air, outdoor objects in particular suffer weather aging interaction, so reinforcing and judicious sealing is very important. In addition to providing high durability, the treatment should be reversible, keeping the material, physical and chemical properties intact [88–90].

A consolidation process can be organic or inorganic. Inorganic consolidation materials are calcium hydroxide, barium hydroxide, sodium silicate (PS material), etc [88, 89, 91, 92], while the organic material used is mainly a polymerized acrylic, silicone or epoxy resin [93, 94]. Due to degradation of polymers, the literature recommends against the use of organic consolidation [89].

The main constituents of sandstone are quartz, feldspar and clay minerals cemented and made of calcium carbonates. In particular, the sandstones in the Yungang Grottoes have a composition above 10% in mass of mineral components such as ferrous iron calcite and dolomite. Chemical weathering of carbonate cements includes dissolution of carbonate minerals, oxidation of Fe^{2+}, Fe^{3+}, gypsum, epsomite, water and carbon-magnesium by hydrolysis.

The main chemical reactions of degradation are:

$$2\,SO_2 + O_2 \Rightarrow 2\,SO_3 \tag{1.60a}$$

$$SO_3 + H_2O \Rightarrow H_2SO_4 \tag{1.60b}$$

$$H_2SO_4 + CaCO_3 + H_2O \Rightarrow CaSO_4 \cdot 2\,H_2O + CO_2\uparrow \tag{1.60c}$$

and

$$CO_2 + H_2O \Leftrightarrow H_2CO_3 \tag{1.61a}$$

$$H_2CO_3 + CaCO_3 \Rightarrow Ca(HCO_3)_2 \tag{1.61b}$$

The carbonate cement dissolution increases the pore size. Water can get in and out easily, causing serious damage to the stone, in some cases breaking or even disintegrating the object.

Nano-calcium hydroxide dispersion strengthened the stone through a certain depth of penetration into the pores by water with dissolved CO_2 and performs a reaction which regenerates $CaCO_3$ and modifies the pores, achieving the effect of consolidation. Of course, this needs to be done after the desalination process to ensure that no other impurities remain inside the pores. The major reactions of consolidation are:

$$Ca(OH)_2 + CO_2 \Rightarrow CaCO_3 + H_2O \tag{1.62}$$

$$Ca(OH)_2 + Ca(HCO_3)_2 \Rightarrow 2\,CaCO_3 + H_2O \tag{1.63}$$

After nano-calcium hydroxide consolidation, the rock regenerates calcium carbonate and fills the pores. Quartz and feldspar grains, cemented, combine to achieve the effect of consolidation. Dispersion techniques and a dispersant combination of modified materials achieve uniform and stable dispersion solutions. However, the number of nano-particles stably dispersed in a medium depends on the kind of the dispersive medium and the ratio, its viscosity and size, and the depth of reinforcing agents' effects.

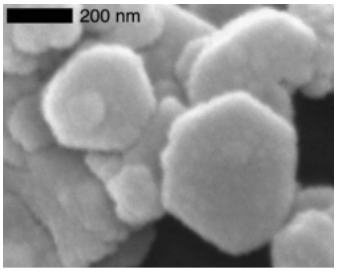

FIGURE 1.17: *SEM* (scanning electron microscopy) image of a $Ca(OH)_2$ nanocrystal [96].

Overall, selecting the dispersion medium of nano-materials to maximize refilling effects brings clear advantages.

Filling penetration into internal porous artifacts is based on the hydrophobic behavior of alcohol chains and nano-materials. When the number of nano-calcium hydroxide surfactant increases, the surface activity and the ability to capture carbon dioxide in air increases, leading to a speeding up of carbonation by calcium hydroxide. Currently, applications of nano-powder dispersion techniques are basically physical, chemical and dispersive material dispersion.

Because of its low solubility (about 1 g/L) and huge crystal size in water, aqueous calcium hydroxide solution has low penetration depth in stone relics. Often the solution is expelled to the surface layer, bleaching the artifacts to a hard shell of calcium, leading to slow air carbonation. Larson et al. [92] limed slurry and used the composite in the consolidation of powdered calcium carbonate. Using hot CO_2 and other methods they could increase the solubility of lime in water; however, the lime carbonated CO_2 absorption was still an issue over long time periods remained a difficult problem to solve.

Huizhi [95] tried aqueous isopropanol with calcium oxide in 90°C to dissolve the -OH bond of the immersed particles, obtaining an average particle diameter of 6 - 8 μm. The calcium hydroxide was dissolved and dispersed even better in pure isopropanol, ethanol and other organic materials, which, to a certain extent, solved the problem of small calcium hydroxide solubility.

Baglioni [96] used small calcium hydroxide crystals in ethanol dispersion as a binder material, for example, for use on flaking mural reposts (Fig. 1.17). After ethanol evaporation, calcium hydroxide and water absorbs CO_2 at a mural patch stone support for peeling between the calcium carbonate and then stably bonded together. Dei and Salvadori [97] also detailed the nano-calcium hydroxide dispersion consolidation in some San Zeno church frescoes (Verona, Italy) and achieved significant results.

In successful consolidation, the reinforcing agent penetrates uniformly from the

surface to the internal masonry, changing physical and mechanical properties, and improving the stone state. The processing materials should have high hydrophobic behavior so that if water vapor infiltrates the stone, the pores will expel the moisture and the chemicals will be filtrated.

NMR is a feasible evaluation tool for the consolidation process because it provides information on water diffusion and relaxation in porous materials and can map structural heterogeneity. Such an approach has been employed on many different stone artifacts and is represented in the literature [13]. Single-sided NMR sensors have been used to evaluate porosity of geological drill core sections [24] and understand quantitatively the water flow in water-repellent treatments in biocalcarenite (Lecce Stone) [25]. Unilateral NMR has also had success in monitoring a consolidation treatment based on polymerization of acrylic monomers inside a porous stone [26]. Recently, porosity of sandstones and calcarenite were measuring during the time of action of a hydrophobic treatment with dimethylsiloxane [27]. Two inflection points of low to high water content were found: the first one was attributed to surface effects, the second one to the dimethylsiloxane penetration depth.

1.3.2 Potteries

Pottery ceramics are a very special class of archeological ceramic artifacts that often require non-invasive analysis for their characterization. They are made of clay, which can have several different elementary compositions, depending on the region of origin, the custom manufacturer and the firing approach. Such differences also bring variability in the porous geometric parameters of these materials [13].

Some researchers used high-field ^{27}Al and ^{29}Si NMR to characterize clay and the firing process [98–100]. A water diffusion experiment was not successful due the huge amount of paramagnetic species in the clay [101].

An important advancement achieved with portable NMR devices and acquisition of multidimensional $T_1 - T_2$ relaxation maps is the pottery characterization of pore size and composition. This was possible because T_1 is sensitive to pore surface-to-volume ratio, but not to changes in gradients, while T_2 is very sensitive to changes in internal or external gradients as well as the presence of para or ferromagnetic ions [13]. $T_1 - T_2$ maps of soaked potteries have already been shown to be able to distinguish and classify Italian ceramics [102, 103] and Roman pottery [104].

1.3.3 Writing materials: parchment and handmade papers

History has been recorded on many different surfaces. Ancient scribes used materials such as stones, bones and leaves. With the development of new technologies these materials were replaced by more advanced ones such as baked clay, wax, tissue fibers, papyrus, parchment and paper.

During about the 25^{th} century BC, ancient Egyptians developed the technique of making papyrus, which is considered the precursor of paper. This material was also important for the ancient civilizations of the Middle East (Hebrews and Babylonians) and those of Greece and Rome.

Made from animal skin, parchment was a substitute for papyrus and became the main writing material during Roman times. Due to its ease of preparation, the history of parchment spans more than 4500 years. Some examples of historic texts written on parchment are: the Alexandrinus, Gigas, Leningrad, Sinaiticus and Vaticanus codices; the Gospel of Judas and the Book of Enoch; the Dead Sea Scrolls; the Masoretic Text and some early Islamic texts. These texts are fundamental to understanding the bases of modern Judaism, Christianity and Islam [105].

The invention of paper and the paper-making process is attributed to the Chinese eunuch Cai Lun in the late 1^{st} century AD. Only in the 13^{th} century did it arrive in Europe. Paper achieved great importance after the year 1440 thanks to Johannes Gutenberg. He developed the type-setting tool, which contributed to a fast rise in diffusing impressed papers and enabled fast circulation of new ideas. Parchment production could not supply the huge need for printing materials.

Parchment

Writing on animal skins is a practice that dates to about 2500 BC. With the development of chemical knowledge, more sophisticated materials such as leather and parchment could be produced from skins. Parchment was developed in Pergamon (Greece) and found great importance during the Roman and Middle Ages, being the substrate material of many Roman official and religious documents.

Parchment is a very important topic in cultural heritage. It is essentially collagen and normally made of goatskin, sheepskin or calfskin cut at the hypodermis level, so the skin is often shaved by lime, sometimes mixed with other chemicals. The skin is washed in water to remove blood, grime, fat and excess flesh; afterward, the skin can be re-limed in order to get a better final product. The final step is drying the parchment on a stretching frame until it is ready for use [13]. Due this very arbitrary production

process, different parchments show different chemical proprieties. However, a common issue among different kinds of parchment is that it very sensitive to relative humidity.

Parchment composition shows fibrillate collagen embedded in a hydrated matrix of complex proteins, elastin, salts and lipids in a complex hierarchical structure. Figure 1.18 shows the collagen hierarchical structure of a rat tail tendon, from the molecular to the tissue level [106].

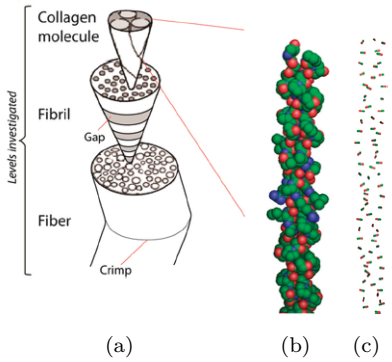

FIGURE 1.18: Hierarchical structure of collagen [106]. (a) The fiber fibril and collagen molecule. (b) Collagen molecule with amino acids (nitrogen), carbon and oxygen colored by blue, green and red, respectively, and the hydrogen atoms are not present. (c) Amino acid chains that organize in a primary, secondary and tertiary structure, with 64 nm in parchment.

There are three main irreversible chemical process that deteriorate parchment collagen, changing the collagen structure and then its interaction with water [107]:

1. Hydrolysis: this process cleaves the peptide linkages, resulting in amino acid end groups. Fungi enzymes accelerate this degradation process.

2. Oxidation: this process degrades amino acids into carbonyl compounds, increasing cross-linking. It is correlated mainly with the storage environment.

3. Gelatinization: this process disorganizes the collagen helical structure, transforming collagen into gelatin, as presented in Fig. 1.19. This process may occur spontaneously.

A solid state NMR experiment with degraded parchment revealed a spectrum with two peaks and different line-width components; the broad one was attributed to collagen and the narrow to water [108]. This experiment revealed that aging decreases the water content in a parchment sample due to partial hydrolysis of peptide bonds in collagen. The hydrolyzed collagen is considered a degraded gelatin, with a mixture of smaller molecular weight polypeptides.

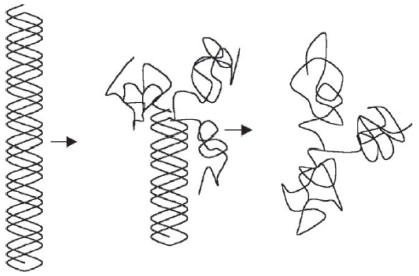

FIGURE 1.19: Gelatinization process [107]. (a) The collagen triple helix. (b) Intermediate state. (c) Gelatin.

A T_1 experiment on parchment was performed with a single-sided NMR sensor [21]. The proposed interpretation is that the gelatinization process disorganizes the collagen structure and short T_1 values, when the hydrolytic process produces longer T_1 values [13, 109]. A similar study investigated the deterioration of a Dead Sea Scroll fragment [22], and again, T_1 values had good agreement with the deterioration state of the parchment. Recently, interactions of lead white pigments in collagen-based binders were explored using the NMR-MOUSE and it was noticed that the pigments change the protein structure of a collagen fiber [23]. In that work, the decays of a CPMG pulse sequence were studied through fitting by mono-exponential decay function as well as inverse Laplace transform and orthogonal projection to latent structure by partial least square discriminant analysis (OPLS-DA), a kind of multivariate data analysis.

Paper

Paper chemistry and degradation is a very important issue to understand, since paper is one of the most important communication media today. Modern paper differs from historic paper in many ways. Paper quality has worsened with time due the addition of impurities during the industrial process, such as paramagnetic ions and lignin, that make the paper more vulnerable to physical and chemical degradation [13].

Paper has two almost equimolar constituents: cellulose and water. Cellulose, a kind of polysaccharide, is a homopolymer made of a-D-Glucose and is the most abundant polysaccharide. D-glucose is connected by linkages called the β-1,4-glycosidic bond. Cotton has a very high cellulose content, between 90 and 98%, while wood typically has 40 to 50%. Polysaccharides such as cellulose are the building blocks of cell walls in plants [60].

Two relaxation components are observed in a paper sample; the fast one is attributed to the cellulose matrix and the slow one to water pools. The ratio between the water and cellulose decay amplitudes is characteristic of the kind of paper, from 0.9

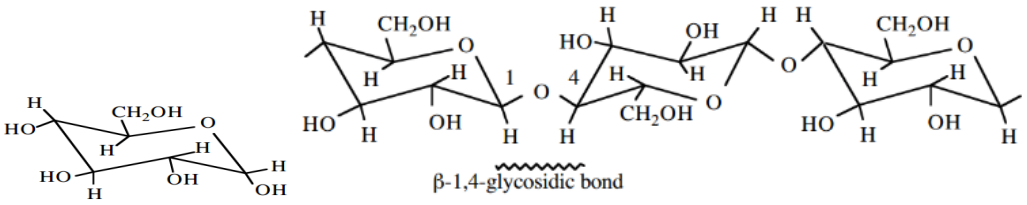

FIGURE 1.20: The cellulose structure. (a) The α-D-Glucose monomer. (b) The monomer connected to generate the polymer [60].

for good to 1.7 for low quality papers [110]. T_1 measurements of paper revealed two components; the short one did not show correlation while the long one was found to be dominated by spin-diffusion, with similar values for the cellulose and water domains [110, 111].

It was found that the freezing temperature of water in paper is lower than 213 K [110, 111], so paper can be interpreted as being a porous polymeric system with water pools with porous size of 1.4 nm, well-defined, surrounded by amorphous cellulose (3.0 nm), and this last one surrounded by crystalline cellulose as indicated in Fig. 1.21 [112]. Paper can suffer chemical degradation from fungal hydrolytic enzymes, which results in random chain scission (by hydrolysis) or peeling, and physical degradation which transforms crystalline to amorphous cellulose, loosing bound water that can be catalyzed by the existing paramagnetic impurities [113]. A chemical aging process in paper was monitored using T_2 variations, with three components, where only the intermediate component had shortened in terms of time [113].

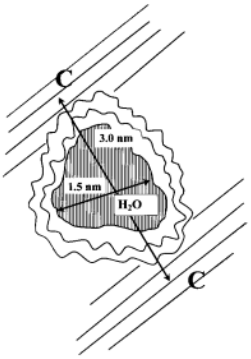

FIGURE 1.21: Paper morphology [112].

A non-invasive *in situ* study of degraded paper could be performed with single-sided NMR sensors. The T_2 values acquired for naturally [18] and artificially aged paper [19] showed distinctions among the low, middle and high levels of degradation, with values decreasing with increasing degradation level. Proietti et al. [19] also compared T_2

values of paper in different magnetic gradients and similar spin-lock effects and ensured that the T_2 similar values indicate low water diffusion.

Ancient Chinese paper began to be used for printing information carried by bearers and dissemination of traditional Chinese culture. The handmade paper production process is more complex and provides better performance compared to modern mechanically produced paper. The initial step in handmade paper production is to collect the raw materials, which can be linen, rattan, rice, hemp or bamboo. After soaking for 12 to 24 hours, the raw material must be cooked with soda ash for almost 8 hours in order to produce a slurry. When this slurry is dried, the final paper is obtained.

The first Chinese paper was made of hemp and produced by Han Cai Lun during the Western Han Dynasty. In the Tang Dynasty, the government replaced hemp with rice to yield a finer-textured paper, rice paper. Bamboo paper dates to the $9^{\texttt{th}}$ century, is made in a high quality fabrication process at high temperature to kill pests, and was used in several important records of Chinese history. Furthermore, there are about 20 different types of paper available using high-strength paper mulberry bark as raw material. These papers are always very fibrous, with a soft texture, and are durable.

1.3.4 Canvas

The art of painting is very old. It started on the walls of caverns and others materials humans could easily find in nature, most of the time representing the current beliefs of the society. From ancient Egypt to the Middle Ages, painting on mortar walls became very common and resulted in the art of fresco painting.

Linen canvas as the substratum for painting and a suitable replacement for wood and parchment dates from about the $15^{\texttt{th}}$ century. An alternative method for linen canvas is known as cotton duck, cheaper and with good performance for acrylic inks, but worse performance for oil inks. The canvas material is normally stretched over a wooden frame, so it must be prepared by the painter carefully before being painted.

It is common in art galleries the reinforcement of old and fragile canvas paintings with polymers waxes or another canvas layer, which may be not a good treatment. There is still no methodology available to evaluate this process. The use of canvas is not limited to paintings. It has also been used to make synthetic products such as shoes, tents or bags, among many other possibilities.

2. Aims

This work had several aims, all related to the development of new unilateral NMR methodology for the polymer and cultural heritage fields. They can be summarized as:

1. Polymer Science:
   - 1.1 **HDPE relaxation**:
     - 1.1.1 Heat fusion joining in HDPE pipes: develop single-sided NMR hardware and verify morphological changes after recrystallization through heat fusion joining process of two PE pipe ends;
     - 1.1.2 Samples treated with β-radiation: propose methodology for checking differences in cross-link density of PE treated with low differences of absorbed β-radiation;
   - 1.2 **Photo polymerization**: explore the capacity of the NMR-MOUSE for tracking photo polymerization reactions of dental resins, with changes in mobility and monomer concentration, and propose a theoretical model for describing the depth-dependent reaction kinetics.
2. Cultural Heritage Science:
   - 2.1 **Sandstone**: non-invasively evaluate a recently developed inorganic consolidation process based on adding $CaCO_3$ to stones of interest to Chinese culture;
   - 2.2 **Pottery**: correlate ancient potteries' elemental compositions with their transverse relaxation times, given by a unilateral NMR experiment;
   - 2.3 **Writing materials**
     - 2.3.1 **Parchment**: ascertain and evaluate damaged parchments using uni- or multi-dimensional relaxation experiments;
     - 2.3.2 **Chinese-papers**: propose experiments and develop methodology to discriminate between different kinds of handmade Chinese papers and evaluate their degradation;

2.4 **Painting canvas**: check the performance of NMR-profiling in determining their layer structures of double-laminated canvases.

3. Materials and methods

This work detailed in this thesis consists mainly of development and applications of NMR, particularly the single-sided stray-field sensor NMR-MOUSE, so a section of this chapter is dedicated to describing a single-sided NMR experiment (section 3.1). This chapter also introduces the data analysis software used (section 3.2) and the analyzed samples, with respective descriptions of the particular measurements performed for the polymer samples (section 3.3) and for the cultural heritage samples (section 3.4).

3.1 The NMR setup

An NMR experiment requires the presence of a static magnetic field $\mathbf{B}_0$ that determines the NMR frequency (Eq. 1.4). Generally, the value of the magnetic field is expressed in MHz, supposing that the analyzed isotope is ^{1}H. In the case of a magnetic field provided by an NMR-MOUSE®, the magnetic field is generated by four bar magnets, which produce a homogeneous magnetic field in a plane at a particular depth (Fig. 1.8(b)). The profile MOUSE's (PM) utilized are labeled according to the allowed depth access with the following specifications (Magritek GmbH [114]):

1. *PM2*: this sensor provides a magnetic field of 29.3 MHz at 2 mm above its surface. The gradient of about 35 T/m permits spatial resolution of 5 μm;
2. *PM5*: the field allowed by this sensor is 18.1 MHz. At a depth of 5 mm the existing gradient lies over 22 T/m, which corresponds to 10 μm of spatial resolution (Fig. 3.1(a));
3. *PM25*: this sensor is larger and heavier than the previous two. This huge sensor generates a static field of 13.7 MHz and enables a depth range of up to 25 mm with a gradient of 8 T/m and a spatial resolution of 100 μm.

Guided by computer software, the NMR spectrometer is the device responsible for synthesizing radio frequency (RF) impulses with the required modulation. It also makes the analogic-digital conversion and has input impedance of 50 Ω. In portable NMR, it

is natural to use portable spectrometers. Two portable spectrometers were used in this thesis work:

1. *Minispec* (Fig. 3.1(b)): produced by the company Bruker, it is controlled by the Minispec software [115];

2. *Kea*: fabricated by the company Magritec Ltd., it is guided by the Prospa software [116].

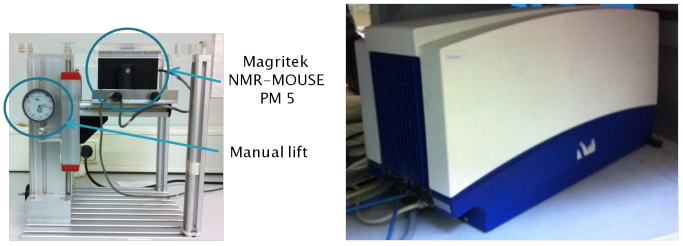

(a) (b)

FIGURE 3.1: (a) The NMR-MOUSE PM5. (b) The Minispec spectrometer.

Before the electrical impulses go to the probe and become the magnetic field, other electric components are required. One of them is the power amplifier, which amplifies the milliwatts of power coming from the transmitter nearly into the kilowatt range. Another component, the duplexor, is responsible for protecting the receiver from the transmitter, as both share the same coil. The pre-amplifier amplifies the weak spin signal (in the μW range) from the sample so that it can be detected and digitized by the spectrometer receiver. The receiver has a power splitter that affords analog quadrature detection, i.e., acquisition of real and imaginary components. All of thes components have frequency band restriction.

The coil is a *LC* (indutance capacitance) or *Tank* circuit. This circuit possesses two variable capacitors: one in series to the coil, called *matching* ($C_{\mathtt{M}}$) because it matches the circuit impedance to 50 Ω, and a second one in parallel, called *tunning* ($C_{\mathtt{T}}$), responsible for achieving the respective resonance frequency. The coil inductance (L) mainly depends on its geometrical characteristics (Fig. 3.2). The circuit frequency is determined by the values of L and approximates the sum $C_{\mathtt{M}} + C_{\mathtt{T}}$ [117]. However, a small resistance (R) is always present and is responsible for dissipating some of the energy as thermal energy.

Independent of the software language, all the concepts are common. For example, for spectroscopic reasons, in relaxometry it is preferable to keep equal pulse lengths $T_{\mathtt{p}}$ for the 90° and 180° pulse. The difference between them is in the electrical attenuation.

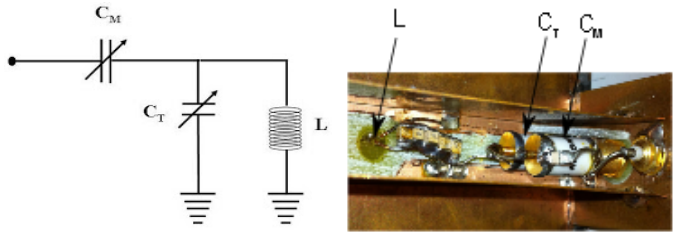

(a) (b)

FIGURE 3.2: (a) The LC circuit. (b) A real LC circuit linked to a surface coil.

att_{90} is the pulse attenuation of 90°, which is the double of att_{180}, the 180° pulse attenuation. Thus the 180° keeps providing the double of the voltage of the 90° pulses, or four times their power.

A feasible algorithm for CPMG or OW4 acquisition in an inhomogeneous field is:

1. Preparation: the recycle delay (rd) or recovery time (rt) should be longer than $5T_1$ if no T_1 weighting is expected, or intermediate if T_1 weighting is desired;
2. 90° pulse: the transmitter pulses at the resonance frequency for a time $T_{\mathtt{p}}$ and attenuation att_{90};
3. Dephasing: the magnetization spreads for a time $T_{\mathrm{E}}/2 - T_{\mathtt{p}}$
4. Echo train (loop with N repetitions, meaning N echoes):
   - 4.1 180° or 90° pulse: the transmitter pulses at the resonance frequency for a time $T_{\mathtt{p}}$ and attenuation att_{90} if 90° pulses are required or att_{180} to perform 180° pulses;
   - 4.2 Rephasing: the magnetization refocuses during a time $(T_{\mathrm{E}} - T_{\mathtt{p}} - T_{\mathtt{acq}})/2 - T_{\mathtt{shift}}$, where $T_{\mathtt{acq}}$ represents the time when the receiver is getting the spin answer of the system, or the echo magnetization, and $T_{\mathtt{shift}}$ represents a possible deviation in the echo center;
   - 4.3 Acquisition: the receiver collects the magnetization during a time $T_{\mathtt{acq}}$. It is possible to acquire $T_{\mathtt{acq}}/\mathtt{dw}$ points (integer number), where $\mathtt{dw}$ represents the dwell time, normally one point per microsecond;
   - 4.4 Dephasing: in this step the magnetization spreads over a time $T_{\mathrm{E}} - T_{\mathtt{p}} - T_{\mathtt{acq}}/2 + T_{\mathtt{shift}}$, so the loop is repeated.

The echo time should be as small as possible, which increases the signal-to-noise ratio and minimizes diffusion effects. However, time is needed for dissipation of the transmitted power in the probe and and also for the the other electronic devices to

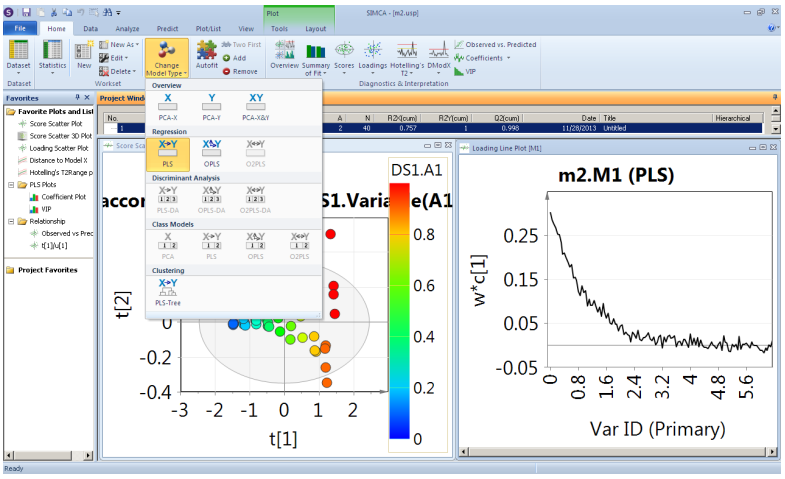

FIGURE 3.3: The software SIMCA 13.0.

recover. This time is known as *dead time*, $T_{\mathtt{d}}$. In the optimum condition, $T_{\mathtt{E_{opt}}} = T_{\mathtt{p}} + T_{\mathtt{acq}} + 2T_{\mathtt{d}}$.

3.2 The MVDA software

Among several multi-variate data analysis (MVDA) software products on the market, the software SIMCA 13.0, from the company Umetrics (Sweden), was chosen and purchased. A three-day training course called "Multivariate Data Analysis," promoted by the company and taught by Dr. Olof Rosen, was attended. The software does not require advanced hardware, is quite fast and has an easy interface, as shown in Fig. 3.3. It is possible to perform several kinds of principal component analysis (PCA) and partial least square (PLS) models, which are validated by the coefficients of correlation and prediction, discussed in detail in the Appendix A, between many other multi-variate coefficients and plots. The other mathematical procurements and data plotting were carried out with the software Origin 9.0 and Matlab 2012b.

3.3 Polymer samples

3.3.1 HDPE pipes joined by heat fusion

Four pipes connected using heat fusion provided by a piping company were explored. Three of them, with small diameters (Φ = 115 mm), were labeled *10-001*, *10-008* and *10-009*; the fourth one had a larger diameter (Φ = 165 mm) and was called *large*.

The typical excited area of a regular PM5 coil is 1 cm^2, so a smaller coil was built, with 3 turns and outer and inner diameters of $\Phi_{out} = 7$ mm and $\Phi_{in} = 4$ mm, respectively (Fig 3.4(a)). In order to improve lateral resolution and avoid the mixing of signal coming from different pipe regions (regions A and B in Fig 3.4(b)), and also due the curved shape of the sample, a small sensitive volume was used to ensure that the full sensitive volume was inside the sample (Fig 3.4(d)). The external rims of the joins produced during the heating fusion process had to be shaved off (Fig 3.4(c)).

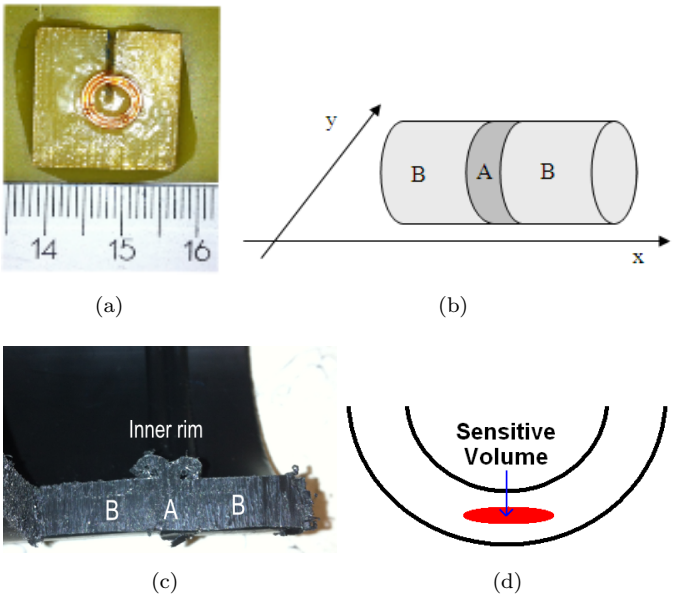

(a) (b) (c) (d)

FIGURE 3.4: (a) The coil with a small sensitive volume. (b) The A (out) and B (at the join) pipe regions. (c) The pipe with the outer rim shaved off. (d) The sensitive volume pipe inside the pipe.

Measurements of both relaxation times with the sequences SR and CPMG were performed at the regions A and B, at room temperature, with two different PM5's, with the parameters shown in Table 3.1:

TABLE 3.1: NMR parameters for the pipe experiment

Parameter	value
Larmor frequency	17.1 or 18.1 MHz
Depth	1 mm
Pulse length	3 µs
Echo time	29 µs
Number of echoes	40
Recycling delay	200 ms
Number of scans	400

Four other PE samples were kept in a drum and removed, each at a different temperature (30, 57, 83 and 110 °C), and had their crystallinity determined by a *Differential Scanning Calorimetry* (DSC) in a triplicate experiment. Furthermore, they were

explored using the same approach applied to the pipes. Comparing sample results can reveal differences between pipes and join crystallinity degree.

Differential scanning calorimetry (DSC) [62] is a thermoanalytical technique based on the differences in absorbed heating as a function of temperature of two samples, one with a known heat capacity and another to be explored. A DSC experiment provides the enthalpy necessary for any thermal transition in a polymer. When compared with a tabulated full enthalpy of the respective polymer transition, the degree of crystallinity can be measured. Being the measured melting enthalpy $\Delta H_{\mathtt{exp}}$ and the melting enthalpy of a 100% crystalline sample $\Delta H_{\mathtt{pur}}$, the crystallinity percentage is calculated as:

$$X_c[\%] = \frac{\Delta H_{\mathtt{exp}}}{\Delta H_{\mathtt{pur}}} \tag{3.1}$$

3.3.2 HDPE samples treated with β-radiation

Intending to monitor differences in the cross-link density between the polymer chains, four HDPE samples with dimensions of 100 x 100 x 5 mm^3, treated with 100, 120, 140 and 160 KGy of β-radiation (Fig. 3.5), were provided by the company SKZ Wuerzburg (Germany) and explored using infrared spectroscopy and unilateral NMR. The infrared spectrometer used was a Perkin Elmer FT-IR Spectrometer Spectrum Two, calibrated to 16 scans and a resolution of 4 cm^{-1}. The NMR experiment was realized with a PM5 device with RF pulses controlled by a Bruker Minispec spectrometer and the parameters present in Table 3.2. Two pulse sequences were chosen, CPMG and OW4, and measurements were carried out over several depths and positions. The acquired data were studied through mono and bi-exponential curve fitting as well by partial least squares regression (PLS), with the radiation dose as the independent variable.

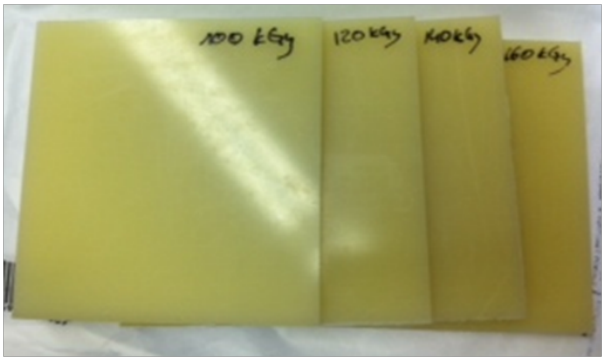

FIGURE 3.5: PE samples treated with β-radiation.

TABLE 3.2: NMR parameters for the PE sample treated with β-radiation

Parameter	value
Larmor frequency	18.1 MHz
Depth	$1, 2, 3, 4$ mm
Pulse length	6 µs
Echo time	32 µs
Acquisition window	6 µs
Number of echoes	128
Recycling delay	600 ms
Number of scans	1024

3.3.3 Dental resins

Two commercial dental resin composites, "Arabesk Top" and "Grandio" (Voco GmbH, Cuxhaven, Germany), with the standard color OA2, were investigated in partnership with Dipl. Ing. Johannes Steinhaus and Prof. Dr. Bernhard Moeginger from the Bonn-Rhein-Sieg University of Applied Sciences (Germany). The samples differ in chemical composition and filler content (Arabesk = 23% monomer in mass, Grandio = 13% monomer in mass). The curing process was photo-activated by applying blue light from a Celalux LED LCU with wavelength $\lambda = 450$ nm (Fig. 3.6(a)).

These NMR measurements were performed with a PM5 sensor operated by a Bruker Minispec with the parameters indicated in Tab. 3.3. The samples studied had a thickness of either 3 mm, allowing testing at four different positions, or 4 mm, allowing testing at six positions. In the following, the space scale is always the distance from the sample surface closest to the light source to the sensitive slice analyzed, set to 1.2, 1.7, 2.2, 2.7, 3.3 and 3.8 mm (Fig. 3.6(b)).

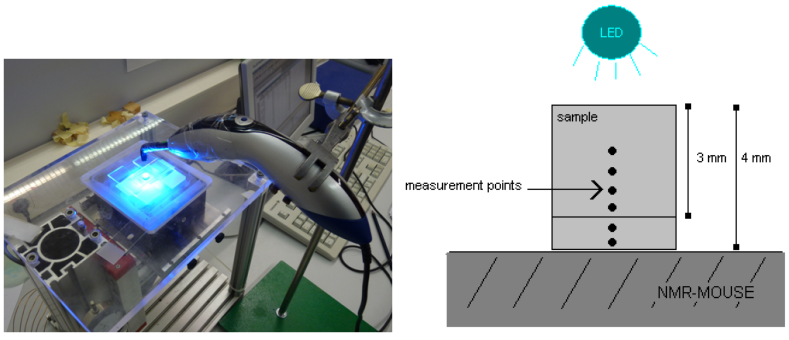

(a) (b)

FIGURE 3.6: (a) NMR setup. (b) Positions of the sensitive slices in the resin sample.

In dentistry, a curing reaction takes less than 40 seconds. This is too fast for NMR analysis. Therefore, 24 common glass slides with a thickness of 1 mm each were used as a light attenuator, slowing down the curing time to about 10 minutes. As it was not

Table 3.3: NMR parameters for the PE sample treated with β-radiation

Parameter	value
Larmor frequency	18.1 MHz
Depth	3 mm
Pulse length	8 µs
Echo time	32 µs
Acquisition window	6 µs
Number of echoes	128
Recycling delay	150 ms
Number of scans	128

possible to stop the photo-reaction, the T_2 measurements are an average of the signal change during 25 s (128 scans). This approximation is acceptable when changes are weak, for example, during the stationary state of a photo-curing reaction, but introduces systematic errors when changes are more pronounced, like at the beginning or the end of the reaction. In such an experiment, the NMR echoes arise only from the mobile monomers present in the sample, while the signal from the solid polymer rapidly relaxes within about 15 µs during the dead time of the sensor.

In order to correlate the NMR results with the temperature history of the sample in the different relevant layers during the curing process, corresponding measurements were performed collecting the temperature evolution with a thermocouple at measurement points similar to those of the NMR setup (Fig. 3.6). However, in this experiment the sample was cut off and the thermocouple was placed underneath. The sample temperature during polymerization was collected for the first 140 s after the start of illumination of both materials (Arabesk and Grandio), each in the following layer depths of the sample: 2.15, 3.40 and 4.40 mm. All measurements were performed three times.

3.4 Cultural heritage samples

3.4.1 Sandstones

Six sandstone samples were subjected to a consolidation process developed by Dr. Zhou Hua of the Beijing Union University (China) and Prof. Dr. Xiao Ya of the Hunan Provincial Institute of Archaeology and Cultural Relics (also in China). The method consists of keeping the stones in a vacuum for 8 hours and then immersing them for the same amount of time in a hydroxide of calcium solutions with purity AR > 95% (established by Fisher Scientific), in a total of six solutions with different kinds or proportions of alcohols. This process characterizes reinforcement by dispersion. The solvent codes are summarized in Table 3.4.

TABLE 3.4: Sample codes and the consolidated alcohol

Sample	Solvent alcohol
blank	no treatment
1	ethanol
2	n-propanol
3	isopropanol
4	ethanol/isopropanol (6/4 volume ratio)
5	ethanol/isopropanol (6/4 volume ratio + 30%(weight) octadecanol)
6	ethanol/isopropanol (8/2 volume ratio)
aged	natural aged sandstone

The samples, similar in size (about 5 x 4 x 2 cm^3, Fig. 3.7), were measured when soaked with deionized water and covered with parafilm to prevent water evaporation during the measurements. The room temperature was 21 ± 1 °C.

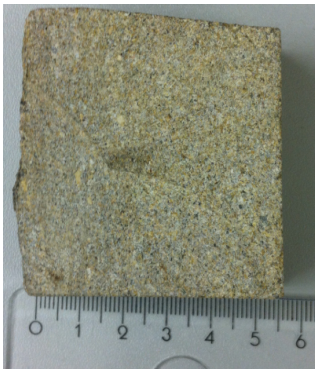

FIGURE 3.7: Sandstone example.

Measurements were performed up to a depth of 3 mm with a PM5 device situated on a manual lift (precision of 0.01 mm) and guided by a Bruker Mini Spec spectrometer. The NMR parameters are summarized in Table 3.5, experiment 1. Another series of experiments was carried out with a deeper depth access using the PM25 sensor situated on an automatic lift controlled by a Magritek Kea spectrometer. The relevant parameters are given in Table 3.5, experiment 2.

Following Equations 1.43 and 1.44, the profiles were processed as a sum over the four initial echoes for the surface profile (Eq. 1.43), and four and thirty-two first echoes for the deeper profile (Eq. 1.43 and Eq. 1.44). In the latter case, the weighting function was also calculated (Eq. 1.46). The short profiles were interpreted with an exponential curve fit, and both of them were smoothed using the "moving average" filter (average of four consecutive points - Matlab®software).

Table 3.5: NMR parameters for the sandstones experiment

Experiment	parameter	value
1	Larmor frequency	18.1 MHz
1	Maximum depth acess	3.3 mm
1	Pulse length	8 µs
1	Echo time	32 µs
1	Acquisition window	5 µs
1	Number of echoes	128
1	Recycling delay	300 ms
1	Number of scans	1024
2	Larmor frequency	13.78MHz
2	Maximum depth access	20 mm
2	Pulse length	21 µs
2	Acquisition window	20 µs
2	Echo time	116 µs
2	Number of echoes	128
2	Recycling delay	900 ms
2	Number of scans	2048

3.4.2 Pottery

A total of 10 potteries from the ancient Rumanian civilization (3500 - 4000 years old) were studied through NMR relaxation in partnership with Prof. Dr. Mihai Vasilescu of the Babes-Bolyai University, Cluj-Napoca (Romania). They probably belonged to three different cultures: Komariw-Costisa / Midle Bronze Culture (samples P1, P2, P3, P4, P5 and P6); Trzniec / End of Early Bronze - Start of Middle Bronze (samples P7 and P8) and New Culture / Late Bronze (P9 and P10). Photos of each pottery sample are shown in Fig. 3.8.

The samples were immersed in deionized water for more than 24 hours, covered with parafilm and measured in a PM5 sensor with the parameters present in Table 3.6. They were profiled to a depth of 3 mm. At a depth where the water penetration was constant (2 mm), the T_2 decays were correlated with the elementary composition of the main pottery elements provided by Prof. Dr. Mihai Vasilescu, given in Table 3.7.

3.4.3 Parchment

A sheet of parchment owned by Prof. Dr. Bernhard Blümich from RWTH Aachen University (Germany) was investigated. It was originally the cover of a book from the 17^{th} century (Fig. 3.9(a)) which had suffered water damage and degradation over time. This parchment was measured with a PM2 connected to a Minispec spectrometer at three different damaged regions: a high-, a medium- and a low-damage position

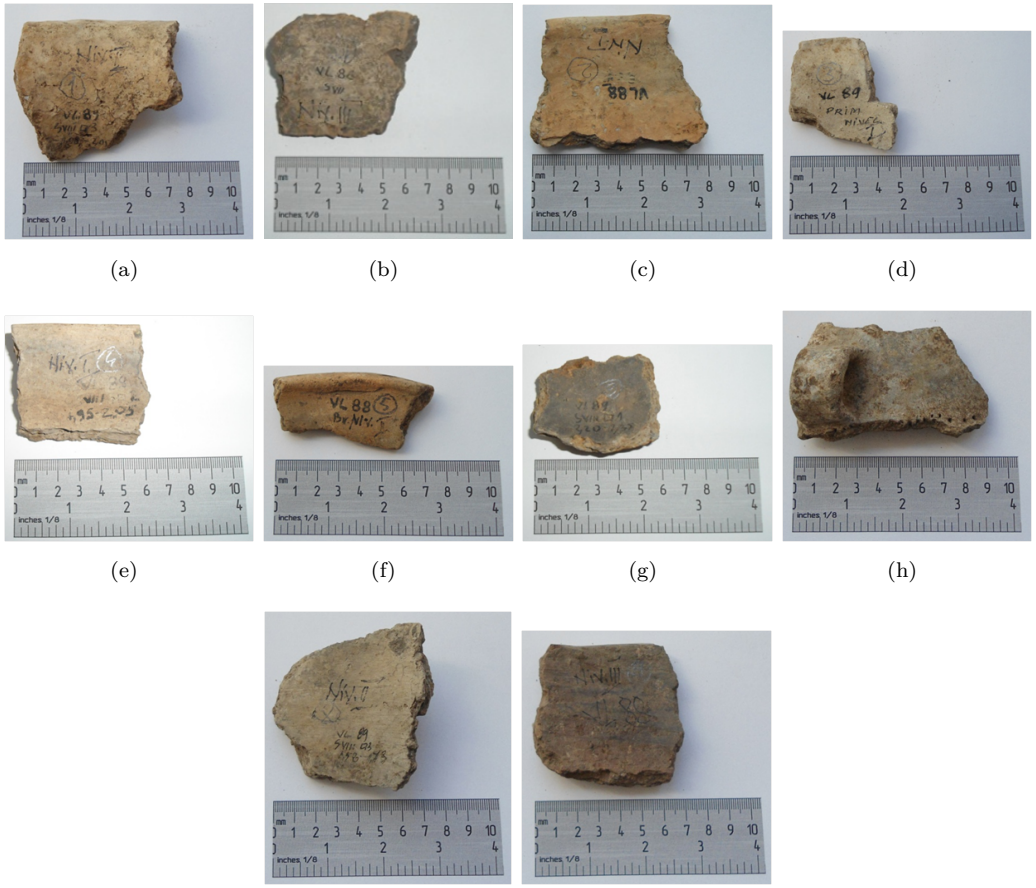

(a) (b) (c) (d)

(e) (f) (g) (h)

(i) (j)

FIGURE 3.8: Pottery samples. (a) Sample P1. (b) Sample P2. (c) Sample P3. (d) Sample P4. (e) Sample P5. (f) Sample P6. (g) Sample P7. (h) Sample P8. (i) Sample P9. (j) Sample P10.

TABLE 3.6: NMR parameters for the pottery experiment

Parameter	value
Larmor frequency	18.1MHz
Maximum depth access	3 mm
Pulse length	5µs
Echo time	35µs
Acquisition window	8µs
Number of echoes	128
Recycling delay	350 ms
Number of scans	256

[107]. The low-damage position was a spot where no damage could be seen, which presumably preserved the characteristics of the undamaged parchment, inluding its color. The medium-damage region was intermediate between the low- and high-damage levels. The high-damage position was the region that had suffered serious degradation over time by action of fungi or bacteria and exposure to climate factors such as humidity or sunlight, which made the parchment become darker, with some holes in its macroscopic

TABLE 3.7: Element weight of the potteries [%] provided by Prof. Dr. Mihai Vasilescu

Sample	Element [%]													
	O	C	Si	Al	Fe	P	Mg	K	Ca	Na	Ti	Mn	Cl	S
P1	39.30	10.03	21.84	5.18	4.95	1.13	1.54	1.69	13.61	0.4	0.33	0	0	0
P2	40.26	2.47	34.52	11.08	4.95	0.45	1.6	2.50	1.16	0.55	0.46	0	0	0
P3	37.68	8.08	32.59	8.67	1.94	0.30	0.72	3.01	4.30	1.53	0.65	0	0.29	0.24
P4	37.24	6.29	32.81	10.39	4.60	0.70	1.51	2.95	1.72	0.97	0.51	0	0.31	0
P5	39.58	2.73	36.41	10.10	5.07	0.00	1.48	2.47	0.93	0.67	0.56	0	0	0
P6	40.95	5.53	33.50	10.15	3.27	0.00	1.52	2.44	0.79	1.17	0.39	0	0.29	0
P7	41.33	14.53	13.64	5.25	3.33	1.87	1.15	1.19	12.37	1.02	0.18	3.85	0.29	0
P8	40.00	2.62	35.04	11.00	4.06	0.00	1.46	3.08	1.26	0.90	0.58	0	0	0
P9	41.10	14.60	25.18	9.28	3.13	0.00	1.62	1.68	0.85	1.89	0.25	0	0.42	0
P10	39.73	13.03	27.64	10.53	2.55	0.30	1.66	2.00	1.4	0.60	0.34	0	0.22	0

structure. This location was called parchment with water attack.

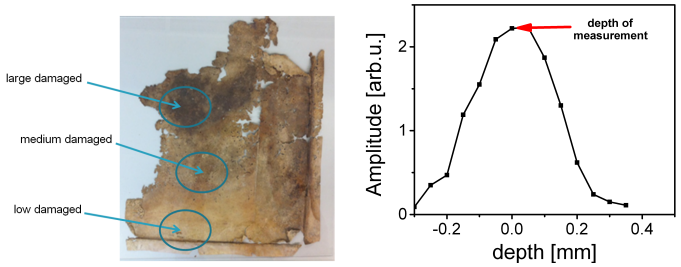

(a) (b)

FIGURE 3.9: (a) Water attacked parchment sheet. (b) Parchment profile.

Another series of untreated parchments were subjected to a chemical aging process consisted of cycles of immersion in a SO_2 solution (50 ppm) for 2 days, 172 k lux of light for 2 hours and heating at 100° C for 48 hours, in 1, 2, 4 and 8 cycles. For this reason, these samples were named 1, 2, 4 or 8 cycles, with SO_2 attack. A third kind of sample was a untreated parchment, and the last sample explored was a gelatine sample, made mainly of gelatinized collagen. These parchments and the gelatine sample were provided by Dr. Admir Masic, from the BAM Berlin (Germany) [21, 118].

The chosen pulse sequence was a bi-dimensional RRCOSY (T_1-T_2), with saturation-recovery for the T_1 and OW4 for the T_2 encoding, applied to the position of maximum signal acquired in a simple profile experiment (Fig 3.9(b)), at a location supposed to be the center of the parchment. A logarithmic scale step size for the T_1 encoding was calculated with Eq. 1.34, continuing through $5T_1$, and the data were transformed using a two-dimensional inverse Laplace algorithm. The acquired data also enabled one-dimensional analysis: selecting only the first or the average of the first four echoes of each OW4 decay resulted in a SR acquisition, or the last experiment with T_1 encoding time of $5T_1$ provided an OW4 decay. Such series of data were explored with mono and

bi-exponential curve fit, one-dimensional inverse Laplace algorithm and PLS models. The NMR parameters used are shown in Table 3.8.

TABLE 3.8: NMR parameters for the parchment experiment

Parameter	value
Larmor frequency	29.3 MHz
Maximum depth access	1.8 mm
Pulse length	2.2 µs
Echo time	24 µs
Acquisition window	4.5 µs
Number of echoes	128
T_1 steps	32
Recycling delay	1000 ms
Number of scans	2048
estimated T_1 for the SR sequence (H_2O attacked sample)	50 ms
estimated T_1 for the SR sequence (SO_2 attacked, untreated and gelatine samples)	80 ms
Number of experiments	8

3.4.4 Handmade paper

Hemp, rice and bamboo handmade papers (for illustration, rice paper samples are shown Fig. 3.10) were purchased at a traditional workshop in China by Dr. Zhou Hua of the Beijing Union University (China). They were kept in a dry heat box at a temperature of 105° C, for cycles of 15 days, from 0 (untreated) through 4 cycles, and then examined using a PM2 sensor guided by a Minispec spectrometer. A quick profile of the sample indicated the depth with highest signal, which was assumed to be the center of the paper (similar to the parchment procedure at Fig. 3.9(b)). Four measurements with the OW4 pulse sequence were performed with the NMR parameters, as summarized in Table 3.9.

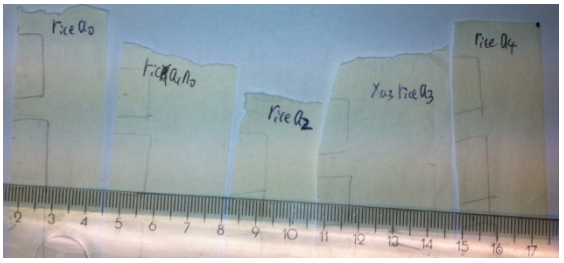

FIGURE 3.10: Rice paper samples.

All the acquired data had the first echo discarded and were analyzed using bi-exponential curve fits. Furthermore, the data were inserted into a chemometrix matrix with and without normalization by the first echo amplitude, and PLS models were created.

Table 3.9: NMR parameters for the handmade paper experiment

Parameter	value
Larmor frequency	29.3 MHz
Maximum depth access	1.8 mm
Pulse length	2.2 µs
Echo time	23 µs
Acquisition window	3.5 µs
Number of echoes	256
Recycling delay	1200 ms
Number of scans	16384
Number of experiments	4

3.4.5 Canvas linings

Six different canvas samples of interest to the Stichting Restauratie Atelier Limburg (SRAL) (Maastricht, Netherlands) were labeled from A to F and investigated (Fig. 3.11). Samples A, B, C, D and E were made of two layers of different materials glued together using different kinds of waxes, and sample F was just one layer of canvas with wax. All experiments were performed with a PM5 operated by a Kea 1 spectrometer (Magritek Ltd). The NMR-MOUSE was mounted on an automatic lift adjusted to 100 µm of spatial resolution. The NMR parameters are summarized in Table 3.10.

Table 3.10: NMR parameters for the canvas experiment

Parameter	value
Larmor frequency	17.1 MHz
Maximum depth access	3.00 mm
Pulse length	5 µs
Echo time	40 µs
Acquisition window	10 µs
Number of echoes	256
Recycling delay	200, 300, 500 or 600 ms
Step size	50 µm
Number of scans	1024

Preliminary measurements of sample A suggested a T_1 value of 100 ms, so the profiles were weighted by T_1 with some selected values of the recovery time for the CPMG pulse sequence: 200, 300 and 500 ms (600 ms for sample A). The data were examined as the addition of four, thirty-two echoes and the weighting function. Each canvas sample was measured with the written mark on the upper side, which means this side is placed at the highest depth.

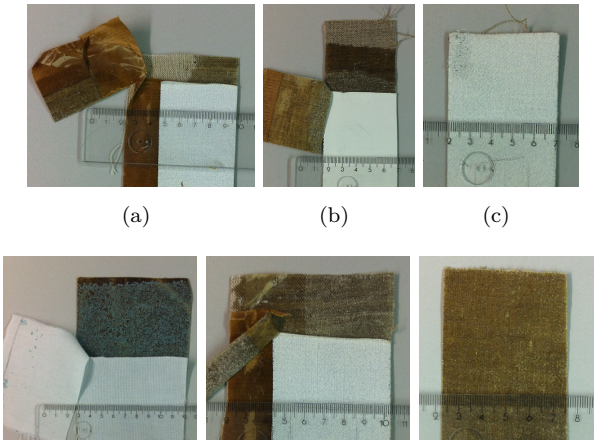

(a) (b) (c)

(d) (e) (f)

FIGURE 3.11: Canvas samples. (a) A. (b) B. (c) C. (d) D. (e) E. (f) F.

4. Results and discussion

The present chapter summarizes the results achieved through the proposed experiments with regard to new advances in polymer and cultural heritage sciences with the NMR-MOUSE. In section 4.1, the explored samples were polymers, such as HDPE pipes (subsection 4.1.1), HDPE blocks treated with β-radiation (subsection 4.1.2) and photo-polymerized dental resins (subsection 4.1.3). Section 4.2 presents the results obtained for cultural heritage samples, such as the consolidated sandstones (subsection 4.2.1), the ancient Rumenian potteries (subsection 4.2.2), the degraded parchment (subsection 4.2.3), the Chinese paper (subsection 4.2.4) and painting canvas (subsection 4.2.5).

4.1 Polymers

4.1.1 Heat fusion joining in HDPE pipes

No relevant variation of the relaxation times T_1 and T_2 could be determined for sample 10-008 in regions inside (A) or outside (B) of the join. The parameters extracted from bi-exponential fits are presented in Tab. 4.1.

TABLE 4.1: T_1 and T_2 for regions inside or outside of the join

parameter	region A	region B
Amplitude (T_1 long) [arb.u.]	18.2 ± 0.2	19.3 ± 0.2
T_1 long [ms]	261 ± 6	260 ± 6
Amplitude (T_1 short) [arb.u.]	4.2 ± 0.2	4.2 ± 0.2
T_1 short [ms]	22 ± 2	25 ± 2
Amplitude (T_2 long) [arb.u.]	15.8 ± 0.5	16.1 ± 0.6
T_2 long [ms]	0.83 ± 0.05	0.88 ± 0.04
Amplitude (T_2 short) [arb.u.]	28.7 ± 0.9	30.3 ± 0.8
T_2 short [ms]	0.082 ± 0.006	0.082 ± 0.004

However, a horizontal profile with a resolution of 2 mm, represented by the addition of the first 14 echoes (50% of the initial intensity) acquired in a CPMG pulse sequence optimizes the sensitivity of the measurement. A notable dip was reproduced three times for the sample 10-008 (Fig. 4.1(a)) and also observed for the samples 10-001

and 10-009 (Fig. 4.1(b) and (c)), where the zero position is the minimum amplitude position (the join) and the amplitudes are normalized by the maximum value.

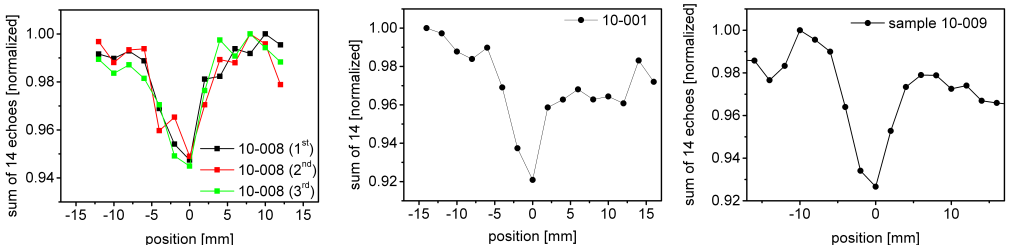

(a) (b) (c)

FIGURE 4.1: Horizontal profile of sample. (a) 10-008. (b) 10-001. (c) 10-009.

After defining the procedure, three positions for every pipe were chosen, one in the welding line (region A) and two outside the welding line (region B). These were scanned along the circumference in order to check the reproducibility along the dip and variations along the circumference (Fig. 4.2). In all cases, the amplitude plotted corresponds to the sum of the first 14 echoes acquired in a CPMG pulse sequence.

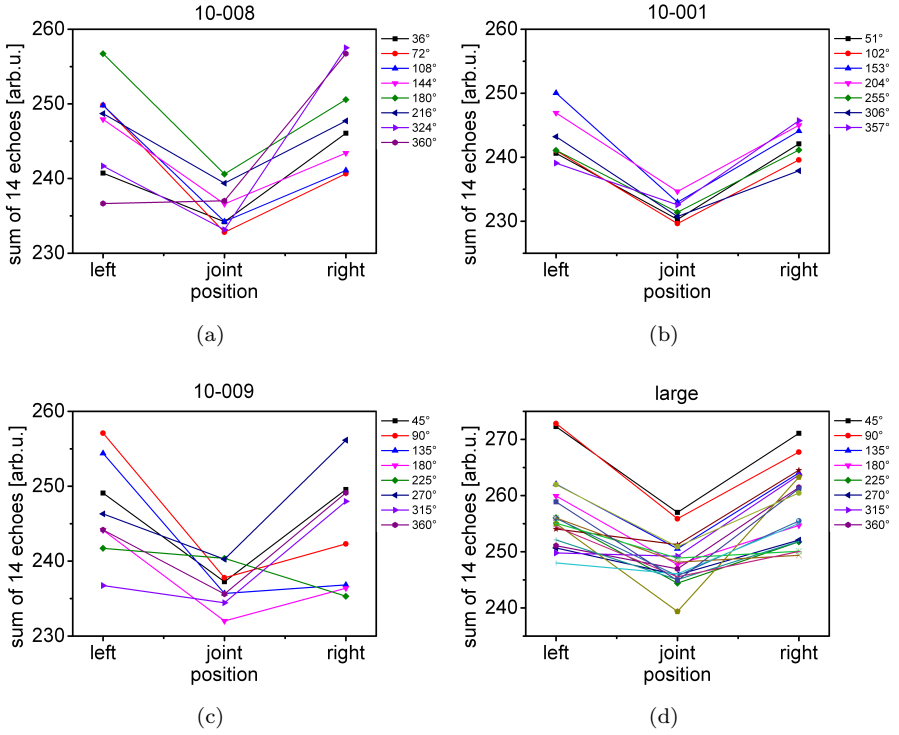

(a) (b) (c) (d)

FIGURE 4.2: NMR measurements along the circumference. (a) Sample 10-008. (b) Sample 10-001. (c) Sample 10-009. (d) Sample Large.

The NMR signal around the pipe circumference in region A for all pipes is shown in Fig. 4.3(a). Some signal fluctuations can be seen along the circumference, which indicates that more than systematic errors in the NMR signal, the pipe-making process

(for example, the imperfect cooling conditions and the statistics of the crystalline distribution) was responsible for producing inhomogeneous material and thus the signal fluctuations [119]. This phenomenon was also observed over a circumference far from the join of sample 10-008 (Fig. 4.3(b)) and over its longitudinal direction (Fig. 4.3(c)).

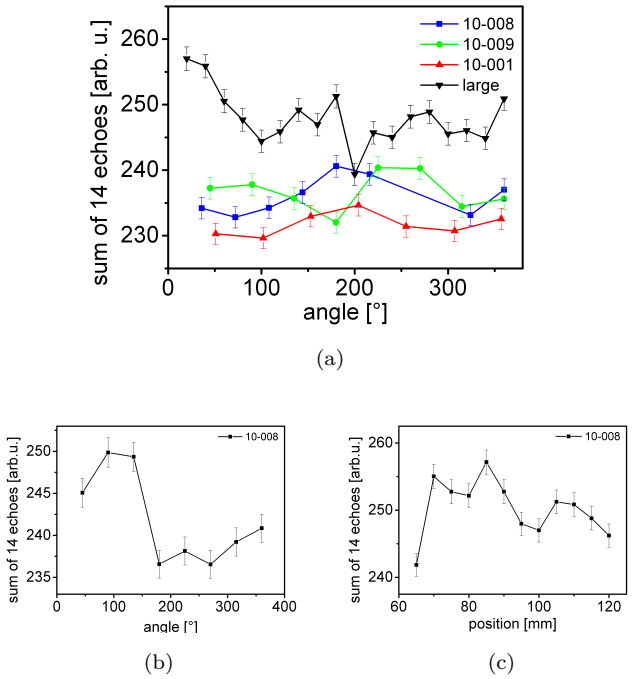

FIGURE 4.3: Signal amplitude in the welding line as a function of the angle for samples. (a) All pipes at the join. (b) Signal amplitude far from the welding line as a function of the angle for sample 10-008. (c) Signal amplitude in a longitudinal line for sample 10-008.

The sample inhomogeneity was further tested by means of statistical distribution along one circumferential line in region A and two lines adjacent to the welding line in region B, to the left and right sides of the join. For all pipe sections, the distributions exhibited in Fig. 4.4 consistently reveal lower NMR signal amplitude for region A as compared to region B.

The signal fluctuations in regions A and B reported in Fig. 4.4 can be approximated by Gaussian distributions. Figure 4.5 shows the signal intensity distributions along the circumference for the large pipe only; due to its larger size it had more than double the acquisition of the other pipes. The narrow width of the signal distribution at the join (region A) correlates with smaller error bars in Fig. 4.4. Table 4.2 lists the estimated widths and average values of the Gaussian distributions.

In summary, an important finding is that all pipes are inhomogeneous due to fluctuations of crystallinity within the sensitive volume of the NMR-MOUSE. These fluctuations are smaller along the welding line than in the thermally unaffected pipe

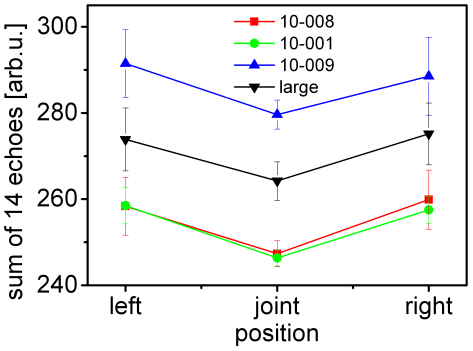

FIGURE 4.4: NMR signal averages for all pipes.

TABLE 4.2: Estimated widths of the NMR signal distributions for the large pipe

region	width [arb.u.]	center [arb.u.]
left (A)	100	252
join (B)	40	245
right (A)	100	253

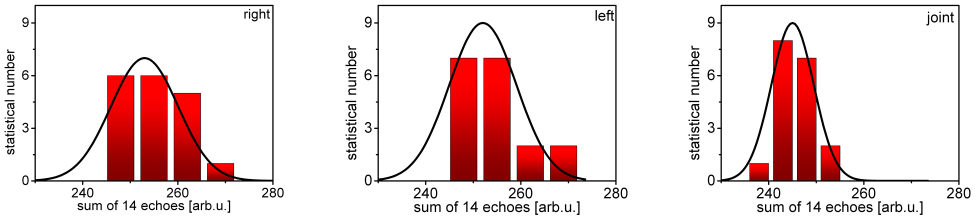

(a) (b) (c)

FIGURE 4.5: Distributions of NMR signals for the large pipe in the regions. (a) Right. (b) Left. (c) At the join.

material. An assessment of the overall quality of a welding line by NMR may be based on statistical averages and variances of NMR signals for the welding line and the thermally unaffected pipe material.

DSC measurements were performed in four other PE samples; a result example is presented in Fig. 4.6(a). Comparing the result with the value of the enthalpy of melting for a pure crystalline PE sample [120], their degree of crystallinity was calculated using Eq. 3.1. Thus, these samples were explored using the same NMR experimental conditions applied to the pipes. A straight line well explains the correlation between the level of crystallinity and the sum of echoes, as presented in Fig. 4.6(b), with coefficients presented in Table 4.3.

The NMR results presented in Figs. 4.4 and 4.5 can be expressed as a function of the polymer crystallinity percentage through the parameters summarized in Table 4.3. These results are shown in Fig. 4.7 and confirm that the heat fusion joining process

TABLE 4.3: Coefficients of Figure 4.6(b)

coefficient	value
Linear [%]	74.19 ± 0.08
Angular [%/arb.u.]	$(-59.0 \pm 0.4)10^{-3}$
$\bar{R}^2$	0.99987

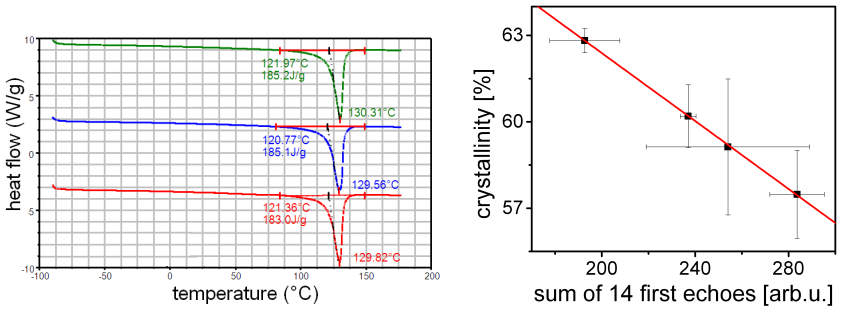

(a) (b)

FIGURE 4.6: (a) DSC result; (b) Correlation between the level of crytallinity and the NMR parameter.

for connecting pipes increases the crystallinity degree of the PE pipes to the values indicated in Table 4.4. The signal distribution at the join is narrow probably because of slow cooling, which is consistent with lower signal due to higher crystallinity.

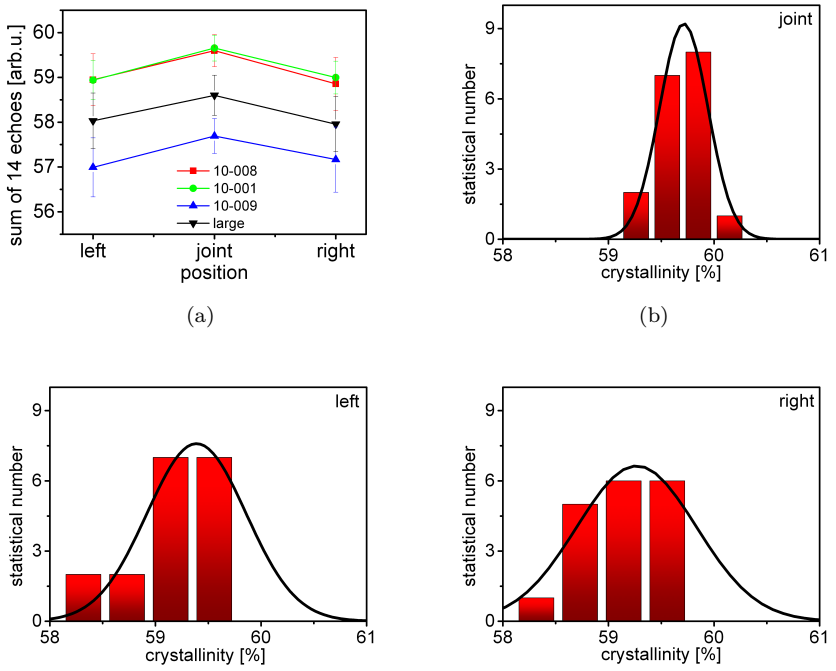

(a) (b)

(c) (d)

FIGURE 4.7: (a) Crystallinity averages for all pipes. Distributions of crystallinity for the large pipe in the different regions. (b) At the join. (c) Left. (d) Right.

TABLE 4.4: Estimated center and widths of the crytallinity distributions for the large pipe

region	center [%]	width [%]
B (left)	59.3 ± 0.2	0.9 ± 0.4
A (join)	59.71 ± 0.03	0.46 ± 0.07
B (right)	59.3 ± 0.1	1.1 ± 0.3

4.1.2 HDPE cross-linked with β-radiation

All of the PE samples were explored using infrared spectroscopy. The acquired spectra are presented in Fig. 4.8(a); Fig. 4.8(b) zooms in on the range of 1800 to 1500 cm^{-1}. Although it is very noisy, the integral over the range of the alkene vibration modes 1700 to 1600 cm^{-1}, as shown in Fig. 4.8(c)), indicates a quantitative decrease in the covalent bonds and increase in the cross-link density due to absorption of β radiation.

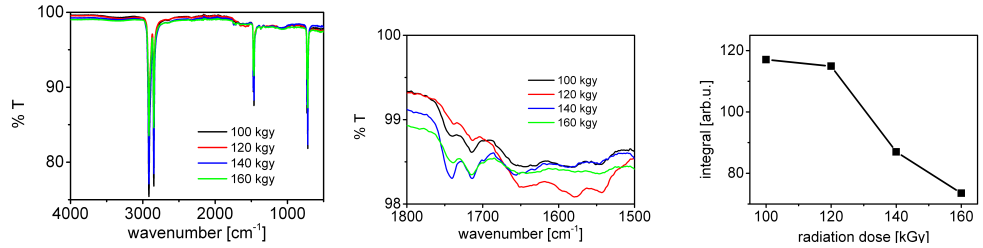

FIGURE 4.8: Infrared spectra of the PE samples treated with β radiation. (a) Full spectra. (b) Zoomed-in vinyl vibrational groups range. (c) Integral over 1700 to 1600 cm^{-1}, the vinyl vibrational groups.

Figure 4.9(a) shows the amplitude and Fig 4.9(b) the decay constants of the data acquired with the CPMG pulse sequence and fitted with a mono-exponential model. The straight line crossing the points in both figures resulted from a linear correlation of the NMR parameters and the absorbed radiation dose, with the coefficients presented in Table 4.5.

TABLE 4.5: Coefficients of the straight line in Fig 4.9.

Variable	coefficient	value
amplitude	linear	16.4 ± 0.3 arb.u.
amplitude	angular	0.003 ± 0.002 arb.u./kGy
amplitude	$\bar{R}^2$	0.03183
T_2	linear	0.299 ± 0.005 ms
T_2	angular	$(-4 \pm 4)10^{-5}$ ms/kGy
T_2	$\bar{R}^2$	0.0033

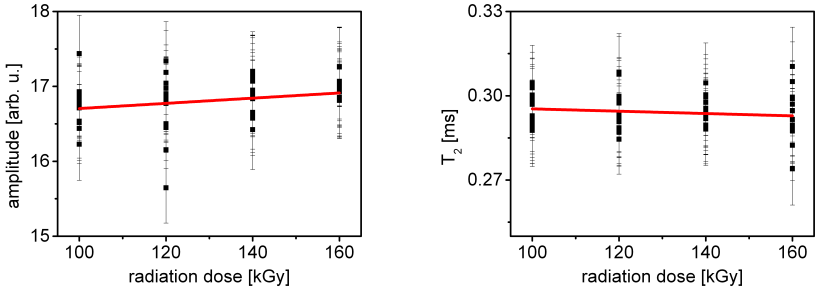

(a) (b)

FIGURE 4.9: Monoexponential fit constants of the CPMG decays. (a) Amplitude. (b) Decay constants. The straight line coefficients are summarized in Table 4.5.

As presented in Table 4.5, the angular coefficients are almost null and are easily confused with the standard deviation, which indicates the impossibility of distinguishing the samples through application of a mono-exponential fit model to the CPMG data. The same data were fitted with a bi-exponential function, which was more accordance with the relaxation theory of polymers [11]. In this way, the four parameters (amplitudes for the short and long components and the respective relaxation times) are presented in Fig. 4.10. As above, the straight lines are a linear fit for the involved variables, with coefficients presented in Table 4.6.

The spins from the rigid domains of a semi-crystalline polymer are expected to relax quickly, and are not acquired during this experiment. Thus, the fitted components are attributed to the more amorphous domains, such the the semi-rigid (short component) or soft (long component) domains, as discussed in chapter 1.2. In fact, the short components frequently have high amplitudes due dead time weighting, so the extrapolation leads to contamination in the magnetization of the zero time.

TABLE 4.6: Coefficients of the straight line in Fig 4.10.

Component	variable	coefficient	value
long	amplitude	linear	6.5 ± 0.2 arb.u.
long	amplitude	angular	0.008 ± 0.002 arb.u./kGy
long	amplitude	$\bar{R}^2$	0.26944
long	T_2	linear	0.77 ± 0.02 ms
long	T_2	angular	$(-5 \pm 2)10^{-4}$ ms/kGy
long	T_2	$\bar{R}^2$	0.11699
short	amplitude	linear	14.4 ± 0.4 arb.u.
short	amplitude	angular	0.021 ± 0.004 arb.u./kGy
short	amplitude	$\bar{R}^2$	0.45786
short	T_2	linear	0.109 ± 0.003 ms
short	T_2	angular	$(20 \pm 2)10^{-5}$ ms/kGy
short	T_2	$\bar{R}^2$	0.50885

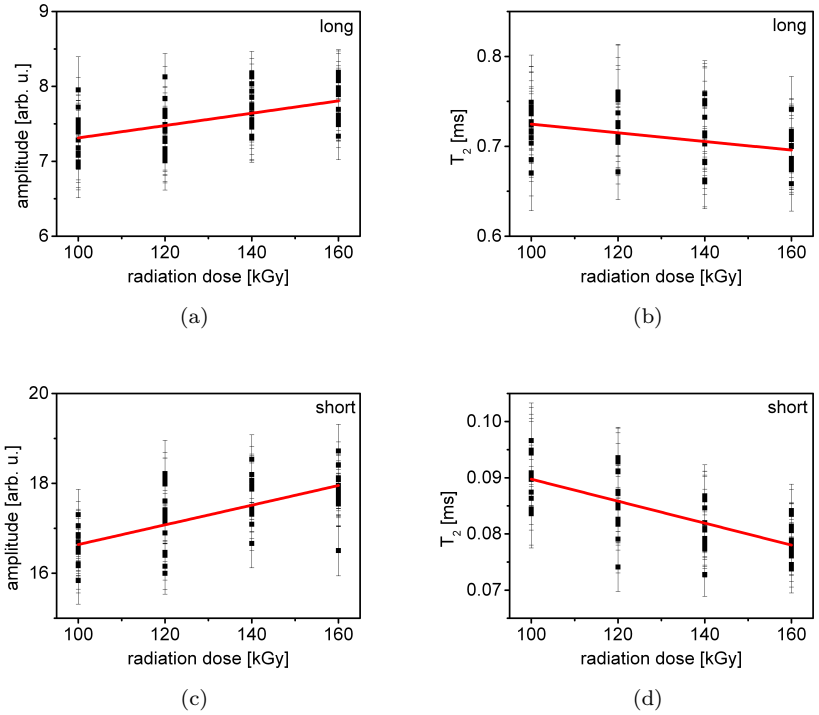

FIGURE 4.10: Bi-exponential fit constants of the CPMG decays. (a) Amplitude for the long component. (b) Decay constants for the long component. (c) Amplitude for the short component. (d) Decay constants for the short component. The straight line represents a linear curve fit adjusted to the data and the coefficients are summarized in Table 4.6.

From the data presented in Table 4.6 and Figure 4.10 a shorting trend can be seen in both relaxation times with the increment of the absorbed dose. However, since there is still a large discrepancy in the results, the correlation coefficient is small, and the correlation is moderate for the long component ($\bar{R}^2 = 0.51$) and weak for the short component ($\bar{R}^2 = 0.12$).

Solid echoes generated by the OW4 pulse sequence were also explored [43, 47]. The spin response of 20 measurements with the OW4 pulse sequence at different depths and positions were interpolated with a mono-exponential function. The amplitude and decay constants are presented in Fig. 4.12. Once again, the straight line indicates a linear correlation, with coefficients given in Table 4.7, which suggests that both $\bar{R}^2$ are near zero, which indicates the absence of correlation for magnetization amplitude or decay constants with mono-exponential fits.

A bi-exponential model could better explain the relaxation, and was also applied to the OW4 data. The extracted parameters are listed in Fig. 4.12, with the linear correlation coefficients presented in Tab. 4.8. Again, no bi-exponential parameter of the OW4 data could classify the samples.

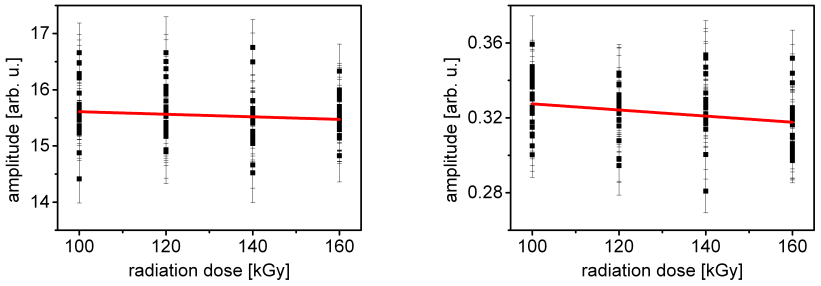

(a) (b)

FIGURE 4.11: Mono-exponential fit constants of the OW4 decays. (a) Amplitude. (b) Decay constants. The straight line coefficients are summarized in Table 4.7.

TABLE 4.7: Coefficients of the straight line in Fig 4.11.

Variable	coefficient	value
amplitude	linear	15.8 ± 0.3 arb.u.
amplitude	angular	-0.002 ± 0.002 arb.u./kGy
amplitude	$\bar{R}^2$	-0.00089
T_2	linear	0.34 ± 0.01 ms
T_2	angular	$(-16 \pm 8)10^{-5}$ ms/kGy
T_2	$\bar{R}^2$	0.04

TABLE 4.8: Coefficients of the straight line in Fig 4.12.

Component	variable	coefficient	value
long	amplitude	linear	7.1 ± 0.3 arb.u.
long	amplitude	angular	-0.005 ± 0.002 arb.u./kGy
long	amplitude	$\bar{R}^2$	0.06716
long	T_2	linear	0.81 ± 0.04 ms
long	T_2	angular	$(1 \pm 3)10^{-4}$ ms/kGy
long	T_2	$\bar{R}^2$	-0.01089
short	amplitude	linear	18.4 ± 0.6 arb.u.
short	amplitude	angular	-0.004 ± 0.004 arb.u./kGy
short	amplitude	$\bar{R}^2$	0.00239
short	T_2	linear	0.079 ± 0.005 ms
short	T_2	angular	$(4 \pm 4)10^{-5}$ ms/kGy
short	T_2	$\bar{R}^2$	0.00079

Overall, the PE samples with different amounts of radiation dose explored do not show enough differences in cross-link density to be distinguished distinguish among them using a relaxation experiment with the NMR-MOUSE. The amplitudes and relaxation times fitted by mono or bi-exponential models were always imprecise, and the average value did not show correlation with the quantity of absorbed dose. Supposing the sample to be homogeneous, an explanation for the broad values is the presence of noise, which could be masked using techniques of multi-variate analysis. Therefore, the first 64 echoes of the decay-acquired CPMG and OW4 data were inserted into a chemometrics table,

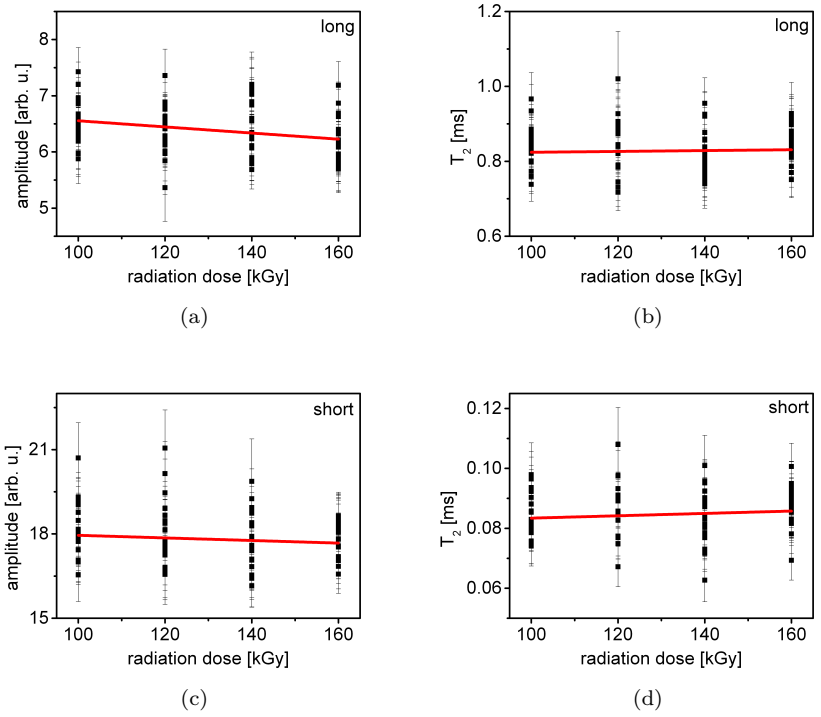

FIGURE 4.12: Bi-exponential fit constants of the CPMG decays. (a) Amplitude for the long component. (b) Decay constants for the long component. (c) Amplitude for the short component. (d) Decay constants for the short component. The straight line coefficients are summarized in Table 4.8.

with the magnetization received for each echo time in a cell element as the dependent variable (x-variable). The control variable was the radiation dose (y-variable).

The model coefficients, as described in Appendix A, are presented in Table 4.9 and indicate low correlation between the variables for the OW4 pulse sequence, and moderate correlation for the CPMG data. Furthermore, the predicted amount of absorbed radiation dose for each acquired decay is shown in Figs. 4.13(a) and (c). It is notable that the OW4 pulse sequence may produce predicted values with discrepancy window of about 40 kGy, or errors of ±20 kGy, while the CPMG sequence offers better prediction, with discrepancy window of about 30 kGy, or deviations of ±15 kGy, which are enough to distinguish between samples with absorbed doses of 100 and 160 kGy. The loadings presented in Figs. 4.13(b) and 4.13(d) indicate that both of the two latent variables have differences that are present in the initial echoes, with a decay constant of about 30 μs; i.e., the loadings prove changes in the rigid domains of the polymer chains. As the dead time effects do not allow acquisition of the rigid component spin response, it is hard to discriminate these samples with a unilateral NMR experiment.

The transverse magnetization decay acquired by the pulse sequence CPMG or OW4 was able to distinguish moderately well between the samples tested and confirm

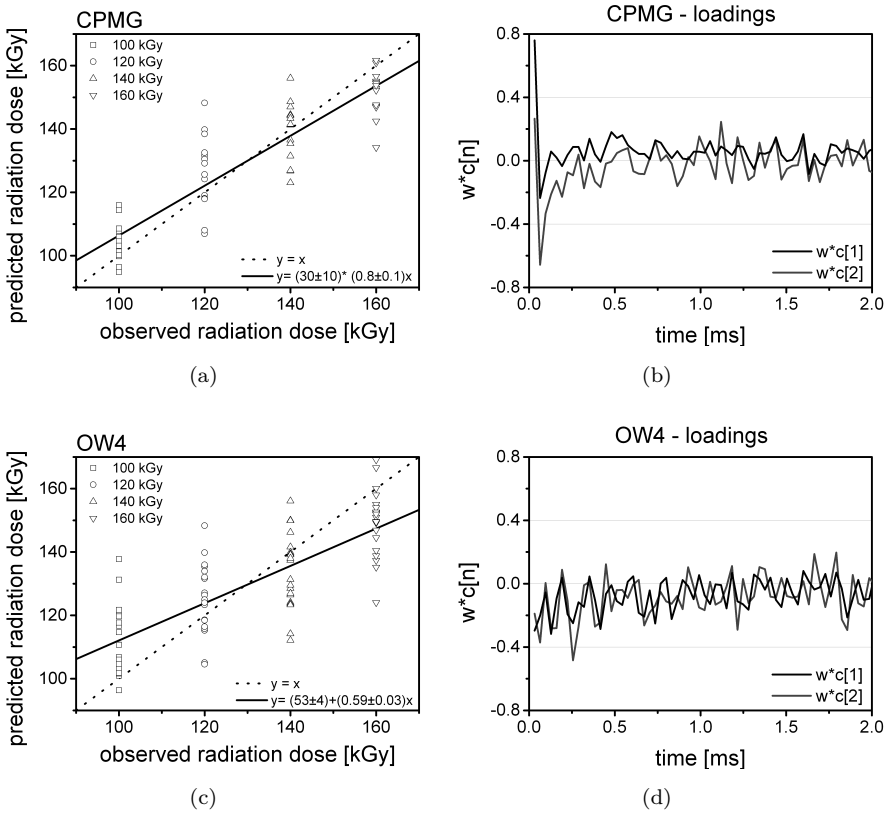

FIGURE 4.13: PLS analysis for HDPE samples treated with β-radiation. (a) Predicted data for the CPMG pulse sequence. (b) Loadings of the data acquired with the CPMG sequence. (c) Predicted data for the OW4 pulse sequence. (d) Loadings of the data acquired with the OW4 sequence.

TABLE 4.9: Fitted coefficients of Fig 4.13.

sequence	LV1		LV2	
	R^2	Q^2	R^2	Q^2
CPMG	0.558149	0.371987	0.787728	0.504971
OW4	0.40178	0.119114	0.604566	0.216846

the low confidence in discriminating the samples using this methodology. Both of the mono-exponential fitted data are broadcast, and no trend can be seen. A small correlation can be seen in the bi-exponential fitted data that suggests a decrease of the T_2 long component over the increase of the absorbed radiation dose, evidence of increasing molecular motion. This behavior is more pronounced for the sequence CPMG than for OW4. The PLS fit model similarly indicates a broad distribution of the predicted data, with better prediction when using the CPMG pulse sequence. However, it also indicates grouping of samples with different absorbed radiation doses, which can be attributed to the tendency of the cross-link density to increase when the radiation dose increases. The loadings suggest high differentiation at times of 30 μs. Also, the PLS model fitted for the CPMG decays is enough to distinguish very well between the samples with radiation

doses of 100 and 160 kGy, as can be observed in Fig. 4.13(a); i.e., this model enables the distinction of small doses of the absorbed radiation.

4.1.3 Photo-polymerization of dental resins

Due to the short measurement time window of 25 s, the CPMG decays of a dental resin sample do not have a good signal-to-noise ratio, as illustrated in Fig. 4.14(a) (sample Arabesk, slice position at 1.2 mm). In fits with exponential decays, the fit parameter's amplitude and relaxation time show errors exceeding 30 %. Therefore, they could not be used to track the reaction. On the other hand, the echo sum has a sufficiently good signal-to-noise ratio for that purpose; echoes until a half of the initial amplitude were co-added. Figures 4.14(b) and (c) summarize the echo sums of the two dental resin composites as functions of time and depth, corresponding to the distance from the light source.

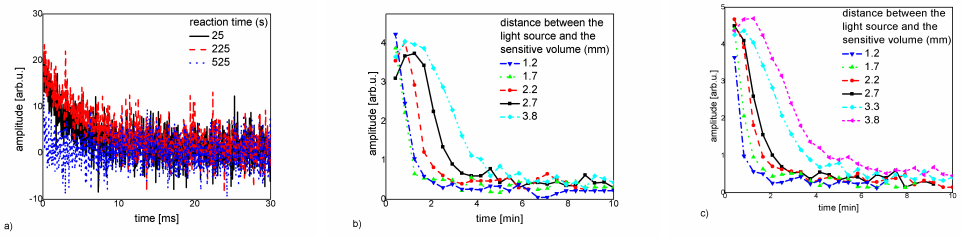

(a) (b) (c)

FIGURE 4.14: (a) Time dependent CPMG decays of the Arabesk sample, at slice position of 1.2 mm. (b) Sums of the first 64 echoes in the CPMG detection trains at different depths versus the curing time by means of single-sided NMR for the Arabesk sample. (c) Sums of the first 64 echoes in the CPMG detection trains at different depths versus the curing time by means of single-sided NMR for the Grandio sample.

Two different time periods can be discriminated in the curing curves depicted in Figs. 4.14(b) and (c): 1) an initiation phase, and 2) a curing phase. The duration of the initiation phase increases with increasing depth, as the light, which initiates the reaction, is more attenuated. The subsequent curing process conforms to Eq. 1.58, with a reaction rate constant that decreases with increasing distance from the light source. To describe the complete curing curves, two new terms were empirically included in Eq. 1.58: *term* 1 encompasses the signal increase, which takes into account the temperature change during the initiation phase, and *term* 2 represents an experimental offset C yielding:

$$[M][t] = [M]_0 \underbrace{\frac{2}{3}\left(\frac{t\_t_0}{\tau}\right)^{3/2}}_{term1} \exp\left[-\frac{2}{3}\left(\frac{t\_t_0}{\tau}\right)^{3/2}\right] + \underbrace{C}_{term2} \tag{4.1}$$

Differentiation of Eq. 4.1 provides the time when the NMR signal achieves its maximum value:

$$t_{\mathtt{max}} = \left(\frac{3}{2}\right)^{\frac{2}{3}} \tau + t_0 \tag{4.2}$$

Figure 4.15(a) shows examples of fits of the experimental data by Eq. 4.1 for the Arabesk sample at depths of 1.7 and 3.8 mm ($R^2 > 0.98$), with all parameters as variables. The spatial dependence of the maximum signal with the relative error bars is presented in Fig. 4.15(b). It is shown below that a constant value for the initial monomer concentration $[M]_0$ is found for all depths, and the reaction time constants τ depend exponentially on depth, as expected based on Eqs. 1.57, 1.59 and 4.1.

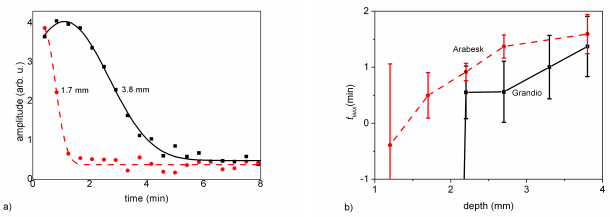

(a) (b)

FIGURE 4.15: (a) Signals selected for the Arabesk sample from Figures 4.14(b) and (c) and fitted using Eq. 4.1. (b) Relations among the maximums of signal, time and depth.

- THE INITIATION PHASE

  In the initial phase of the reaction, shown in Figs. 4.14(b) and 4.14(c), the NMR signal amplitude grows up to a maximum. This signal increase is attributed to the increase in molecular mobility due to rising temperature. This means that less signal is lost during the dead time of the NMR-MOUSE.

  The effect of temperature was investigated in a series of experiments in which a temperature sensor was placed underneath samples of different thicknesses, and the temperature was monitored as a function of the curing time (Fig. 4.16). In these experiments the light intensity was the same as in the NMR experiments. The initial rise in temperature matches the NMR signal rise well. After reaching the maximum temperature, the subsequent cooling is slow, and one can assume a constant temperature for the subsequent analysis.

- THE CURING PHASE

  In the curing phase, the decay of the echo sum shows the same time dependence as the monomer concentration in Eq. 4.1. The characteristic time constants $\tau(d)$ are

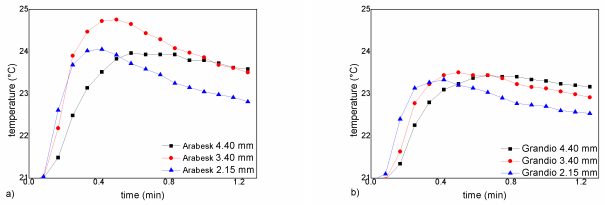

(a) (b)

FIGURE 4.16: Temperature as a function of reaction time for different sample thicknesses, normalized to a common initial temperature: (a) Sample Arabesk. (b) Sample Grandio.

related to the constant $K(d)$ according to Eq. 1.59. They both depend exponentially on the depth d (Fig. 4.16). However, the characteristic time constants at low depths close to the surface do not follow the exponential trend due the absence of a signal maximum and result in some difficulties for tracking the reaction at high reaction rates with good accuracy. Therefore, the first points were discarded.

Figure 4.17 summarizes the decay and reaction speed constants of the magnetization during the steady state of the polymerization reaction as a function of depth into the sample. The experimental reaction speed constants are in accordance with Eq. 4.1 and the associated decay constant is the extinction coefficient α (Tab. 4.10). For both Arabesk and Grandio, the extinction coefficients determined by NMR agree well with the ones directly determined by optical transmission measurements (OTE).

While reaction time τ and reaction rate constant K approximately follow exponential laws at depths exceeding 2 mm, their values at shallow depths are strongly impacted by fast temperature changes in the sample at these depths and the limited time resolution of the experiment. The same applies to the time lags in Fig. 4.15(b). These data points are therefore characterized as outliers and are neglected in the determination of the extinction coefficient α from Eq. 1.57 (Tab. 4.10).

TABLE 4.10: Extinction coefficients extracted from Fig. 4.17 and determined by optical transmission experiments (OTE)

sample	$\alpha_{\mathtt{NMR}}$ $[\mathtt{m}^{-3}]$	$\alpha_{\mathtt{OTE}}$ $[\mathtt{m}^{-3}]$
Arebesk	0.7 ± 0.1	0.64 ± 0.03
Grandio	0.7 ± 0.2	0.60 ± 0.03

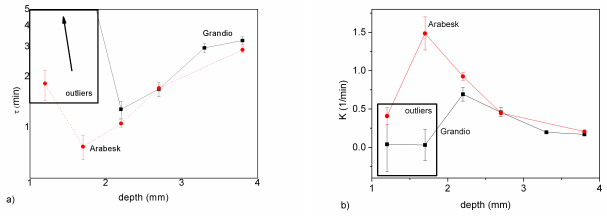

(a) (b)

FIGURE 4.17: (a) The characteristic constant τ of reaction. (b) The reaction constant K at different depths, extracted from Fig. 4.14; the outliers are indicated.

4.1.4 Summary

The results presented in section 4.1 represent progress regarding utilization of unilateral NMR sensors in evaluating polymer materials. Although we were unable to detect spatial defects caused by heat fusion in joined HDPE pipes, the results showed that the pipe join has a crystallinity degree higher than the pipe material, as expected. The cross-link density in PE samples could be ascertained better by the CPMG pulse sequence than with the OW4, because the the signal differences lies in the rigid domains, located at the very beginning of the magnetization decay, and are better understood with the help of multi-variate data analysis. The kinetics and depth dependence of a photo-curing reaction of a dental resin were explored with the NMR-MOUSE sensor and interpreted with adapted equations extracted from polymer books.

4.2 Cultural heritage

4.2.1 Consolidated sandstones

The profiles made to a depth of 3.3 mm using co-addition of 4 echoes, producing up to 80% of the initial magnetization intensity, what the results are presented in Fig. 4.18(a). The presence of a common peak in all the soaked samples was noted and attributed to the presence of a parafilm cover layer that may retain water on the cover surface. The signal from the water would then be aggregated with some spin response coming from the parafilm material itself. The anomalous peak of the blank sample arises from the fact that the untreated surface experiences high surface water accumulation and adsorption caused by the presence of a huge number of water molecules. The consolidation process causes changes in the material, reducing its water accumulation layer. Therefore, no film is observed on the reinforcing rock surfaces: the nano-material dissolved in alcohol produces a chain with hydrophobic properties. In order to understand the behavior of

the water at the sample surface, the measured depths between 1 and 3 mm are showed separately in Fig. 4.18(b).

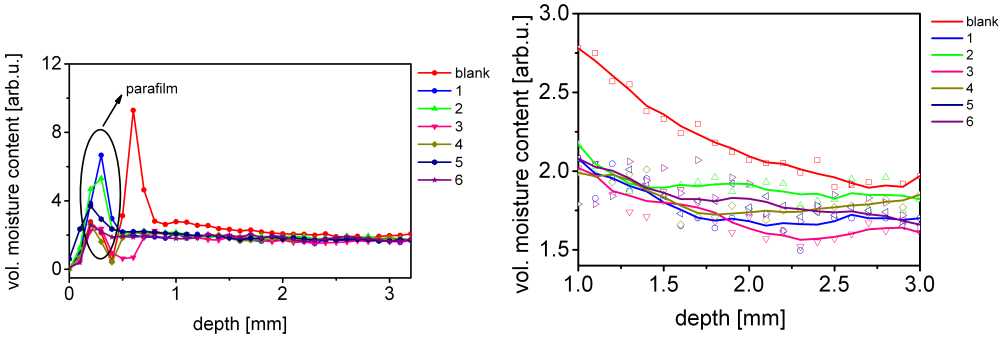

FIGURE 4.18: The short (3 mm) profile of the sandstones. (a) Full profile. (b) Zoom in 1-3 mm of depth; the lines represent the moving average filter, which is the mean of four consecutive points.

The trend of the curves present in 4.18(b) was accompanied, in a first approximation, by mono-exponential curve fits. The coefficients are shown in Table 4.11. The decay rate can be organized in a descending order as: blank $>$ 5 $>$ 3 $>$ 1 $>$ 4 $>$ 2 $>$ 6; the amplitudes can be organized in a descending order as: blank $>$ 3 $>$ 1 $>$ 5 $>$ 4 $>$ 2 $>$ 6; the decay of sample 6 does not look like an exponential decay. These results show that sample blank has the largest decrease in water amount from the surface to the inner layer, and all the consolidation solutions reduce this water amount until depths lower than 3.0 mm (except for treatment number 5). The water amount that remains in the stone is given by the offset, and suggests that consolidation process number 3 is the treatment that ensures the least water inside the sample.

TABLE 4.11: Exponential fit coefficient of the short profile, from 1 to 3 mm, as presented in Fig. 4.18(b)

sample	offset [arb.u.]	amp. at 1 mm [arb.u.]	decay const. [mm]	R^2
blank	1.81 ± 0.05	1.0 ± 0.5	0.8 ± 0.1	0.96724
1	1.66 ± 0.04	0.40 ± 0.07	0.4 ± 0.2	0.60269
2	1.86 ± 0.02	0.30 ± 0.07	0.14 ± 0.07	0.51613
3	1.59 ± 0.05	0.45 ± 0.06	0.5 ± 0.2	0.71717
4	1.76 ± 0.03	0.29 ± 0.06	0.3 ± 0.2	0.51536
5	1.68 ± 0.05	0.40 ± 0.05	0.8 ± 0.3	0.79784
6	1.90 ± 0.05	0.002 ± 0.009	-0.4 ± 0.4	0.22502

Even though the short profile was able to classify the different aspects of the consolidation solutions, a deeper profile would improve the experiment. The sensor PM25 could access depths up to 20 mm, which meant that the sensitive volume could cross the full volume of the sample blank, because it is thinner than 20 mm, and almost the full volume of the treated and aged sample. The profiles with $a = 4$ in Eq. 1.43 cover

the decay until about 50% of the initial intensity and represent the volumetric moisture content at the given depths. These profiles are presented in Fig. 4.19(a). The profiles with $b = 32$ in Eq. 1.44 summed all the echoes, until the magnetization reaches the noise level. So this profiles represent the averaged T_2 and is proportional to the average pore size through the correlation shown in Eq. 1.41. These profiles are presented in Fig. 4.19(b). Furthermore, the weighting function defined by Eq. 1.46 was calculated with $i_{\mathtt{i}}$=1, $i_{\mathtt{f}}$=4, $j_{\mathtt{i}}$=5 and $j_{\mathtt{f}}$=32, and the resulting profiles are presented in Fig. 4.19(c). In all three figures, the presence of a peak attributable to the parafilm cover can once more be seen. These profiles do not reveal the small differences observed in Fig. 4.18 due the big step size.

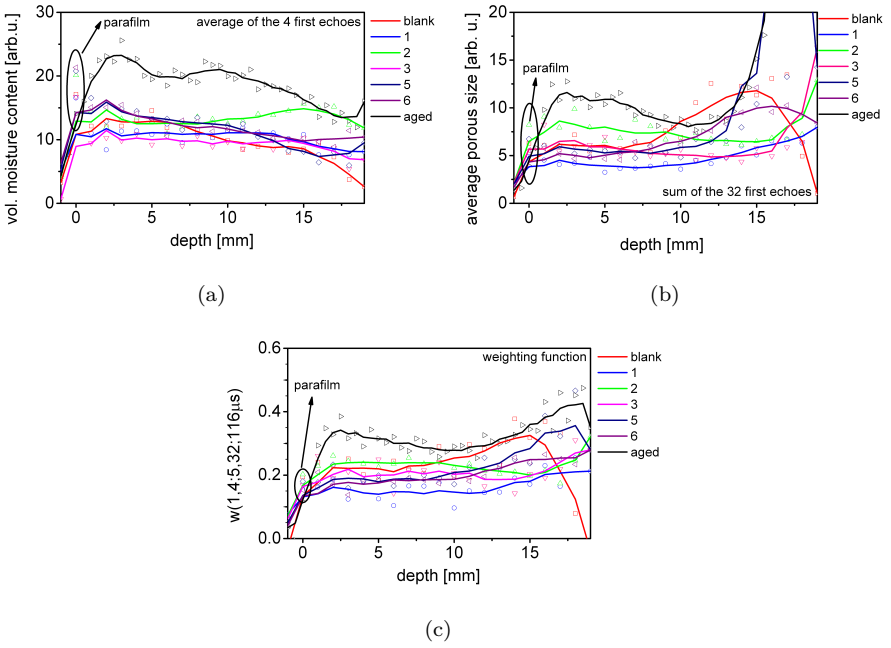

FIGURE 4.19: The long (20 mm) profile of the sandstones. The lines represent the moving average filter, which is the mean of four consecutive points. (a) Sum of the first 4 echoes. (b) Sum of the first 32 echoes. (c) Weighting function.

It is noted in Fig. 4.19(a) that the consolidation process present in samples 1 and 3 results in the lowest volume of moisture content and the process number of samples 2, 5 and 6 reduced the porosity quite well; due to systematic errors no better grouping could be realized. Moreover, the average pore size shown in Fig. 4.19(b) suggests that the consolidation process of sample 1 produces the smallest pore size of all the investigated processes. The high values seen mainly in the naturally aged sample below a depth of 13 mm arise from the small magnetization value and the propagated errors, with the normalization suggested by Eq 1.44. Figure 4.19(c) shows results similar to those seen in Fig. 4.19(b) but eliminates the high values caused by normalization.

In both versions of Fig. 4.19 the presence of a layer with water accumulation in

the natural stone can be seen; it is attributed to the equilibrium between the moisture in and outside of the sample, which results in a notably broad layer of water with width of about 4 mm. The reason that this peak does not appear in the deeper profile of the blank sample is that the spatial resolution of the deeper profile is larger than the water accumulation layer thickness in Fig. 4.18.

These results indicate that the pure solvents isopropanol and ethanol are best suited for consolidation treatments with crystals of $Ca(OH)_2$. Furthermore, they validate the NMR-MOUSE as a feasible tool for evaluating porosity and pore-size distribution in stones of cultural interest due to the non-destructiveness of the method. For the first time, this technique has been applied for Chinese sandstone artifacts and may make new measurements *in situ* in the Yungang Grottoes.

4.2.2 Relaxation in pottery

The pottery profiles calculated with the sum of 32 echoes are presented in Fig. 4.20(a). It is notable that after a depth of 1 mm the signal has an apparently constant trend, which can group the potteries as presented in Table. 4.12. The samples do not group according to geographical region.

TABLE 4.12: Potteries grouped as a function of the profile amplitudes at depths higher than 1 mm

amplitude [arb.u.]	sample
0.9	P1, P2, P10
1.5	P7, P8, P9
3.0	P4
5.0	P3, P5, P6

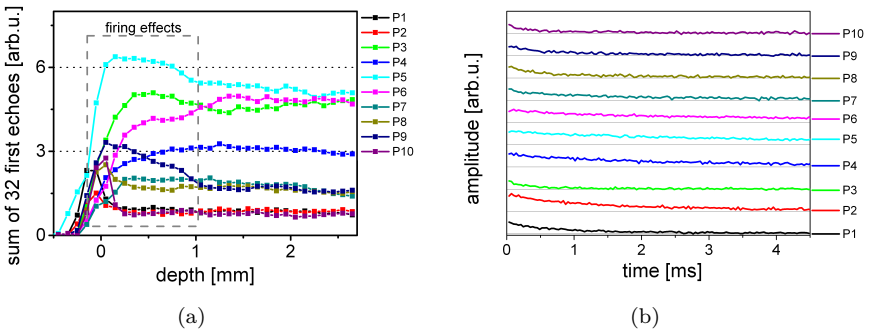

(a) (b)

FIGURE 4.20: (a) Pottery profiles. (b) Decays at 2 mm.

Furthermore, all the decays acquired for the CPMG pulse sequence at 2 mm, as shown in Fig. 4.20(b), were inserted into a chemometrics matrix. The elementary composition elemental composition was centered about the mean to best illustrate the

variation between samples. The PLS models were fitted with the independent variables as being the elementary composition presented in Table 3.7. Figure 4.21(a) summarizes all the model explained variation coefficients R^2 and the prediction coefficient Q^2. It is notable that C, Si, Al, Fe and Mg have positive Q^2, i.e., significant models; however, only Fe and C present good models. Thus, these last two elements were examined in separate models, with each element being the only y-variable in its model. The model coefficients are given in Table 4.13.

TABLE 4.13: PLS of the pottery

Element	LV1		LV2		LV3	
	R^2	Q^2	R^2	Q^2	R^2	Q^2 (LV3)
C	0.364046	0.272284				
Fe	0.441406	0.246204	0.766882	0.48554	0.965527	0.535293

The observed percentage of elemental masses shown in Tab. 3.7 and their values as predicted by the PLS model are presented in Fig. 4.21(b) for carbon and Fig. 4.21(d) for iron. This kind of plot represents a good model when the points are close to the $y = x$ line, as seen in Fig. 4.21(d). The explanation for why these elements yield good models lies in the fact that iron and old carbon (carbon black) are paramagnetic elements, thus they influence the transverse magnetization acquired during a CPMG experiment. From Fig. 4.21(c), the loading of the carbon PLS model, it is understood that there is a negative correlation between the carbon mass and the magnetization amplitude decays of the pottery and all the acquired echoes are important to explain the correlation.

Figure 4.21(e) shows that a similar phenomenon also happens for the first latent variable in the iron model, which explains 44% of the variance, although in this case the correlation is positive. The second latent variable explains an additional 32.5% of the variation and is important only at the beginning of the decay, until 1.2 ms, so this variance may be related to a fast decay component. The third latent variable is random, which indicates white noise.

It has previously been demonstrated that changes in the transverse relaxation time depend on the pottery composition. The T_2 measured in a single-sided NMR experiment, together with multivariate data analysis, in particular PLS models, were shown to be able to correlate information regarding the elemental composition of ancient potteries. A negative correlation implies a reducing and shortening of the decay with increasing carbon and iron content. This introduced method represents a scientific advance because it uses a fast and cheap measurement to non-invasively predict Fe and C amounts in the sample, with a high degree of accuracy for the Fe element.

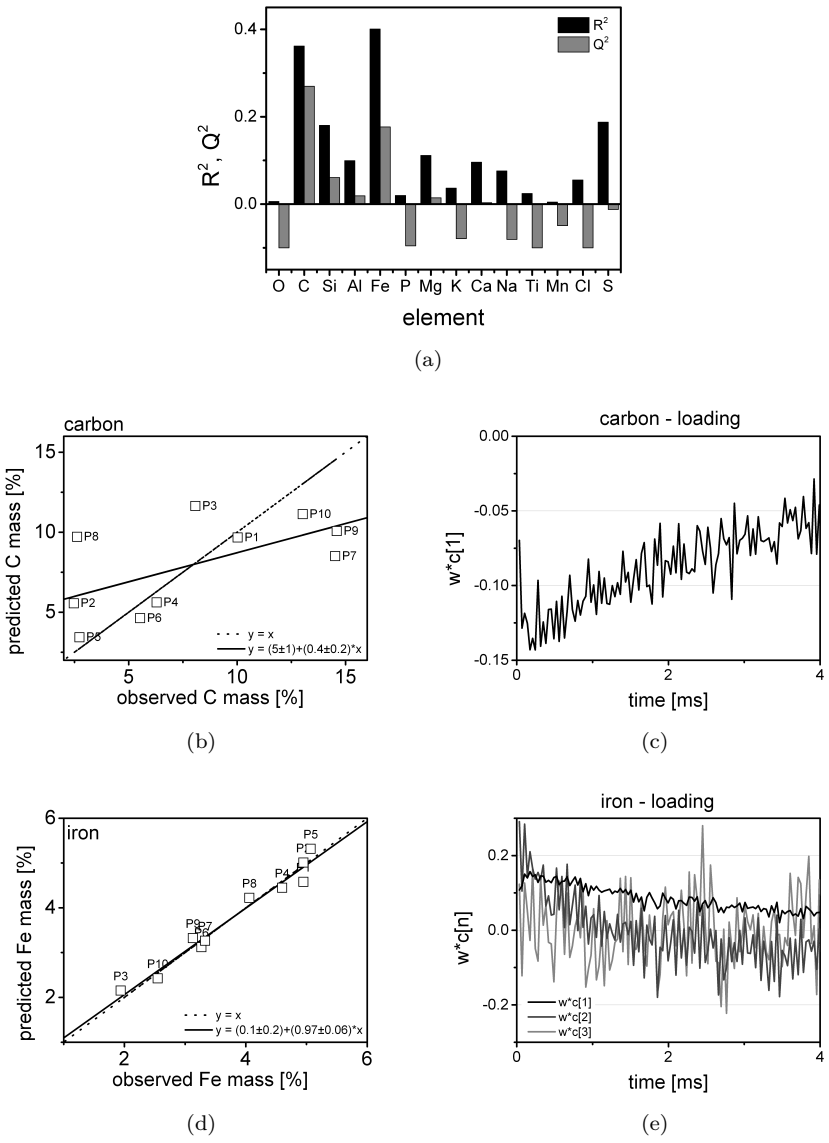

FIGURE 4.21: PLS models for the pottery relaxation data and elemental composition. (a) R^2 and Q^2 for all elements. (b) The observed and predicted C mass. (c) The loading for the carbon PLS model. (d) The observed and predicted Fe mass. (e) The loading for the iron PLS model.

4.2.3 Damaged parchment

Maps of the 2D-inverse Laplace transform of the parchment data, acquired with the RRCOSY sequence, encoded by the sequences SR-OW4 for $T_1 - T_2$ and reproduced over the 8 measurements, are presented in Fig. 4.22. Three well-defined spots can be clearly seen. The most clearly visible spot, named spot 1, has similar T_1 and different T_2 values. As spot 1, T_2 of samples with SO_2 treatment, is longer than the H_2O attacked sample and also longer than the raw matrix, the untreated parchment, these T_2 changes are related to the main interaction of water with the collagen fibers at a bound level. In

both cases it is seen that spot 1 T_1 increases within deterioration, but samples with different origins cannot be compared in absolute values due to differences assigned to the parchment origins and the chemicals used in their manufacture.

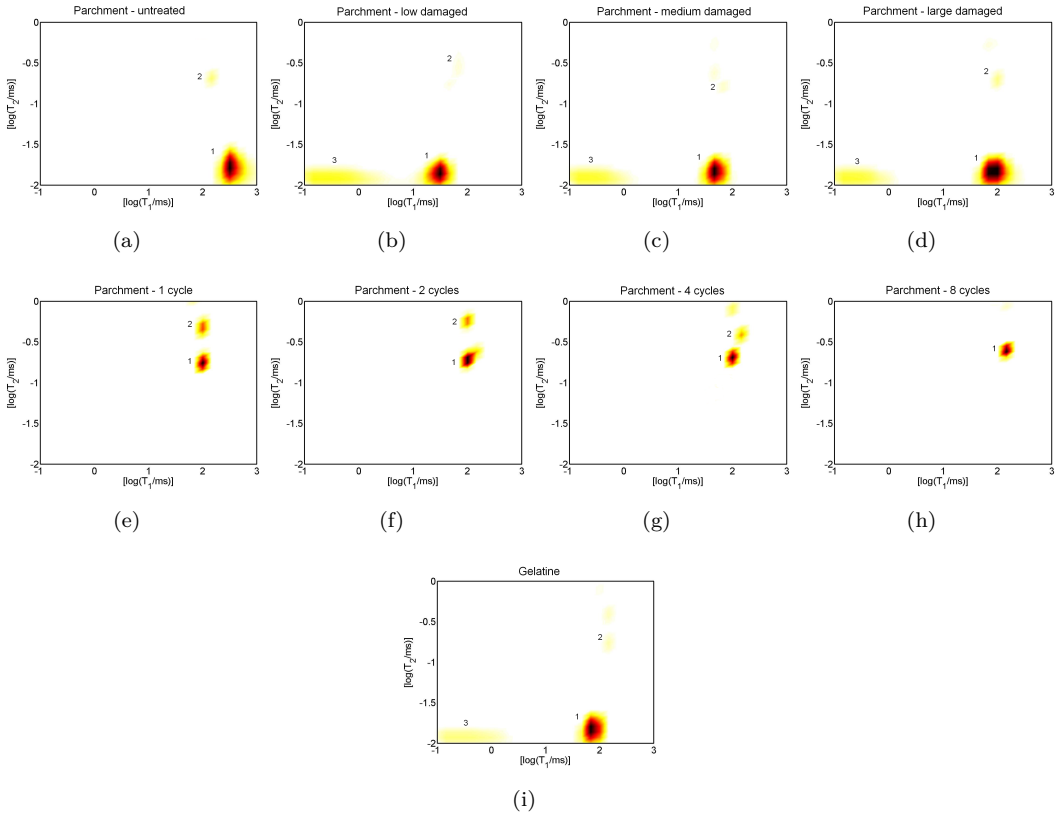

FIGURE 4.22: RRCOSY maps for the parchment samples. (a) Untreated. (b) Low level of damage from H_2O attack. (c) Medium level of damage from H_2O attack. (d) High level of damage from H_2O attack. (e) 1 cycle of SO_2 treatment. (f) 2 cycles of SO_2 treatment. (g) 4 cycles of SO_2 treatment. (h) 8 cycles of SO_2 treatment. (i) Gelatine.

The second notable spot, labeled spot 2, has longer T_2 but similar T_1 compared to spot 1. Spot 2 indicates free water molecules remaining inside the collagen structures, with more mobility. Spot 2 magnetization is high for the SO_2 and low for the H_2O attacked samples, so the non-chemically treated sample has less free water in its structure because the chemical treatments took place in an aqueous solution. Spot 2's tendency is to disappear with progressive aging, as it is not more noticeable in the samples with 8 cycles of aging than it is with 2 cycles. This confirms that the affinity between water and collagen increases along the degradation.

The last spot, spot 3, is observed only in the 2D relaxation map of the H_2O attacked parchment and the gelatine sample. As it is not also present in the chart of the untreated sample, it is reasonable to correlate this spot with the interaction of water with gelatinized collagen in the more-than-300-year-old parchment. The SO_2 attack probably caused more degradation by hydrolysis than by gelatinization.

One-dimensional relaxation experiments were carried out extracting selected lines of the RRCOCY experiment: the first echo acquisition of the T_2 encoding results in a 1D T_1 experiment; the last acquisition in the T_1 encoding results in a 1D T_2 experiment. Figure 4.23(a) shows the T_1 encoding given by the saturation-recovery experiment of the SO_2 attacked parchment; Fig. 4.23(b) shows a similar time encoding, but each point of the curve is averaged over the first four echoes of the T_2 encoding. Fig. 4.23(c) shows the T_2 encoding given by the OW4 experiment. It can be clearly seen that averaging echoes in a T_1 experiment elongates the relaxation time. Also, there are notable differences in the decay amplitude during aging.

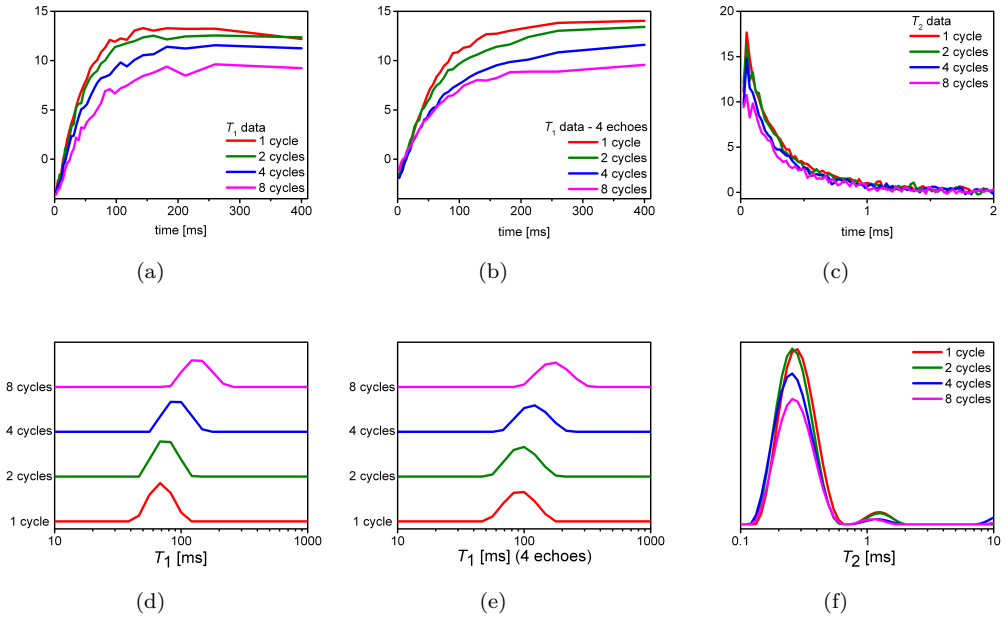

FIGURE 4.23: Parchment 1D data of the SO_2 attacked samples. (a) T_1 data by saturation-recovery. (b) T_1 data by saturation-recovery, averaging 4 echoes. (c) T_2 data by OW4. (d) ILT of Fig. (a). (e) ILT of Fig. (b). (f) ILT of Fig. (c).

The decay curves presented in Figs. (a), (b) and (c) were submitted to a 1D-inverse Laplace transform algorithm with proper kernels for the respective relaxation times. The results are presented in Figs. 4.23 4.23(d), 4.23(e) and 4.23(f) for the T_1, T_1 (average of 4 echoes) and T_2 data, respectively. Both of the T_1 graphs indicate one relaxation peak that shifts to longer times during aging, although the effect of averaging echoes introduces T_2 weighting, which elongates the T_1 values of the peak. For T_2, two relaxation peaks were present, attributed to collagen-water interaction at a freer (the long) and more restricted (the short component) level. Aging breaks the collagen chains, which allows water loss and may decrease magnetization; this results in a very small, almost undetectable shift in the distribution center. Similarly, the long component also shrinks during aging.

The 1D analysis leads to conclusions similar to those from the 2D analysis, but

with poorer details; for example, spot 3 is not recognized in 1D experiments. On the other hand, performing 2D maps is more time-consuming than a T_2 experiment, but is about the same in terms of time investment as a T_1 experiment, with the difference being that RRCOSY requires acquisition of a full CPMG train after a T_1 measurement. The second disadvantage of bi-dimensional analysis is that in the data process multi-dimensional relaxation experiments require more complex inversion algorithms.

The first regression method for the 1D data was a non-linear curve fitting with mono-expoential functions for the T_1 and bi-exeponential for the T_2 data. The fitted amplitudes and relaxation times are presented in Fig. 4.24, that figure confirms that the magnetization amplitude is reduced during both of the aging processes. There are two feasible explanations:

1. Supposing that the ^{1}H amount inside the sensitive volume did not change between the samples, this change is attributed to the dead time of the experiment.
2. Water loss during the aging process.

As the T_2 magnetizations of the long component change much less than the differences in total magnetization given by the T_1 amplitude, explanation 2 is discarded. Explanation 1 is also supported by the fact that the high range of the magnetization belongs to the T_2 short component. The gelatine sample shows anomalous magnetization because it did not have the same origin as the others; i.e., it is not parchment, so it has an elevated number of hydrogen atoms.

Comparing Fig. 4.24(a) and Fig. 4.24(c), a small difference in magnetization can be seen when the T_1 curves are averaged in echoes, as expected; comparing Fig. 4.24(b) and Fig. 4.24(d) highlights the elongation of T_1 upon echo averaging. Moreover, both Fig. 4.24(b) and Fig. 4.24(d) suggest that T_1 increases during the SO_2 degradation or the damages after the H_2O attack, trending to the T_1 of the gelatine sample.

Furthermore, the T_2 data in Fig. 4.24(e) reveal decay of the magnetization of the long component during the SO_2 attack; for the H_2O attacked samples, the increment in absolute value can be confused with the error bars, so no information could be extracted. A similar phenomenon is present in the results shown in Fig. 4.24(f): the big error bars do not allow for an exact conclusion. Regarding Fig. 4.24(h), the short T_2 time seems to slightly decrease during aging; as their values are about 250 µs, the magnetizations in 4.24(g) are weighted by the dead time.

As an alternative methodology, 1D-ILT were carried out in the decay data and posteriorly adjusted to a normal distribution by non-linear regression, with one (T_1 experiments) or two centers (T_2 experiments). The distribution area is proportional to

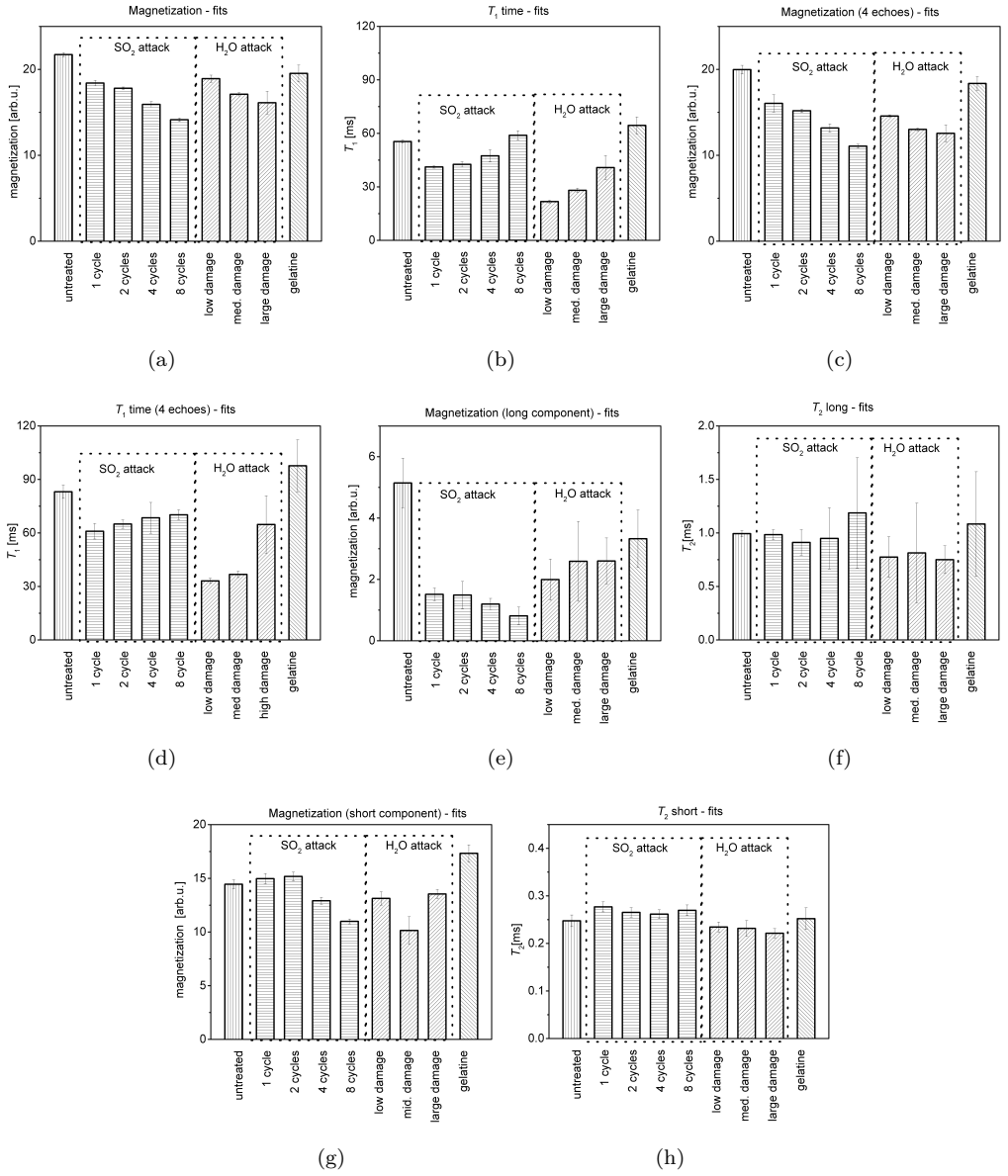

FIGURE 4.24: Mono-exponential curve-fits of the T_1 curves. (a) Magnetization. (b) T_1. (c) Magnetization (adding 4 echoes). (d) T_1 (adding 4 echoes). Bi-exponential curve-fits of the T_2 curves. (e) Magnetization of the long component. (f) T_2 of the long component. (g) Magnetization of the short component. (h) T_2 of the short component.

the magnetization amplitude; its center is the correlated relaxation time, as is shown in Fig. 4.25. The results are presented in Fig. 4.25; however, this approach leads to conclusions similar to those from Fig. 4.24. There is a small difference between the accuracy of exponential regression and the ILT process, which comes from the additional mathematical process behind the ILT algorithms.

The results for the SO_2 attacked samples presented in Fig. 4.25 were explored through a linear regression between the aging cycles and magnetizations on one hand and the relaxation times on the other. These results are shown in Fig. 4.26, with the

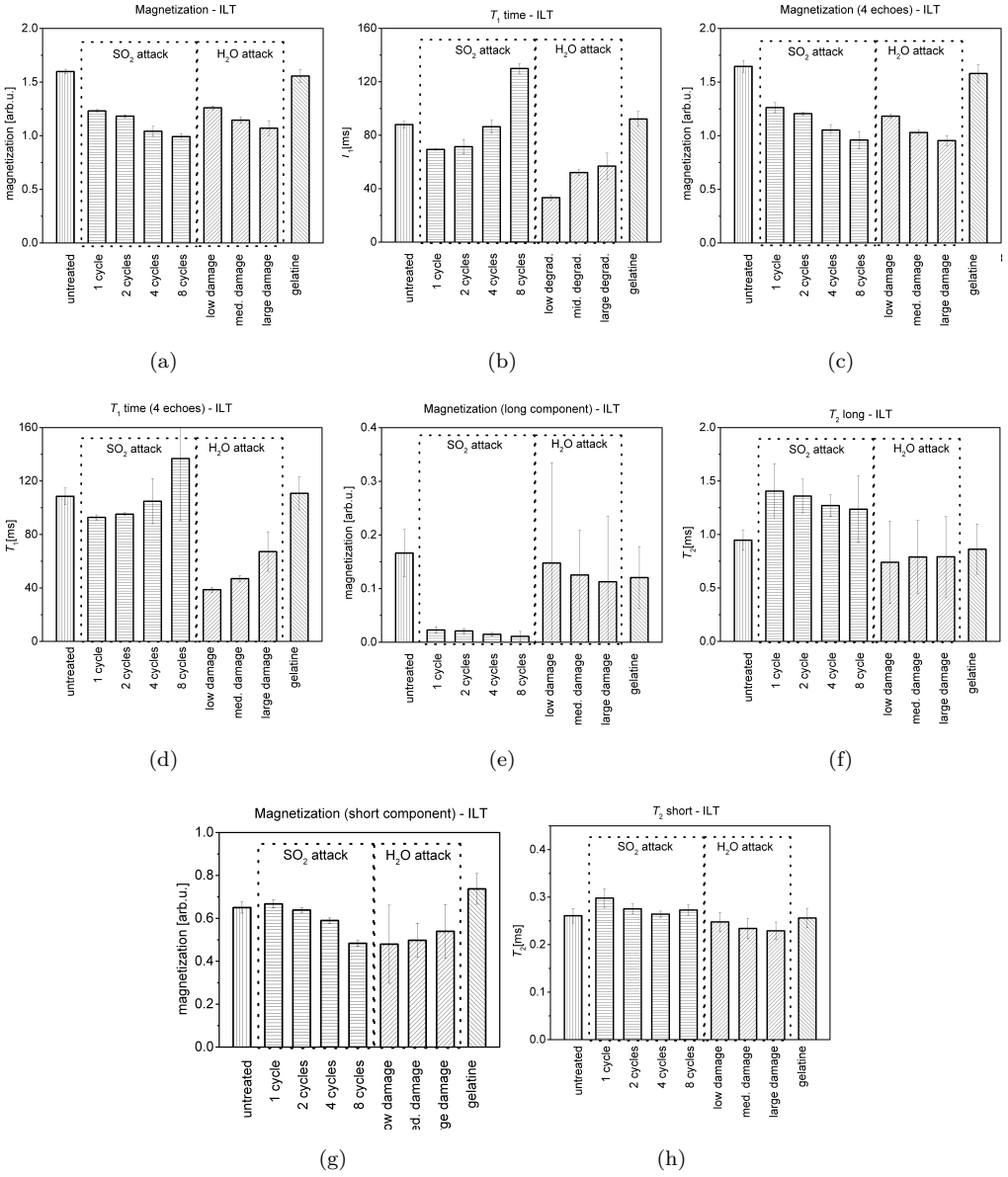

FIGURE 4.25: Inverse Laplace transform coefficients. (a) T_1 magnetization. (b) T_1 relaxation time. (c) T_1 (adding 4 echoes) magnetization. (d) T_1 (adding 4 echoes) relaxation time. (e) T_2 magnetization of the long component. (f) T_2 relaxation time of the long component. (g) T_2 magnetization of the short component. (h) T_2 relaxation time of the short component.

respective linear, angular and correlation coefficients summarized in Tab. 4.14.

From Figs. 4.26(a) and 4.26(c) it is observed that both magnetizations result in good correlation with the cycles of SO_2 attack and with the T_1 acquired with only one echo. Averaging four echoes introduces relaxation weight and reduces the correlation, as the T_2 values do not present satisfactory correlation.

The percentages of the long and short components' magnetization extracted from

TABLE 4.14: Coefficients of the linear curve fits of the ILT treatment (Fig. 4.26).

Variable	Linear coef.	Angular coef.	$\bar{R}^2$
magnetization	1.24 ± 0.02 arb.u.	-0.80 ± 0.01 arb.u./(n. cycles)	0.926
T_1 relax. time	61 ± 1 ms	8.4 ± 0.7 ms /(n. cycles)	0.978
magnetization (4 echoes)	1.31 ± 0.03 arb.u.	-0.11 ± 0.03 arb.u./(n. cycles)	0.850
T_1 (4 echoes) relax. time	90 ± 2 ms	2.9 ± 0.9 ms /(n. cycles)	0.772
magnetization T_2 long comp.	0.024 ± 0.002 arb.u.	-0.0020 ± 0.0004 arb.u./(n. cycles)	0.819
T_2 long comp. relax. time	1.4 ± 0.4 ms	-0.03 ± 0.01 ms /(n. cycles)	0.670
magnetization T_2 short comp.	0.70 ± 0.03 arb.u.	-0.06 ± 0.01 arb.u./(n. cycles)	0.868
T_2 short comp. relax. time	0.27 ± 0.01 ms	-0.01 ± 0.03 ms /(n. cycles)	0.388

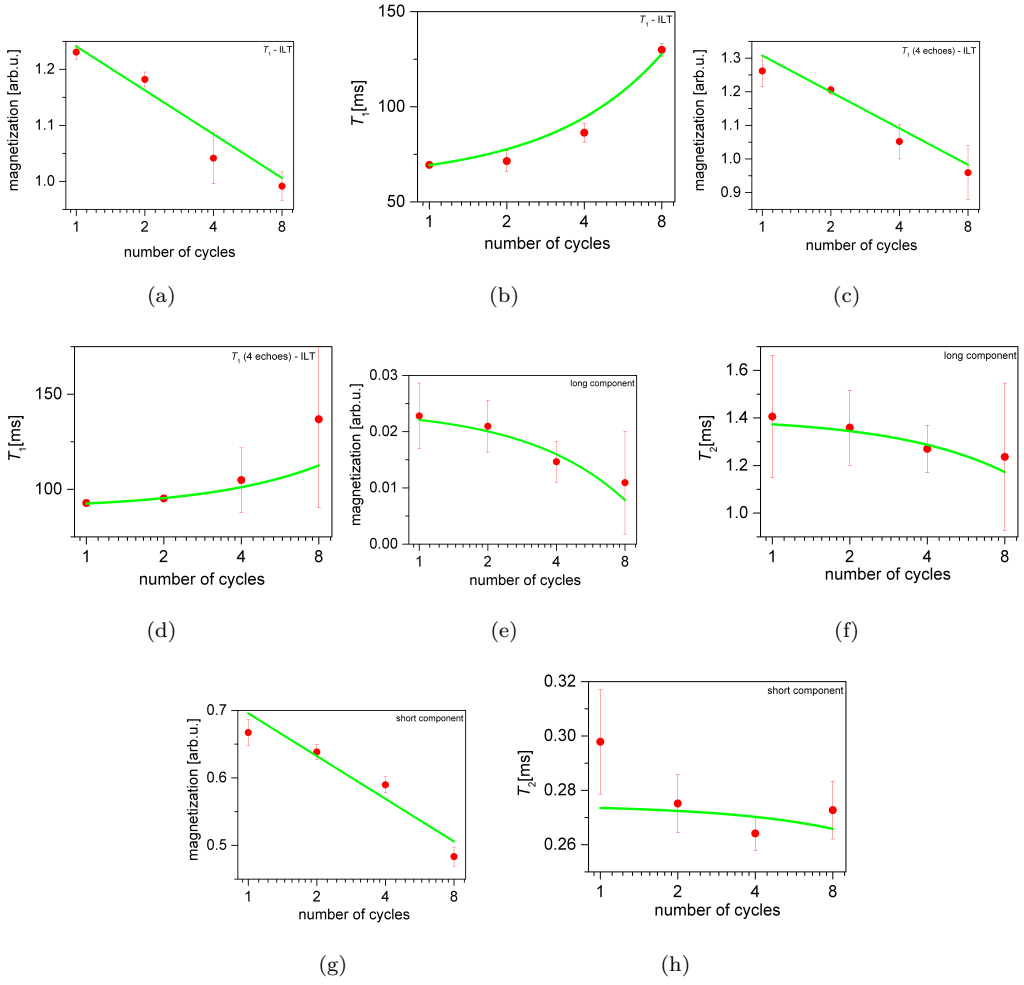

FIGURE 4.26: Fitting parameters correlated with the number of aging cycles. (a) Magnetization. (b) T_1 relaxation times. (c) Magnetization (average four echoes). (d) T_1 (average four echoes) relaxation times. (e) Magnetization of the long component. (f) T_2 relaxation times of the long component. (g) Magnetization of the short component. (h) T_2 relaxation times of the short component.

both T_2 data processes are shown in Fig. 4.27. It can be seen that the collagen interactions with water at a bound level represent between 70 and 90% of the NMR signal.

As a third methodology, multi-variate data analysis was carried out with the 1D

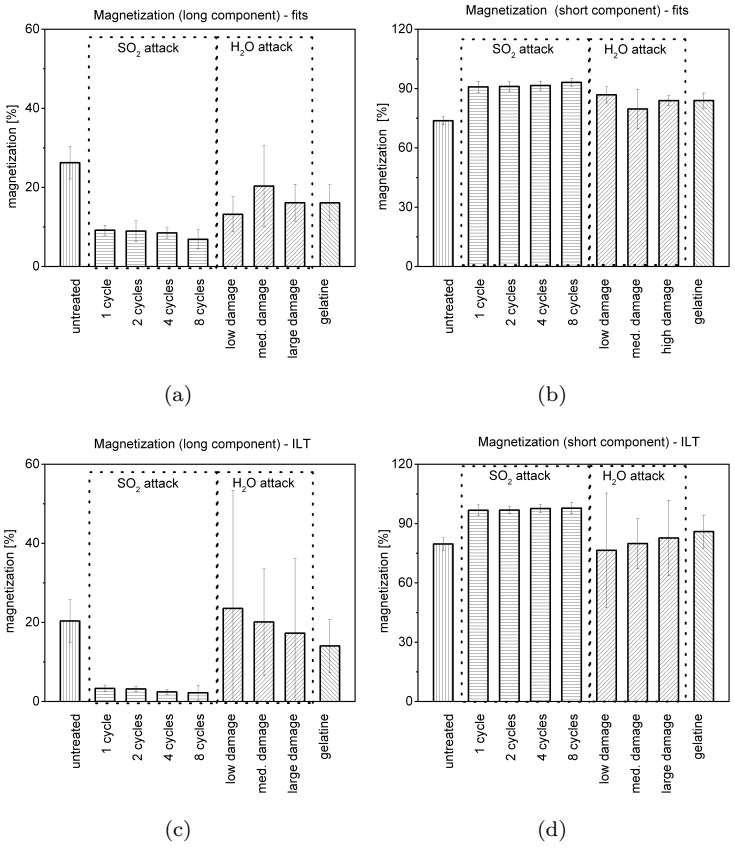

FIGURE 4.27: Percentage values of the T_2 magnetizations. (a) Long component (bi-exponential curve fit). (b) Short component (bi-exponential curve fit). (c) Long component (inverse Laplace transform). (d) Short component (inverse Laplace transform).

relaxation data. The chemometric matrix lines consisted of the number of experiments N and the encoding times over the columns, which resulted in a matrix with dimensions N (samples) × i (encoding times). The matrix was centered on the average and set as dependent variables in a PLS model; the independent variables were attributed to the number of aging cycles or the aging condition for each different discriminant class (PLS-DA). Separate PLS models were carried out for the different SO_2 and H_2O attacked samples, with the T_1, T_1 averaged in 4 echoes and T_2 curves. A pre-processing by normalization by the maximum would eliminate any amplitude discrimination, so the models were repeated for the normalized data.

The resulting scores are presented in Fig. 4.28, the loadings in Fig. 4.29 and the respective fitting coefficients are summarized in Table 4.15. The SO_2 attack is very well explained, with only one latent variable (LV1) in the T_1 normalized and non-normalized models, and has the maximum loading at about 60 ms, as indicated in Figs. 4.29(a) and 4.29(b). These figures agree with the T_1 average of Fig. 4.24(b); in this case magnetization amplitudes are not important. The H_2O attack requires an additional LV to explain its remaining 50% of variation. LV1 has maximum changes at about

40 ms, again in agreement with Fig. 4.24(b). LV2 has maximum variation at a time shorter than 10 ms and results in grouping in Figs. 4.28(g) and 4.28(h) with regard to the gelatinized state of the sample. Similar conclusions are achieved for the models with 4 echoes averaged; however, these last have lower coefficients. Although very noisy, the T_2 data resulted in a very good model for the SO_2 attacked samples, but not for the H_2O attacked ones. T_2 loading changes during the SO_2 treatment, as shown in Fig. 4.29(e), are similar to a mono-exponential decay with a rate constant of 300 µs. As this is similar to the changes present in the loadings of Fig. 4.29(e), it is concluded that the chemical treatment led to changes in the time and magnetization amplitudes of the decay; for the H_2O attacked parchment, there was a small change in magnetization, because the loading plot of LV1 Fig. 4.29(k) has a decay constant of 300 µs, but no model was possible with the normalized data. The T_2 models, the last component of all, are mainly noise.

TABLE 4.15: Coefficients of the PLS models for parchment

rel. time	norm.	attack	model	LV1		LV2		LV3		LV4		LV5	
				R^2	Q^2	R^2	Q^2	R^2	Q^2	R^2	Q^2	R^2	Q^2
T_1	no	SO_2	PLS	0.963	0.960	0.978	0.960						
T_1	yes	SO_2	PLS	0.899	0.892	0.932	0.892						
T_1	no	H_2O	PLS-DA	0.390	0.368	0.875	0.860	0.953	0.930				
T_1	yes	H_2O	PLS-DA	0.446	0.433	0.914	0.906	0.960	0.924				
T_1 (4 ec.)	no	SO_2	PLS	0.902	0.900	0.933	0.920						
T_1 (4 ec.)	yes	SO_2	PLS	0.115	0.095	0.652	0.513	0.807	0.578				
T_1 (4 ec.)	no	H_2O	PLS-DA	0.410	0.383	0.860	0.828	0.948	0.894	0.969	0.904	0.980	0.924
T_1 (4 ec.)	yes	H_2O	PLS-DA	0.443	0.426	0.843	0.810	0.931	0.893	0.967	0.915		
T_2	no	SO_2	PLS	0.932	0.926	0.980	0.934	0.994	0.942				
T_2	yes	SO_2	PLS	0.492	0.260	0.534	0.299	0.799	0.585				
T_2	no	H_2O	PLS-DA	0.424	0.401	0.875	0.350						
T_2	yes	H_2O	PLS-DA	0	0								

The T_1, T_2 correlation experiment indicated three different T_1, T_2 relaxation peaks, attributed to collagen interactions with free and bound water as well as to water and gelatinezed collagen interactions. It proved to be a complete method and provided more information than the one-dimensional analysis, but it is very time-consuming and requires advanced and difficult mathematical algorithms. All three methodologies of performed one-dimensional analysis indicate T_1 as the best parameter to track parchment aging. Data fitting provided better accuracy than the ILT, and also has another positive characteristic: it quantifies the magnetization amplitude and relaxation time. The PLS models were very powerful because they indicated water interactions with the non-gelatinized and gelatinized collagen. This makes the PLS a very good tool for classifying the damage state of parchment. Chemical and biological aging agreed with the trend of the relaxation times; however, the artificial process of aging may have changed the water

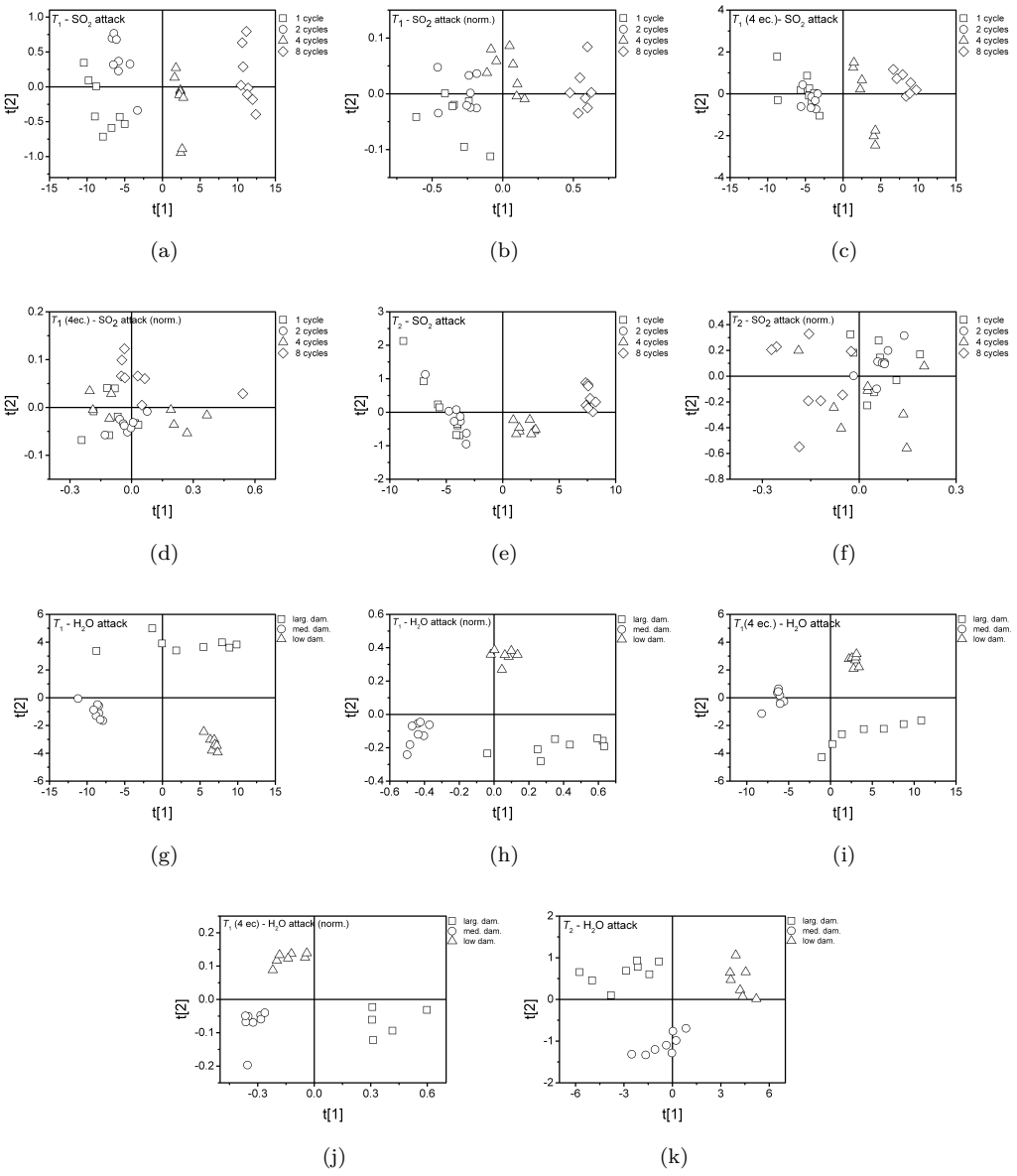

FIGURE 4.28: Scores of the PLS model for the relaxation curves. (a) SO_2 attacked samples T_1 acquired data. (b) SO_2 attacked samples T_1 normalized data. (c) SO_2 attacked samples T_1 (adding 4 echoes) acquired data. (d) SO_2 attacked samples T_1 (adding 4 echoes) normalized data. (e) SO_2 attacked samples T_2 acquired data. (f) SO_2 attacked samples T_2 normalized data. (g) H_2O attacked samples T_1 acquired data. (h) H_2O attacked samples T_1 normalized data. (i) H_2O attacked samples T_1 (adding 4 echoes) acquired data. (j) H_2O attacked samples T_1 (adding 4 echoes) normalized data. (k) H_2O attacked samples T_2 acquired data.

characteristics in the parchment sample. Averaging over echoes increases the signal-to-noise ratio but brings undesired T_2 contamination, more pronounced in fast relaxation decays, such as those of parchment. T_2 did not show good correlation with aging.

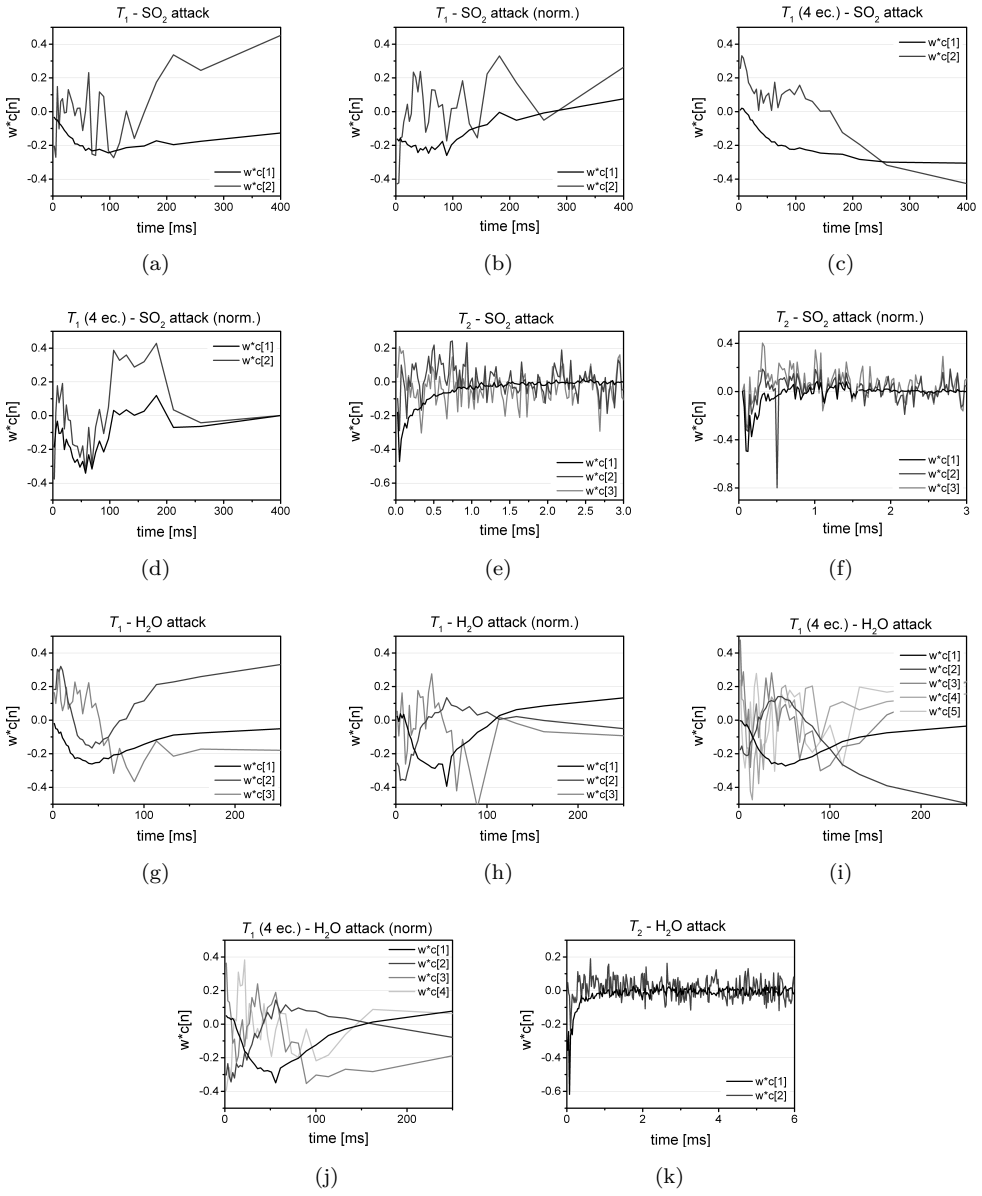

FIGURE 4.29: Loadings of the PLS model for the relaxation curves. (a) SO_2 attacked samples T_1 acquired data. (b) SO_2 attacked samples T_1 normalized data. (c) SO_2 attacked samples T_1 (adding 4 echoes) acquired data. (d) SO_2 attacked samples T_1 (adding 4 echoes) normalized data. (e) SO_2 attacked samples T_2 acquired data. (f) SO_2 attacked samples T_2 normalized data. (h) H_2O attacked samples T_1 acquired data. (g) H_2O attacked samples T_1 normalized data. (j) H_2O attacked samples T_1 (adding 4 echoes) acquired data. (i) H_2O attacked samples T_1 (adding 4 echoes) normalized data. (k) H_2O attacked samples T_2 acquired data.

4.2.4 Handmade paper

Examples of relaxation data acquired with the OW4 pulse sequence for hemp, rice and bamboo papers, with their respective inverse Laplace transforms, are presented in Fig. 4.30. It can clearly be seen that the decay is not mono-exponential and the larger changes in the bamboo paper decays suggests this paper as the most vulnerable to

the aging process. In agreement with ref. [18], the decays should have bi-exponential behavior of the magnetization; however, this is difficult to observe through ILT, the relaxation time constants merged to a single value in the distribution.

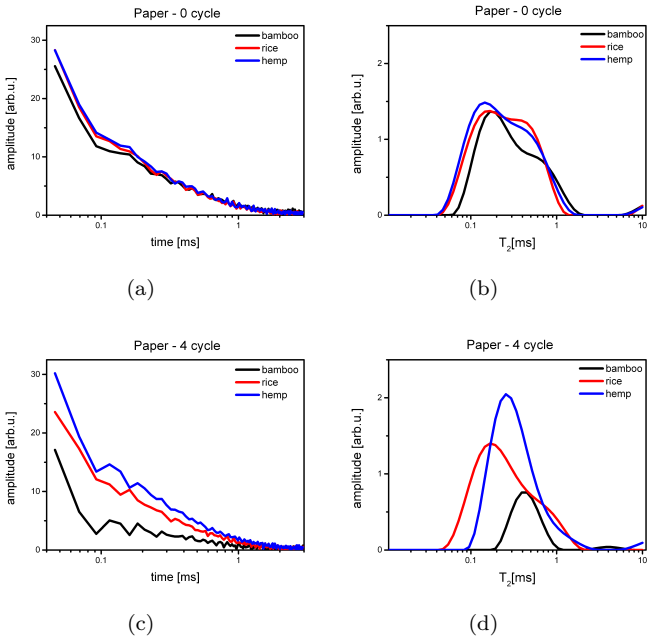

FIGURE 4.30: (a) OW4 magnetization decays for untreated hemp, rice and bamboo paper. (b) ILT of Fig. 4.30(a). (c) OW4 magnetization decays for hemp, rice and bamboo paper with 4 cycles of aging. (d) ILT of Fig. 4.30(c).

Therefore, the bi-exponential curve fit model was chosen, and all the decay curves were explored. The magnetizations for the long and short components in absolute value and in percentage, and the respective relaxation times, are presented in Fig. 4.31.

Because of the very low amplitude of the magnetization decays, it is difficult to be exact in the extracted fit parameters. This complication does not exist if the intention is to compare the three kinds of paper: bamboo paper always has a smaller magnetization amplitudes and changes over aging than the others. The difference between the rice and hemp papers is small, but the hemp paper has a little more magnetization amplitude than the rice. The relaxation times are similar, mainly due to the high error bars. The ratio proposed by Capitani et al. [110], given by the magnetization of the long component, attributed to water, divided by that of the short component, related to cellulose, was also calculated, and is presented in Fig. 4.32. The propagation of errors resulted in huge error bars; together with the high dead time contamination of the short component magnetization, this resulted in a ratio that is much smaller and does not agree with the findings of reference [110].

The trend of the changes in the relaxation constants can be better visualized using multi-variate methodology. PLS models were created from an x-matrix with the samples

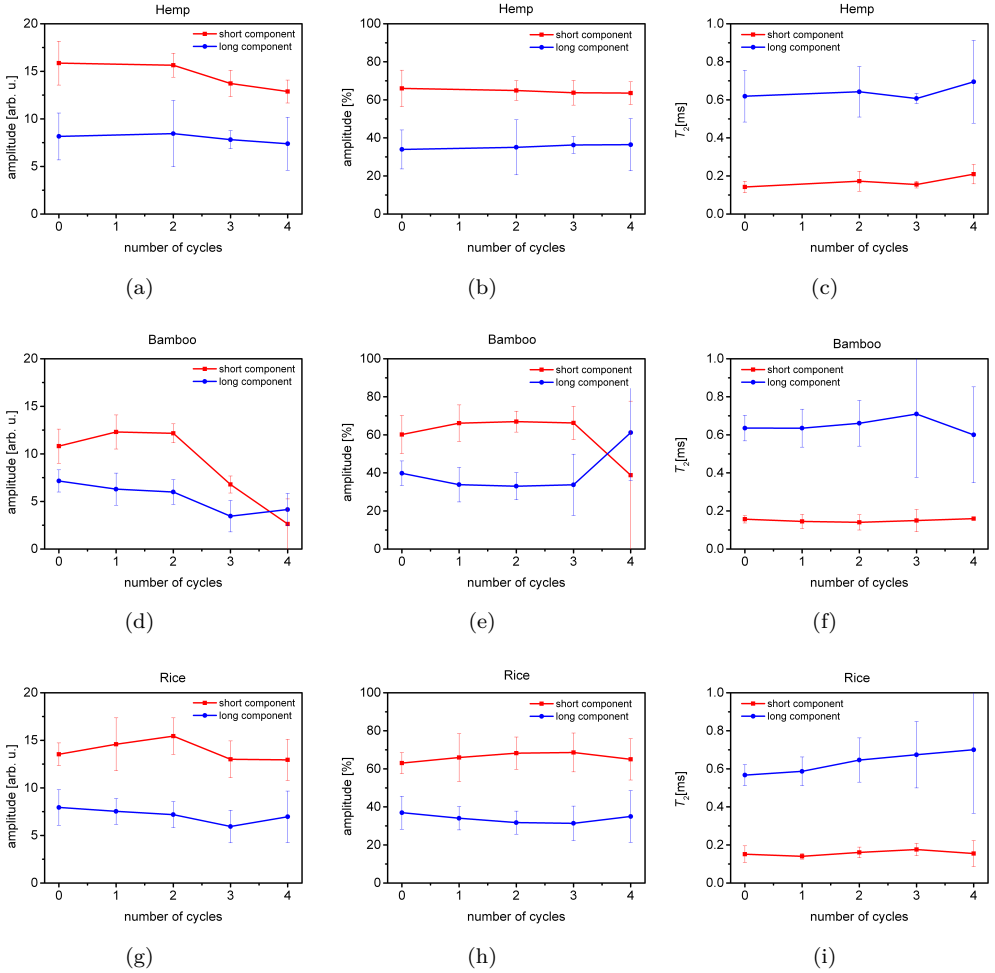

FIGURE 4.31: OW4 results. (a) Hemp paper magnetization. (b) Hemp paper relative magnetization. (c) Hemp paper T_2. (d) Bamboo paper magnetization. (e) Bamboo paper relative magnetization. (f) Bamboo paper T_2. (g) Rice paper magnetization. (h) Rice paper relative magnetization. (i) Rice paper T_2.

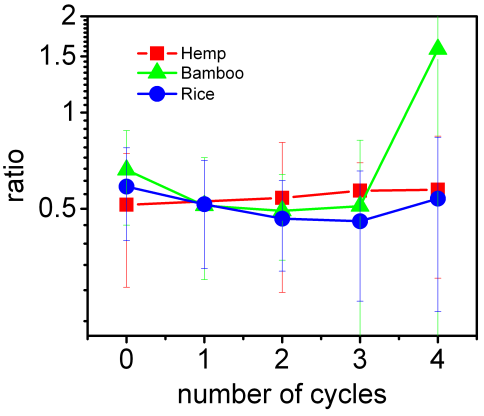

FIGURE 4.32: Ratio suggested in reference [110] of the magnetization for the different kinds of paper over the aging process.

over the lines and the magnetization of each echo time over the columns; the y-array was the number of aging cycles. Fig. 4.33 shows the PLS scores for the non-normalized and normalized (by the initial value) data, always centered on the average; Fig. 4.34 shows the respective loadings.

TABLE 4.16: Coefficients of the PLS model for paper

type	norm.	model	LV1		LV2		LV3		LV4		LV5	
			R^2	Q^2	R^2	Q^2	R^2	Q^2	R^2	Q^2	R^2	Q^2
hemp	no	PLS	0	0								
hemp	yes	PLS	0	0	0	0						
bamboo	no	PLS	0.898	0.895	0.964	0.944	0.998	0.980				
bamboo	yes	PLS	0.716	0.685	0.966	0.918	0.998	0.956				
rice	no	PLS	0.618	0.426	0.882	0.636	0.989	0.768				
rice	yes	PLS	0	0								
all untreated	no	PLS-DA	0.476	0.374	0.861	0.471	0.969	0.577	0.988	0.713	0.999	0.841
all untreated	yes	PLS-DA	0.444	0.242	0.806	0.166						
all 4 cycles	no	PLS-DA	0.497	0.452	0.918	0.860	0.994	0.889				
all 4 cycles	yes	PLS-DA	0.488	0.447	0.872	0.754	0.967	0.810	0.987	0.825		

The model coefficients are very good for the bamboo and rice papers, without normalization. As no model could be fitted to the hemp paper, it can be concluded that the hemp paper did not degrade during the attempted aging process, and can be deemed the highest quality paper.

The rice paper showed little decrease in magnetization during aging, as can be seen in Fig. 4.34(c); no model could be fitted for the normalized sample, the selected aging process did not change T_2. The bamboo paper proved to be very sensitive to aging by heating, with very defined changes in magnetization amplitude, as shown in Fig. 4.34(a), also T_2 changes with maximum variance at a time of about 100 µs, as observed in Fig. 4.34(b). Furthermore, good PLS models were fitted for the various untreated samples. The first latent variable of Fig. 4.33(d) suggests that the bamboo paper has the smallest magnetization amplitude, in agreement with Fig. 4.31.

The time decay also changes among the three kinds of paper, as presented in Fig. 4.33(e); the bamboo paper has the shortest component (low LV1 and LV2) and the hemp has the longest component (high LV1 and LV2). The aging process brings loading similar to the untreated samples, as indicated in Fig. 4.34(f); the scores of Fig. 4.33(f) affirm that the aging process increased the differences in paper relaxation times, resulting in clearer distinctions among the groups.

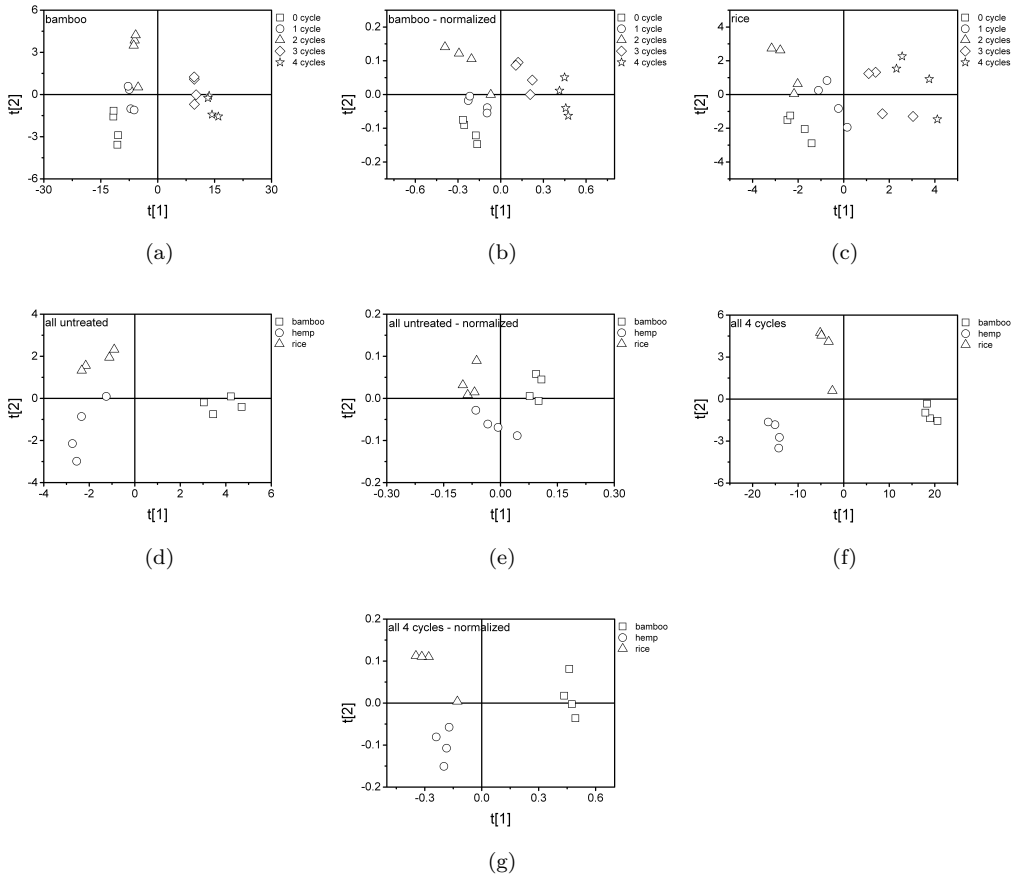

FIGURE 4.33: Scores of the PLS model for the T_2 relaxation curves. (a) Bamboo paper acquired data. (b) Bamboo paper normalized data. (c) Rice paper acquired data. (d) All untreated papers acquired data. (e) All untreated papers normalized data. (f) All 4 cycles aged paper acquired data. (g) All 4 cycles aged paper normalized data.

4.2.5 Canvas linings

Differences in T_1 were realized by analyzing the profile amplitudes weighted by the recycle delay, where long T_1 values bring more variation than short ones. A full profile performed with 1024 scans took about 70, 100 and 190 minutes with recycle delays of 200 ms, 300 and 500 ms, respectively.

Profiles encoded as the mean of the first four echoes averaged until 50% of the initial amplitude, even though this value changed with different samples due to changes in the amplitude and relaxation rate. The profiles are shown in Fig. 4.35, where it can clearly be seen that the variation in Fig. 4.35(a) suggests canvas A, with the longest T_1, well estimated at 200 ms. Similarly, the deep layer of canvas B in Fig. 4.35(b) has a long T_1, also about 100 ms. Furthermore, samples C, D, E and F have low amplitudes, which is attributed to the low mobility of the ^{1}H spins in the material, because their material is harder than the material found in samples A and B. Also, it can be seen that

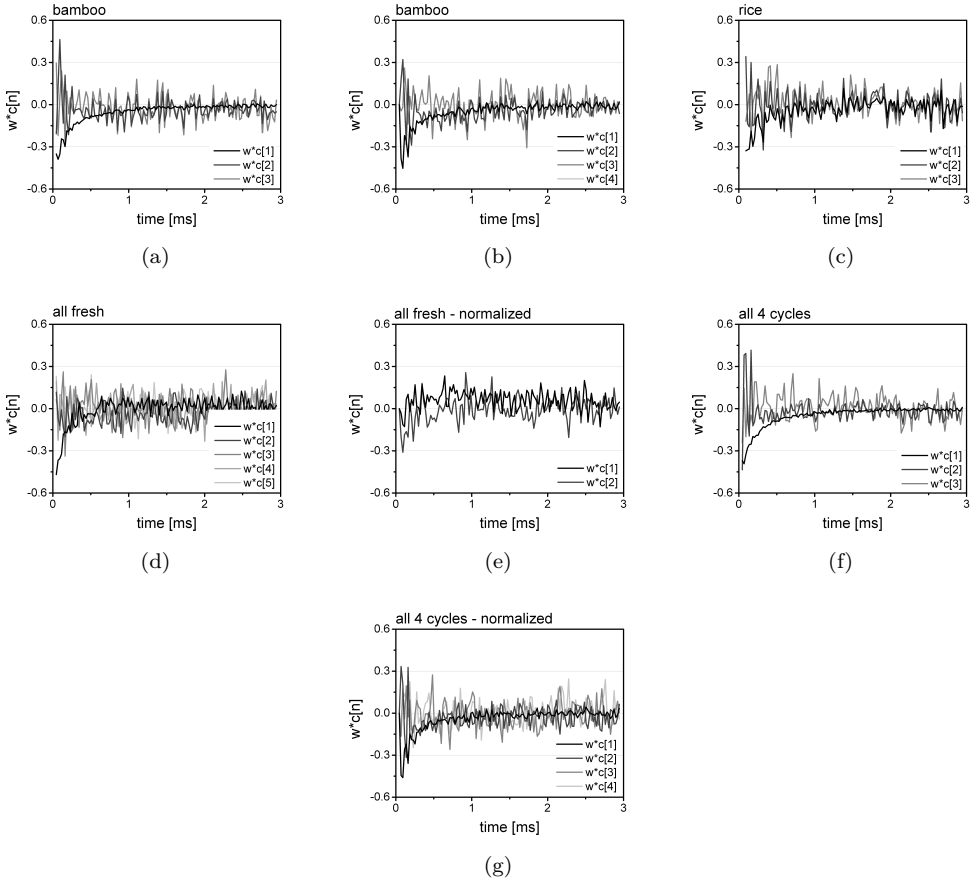

FIGURE 4.34: Loadings of the PLS model for the T_2 relaxation curves. (a) Bamboo paper acquired data. (b) Bamboo paper normalized data. (c) Rice paper acquired data. (d) All untreated papers acquired data. (e) All untreated papers normalized data. (f) All 4 cycles aged paper acquired data. (g) All 4 cycles aged paper normalized data.

the material in sample A is diffused in two layers as the minimum amplitude found at depth (0.7 mm) discerns a layer of material change; in sample B the wax is concentrated in the center and no layer is identified.

Figure 4.36 shows the results of averaging the first 64 echoes, ensuring co-addition until the noise level. The result is proportional to the average T_2, so this plot confirms that samples A and B have softer material than samples C, D, E and F. The spatial distribution of this soft material is also confirmed. Very high values, for example between 0 and 0.4 mm and 1.3 and 1.5 mm of canvas A (Fig.4.36(a)), come from the required normalization where the initial amplitude is very small (see Fig 4.35(a)).

The weighting functions calculated for the limits $i_{\mathtt{i}} = 1$, $i_{\mathtt{f}} = 4$, $j_{\mathtt{i=5}}$, $j_{\mathtt{f}} = 32$ are exhibited in Fig. 4.37. As was demonstrated, the mathematics behind the weighting function eliminate amplitude weighting in the profiles, so Figs. 4.37(a) and 4.37(b) prove that the wax in samples A and B is made from a soft and homogenous material, although Figs. 4.35 and 4.36 confirm that the wax is differently distributed spatially. The hard

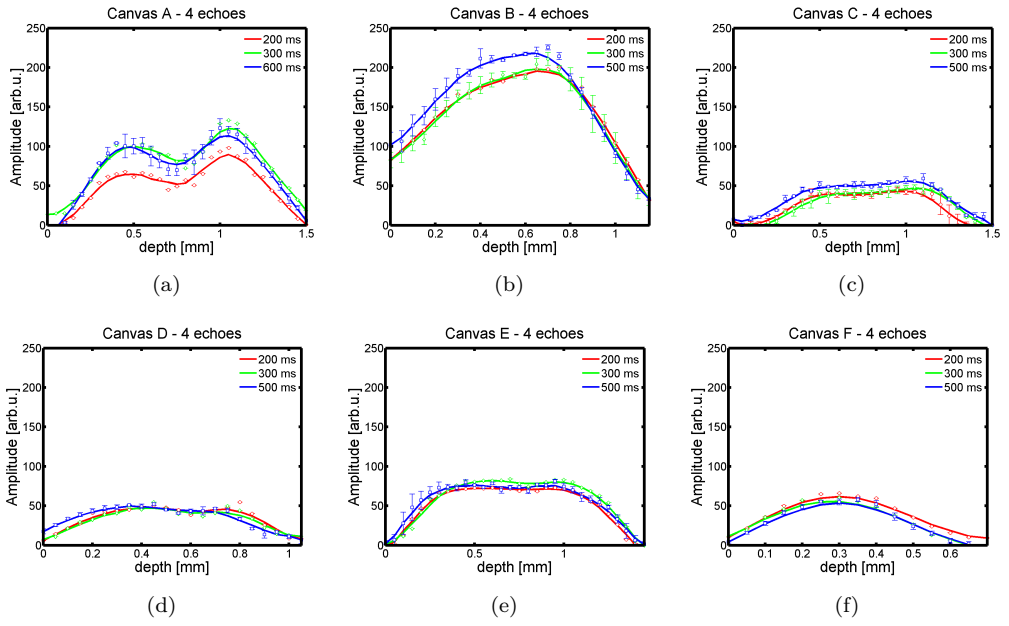

FIGURE 4.35: Sum of four echoes for the canvas samples in three different recycle delays. (a) Sample A. (b) Sample B. (c) Sample C. (d) Sample D. (e) Sample E. (f) Sample F.

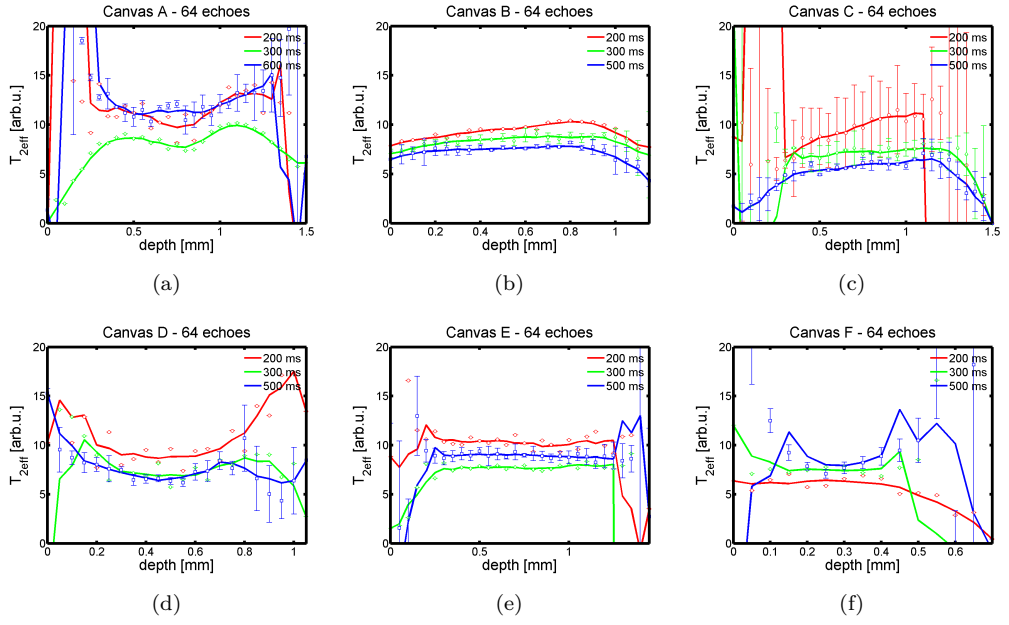

FIGURE 4.36: Sum of 64 echoes for the canvas samples in three different recycle delays. (a) Sample A. (b) Sample B. (c) Sample C. (d) Sample D. (e) Sample E. (f) Sample F.

material in the samples C, D, E and F makes the low weighting function denominator very low and highly sensitive to noise, which increases the ratio value and brings noise.

Different canvas structures could be profiled with the NMR-MOUSE. The results, presented in Figs. 4.35, 4.36 and 4.37, prove, for the first time, that relaxation measurements can reveal quantitative and qualitative information about material changes

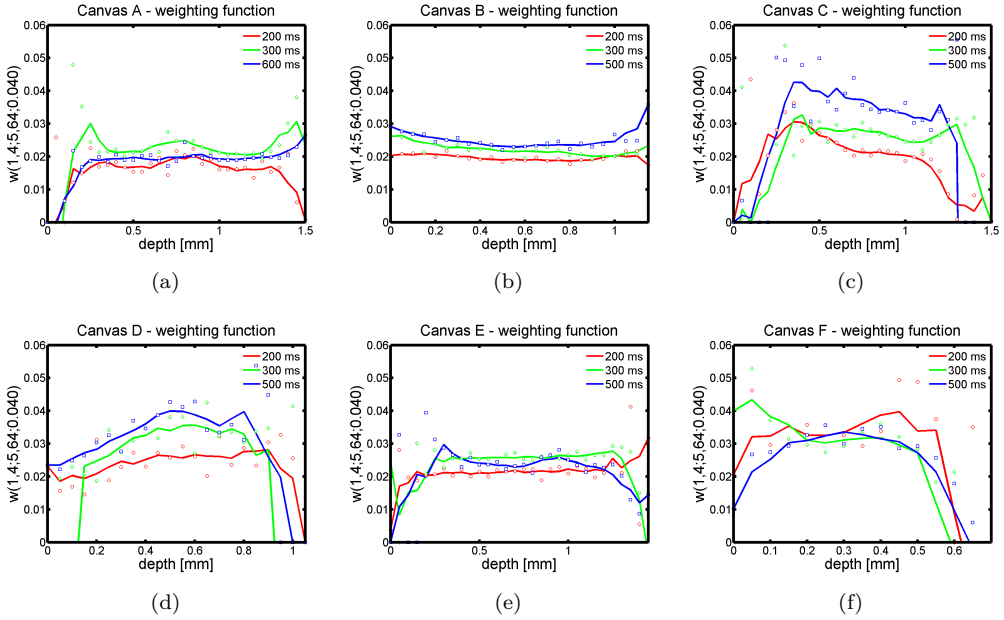

FIGURE 4.37: Weighting function (1,4;5,32) for the canvas samples in three different recycle delays. (a) Sample A. (b) Sample B. (c) Sample C. (d) Sample D. (e) Sample E. (f) Sample F.

in canvas. This experiment opens doors in the art conservation field for using unilateral NMR sensors as a powerful tool in evaluating laminated canvas and investigating suitable repairing techniques.

4.2.6 Summary

Section 4.2 has discussed innovations related to the use of single-sided NMR sensors in the cultural heritage field. Through measurements of porosity and pore-size distribution, consolidation treatments in stones could be non-invasively monitored and compared in order to choose the best consolidation method. These results suggested for the first time the possibility to perform *in situ* measurements in the Chinese Yungang Grottoes. Transverse relaxation measurements, together with multi-variate data analysis, proved to be able to predict ancient pottery's elemental composition, mainly with regard to iron (very good correlation) and carbon (satisfactory correlation). The correlation was explained by the high paramagnetic character of the iron element; the carbon in ancient pottery has many free radicals (carbon black). Due to the huge acquisition number, the bi-dimensional RRCOSY (T_1, T_2) pulse sequence applied to H_2O and SO_2 damaged parchment revealed information until now unknown in the literature: the case of a relaxation peak attributed to the gelatinized collagen-water interaction that data fit or ILT of one-dimensional pulse sequences were not able to predict. Multi-variate data analysis proved to be very powerful, because it could detect the new peak variation in

a uni-dimensional T_1 experiment faster than in a bi-dimensional one. Hemp, rice and bamboo handmade Chinese paper showed different sensitivity to aging by heating: the bamboo paper is the most sensitive, when the hemp is the least sensitive; this conclusion was possible only with multi-variate data analysis of the echoes generated by a CPMG-like pulse sequence. Moreover, for the first time, single-sided NMR is proposed as an analytical tool for monitoring reinforced canvas of artistic interest, opening doors for new optimizing canvas repair techniques.

5. Conclusion

The NMR-MOUSE proved to be an useful tool for the proposed polymer analysis. The heat fusion joining process in PE pipes indicated a rise in the polymer crystalline level, which was observed by the decrease in the sum of echoes and proven through a comparison with a DSC experiment. As the PE pipes were considered an inhomogeneous sample, the acquired data had to be explored by means of statistical averages; however, the experiment provided consistent data.

Moreover, the small differences in cross-link density of PE samples could be investigated. In this case, mono and bi-exponential regression models did not show acceptable correlation, but multi-variate data analysis revealed very small differences at the crystal domains of the polymer. The achieved PLS model fitted to the CPMG sequence had better coefficients than the OW4 one. This experiment confirmed that even in echo times on the order of 30 µs the short magnetization decays of the rigid part of a polymer can be investigated.

A slow photo-curing reaction of a dental resin sample was tracked in depths larger than 2 mm. By varying the distance between the NMR-MOUSE and the sample, the sensitive volume could be shifted across the thickness of the sample to follow the curing reaction at different depths going from light to dark curing of dental resins. A signal maximum was observed and attributed to the temperature increase caused by the exothermic reaction. Using an empirical equation the occurrence time of the temperature maximum was estimated. The experimental data were modeled with the textbook equations for first-order reaction kinetics of a photo-initiated radical polymerization. The two analyzed resins polymerize on similar time scales. The Weibull modification of the Kohlrausch function was implemented in the kinetic formula to account for the initial temperature rise of the material at the beginning of the photo polymerization time. In the proposed form the resultant semi-empirical expression fits the time dependence of the curing reaction well. The depth dependence of the reaction kinetics is in accordance with the Lambert-Beer law. The photo polymerization of the dental resins thus can be modeled as a function of reaction time and depth for the benefit of assisting the optimization of resin formulations and curing procedures.

Stones were treated with a recently developed consolidation process by re-filling $CaCO_3$ and were explored with the NMR-MOUSE in a completely non-invasive way. The results revealed hydrophobic proprieties of the consolidation process and indicated pure ethanol or isopropanol as the best solvents for Ca(OH). This work is a pioneering application of NMR to preserve Chinese cultural artifacts and will allow performance of *in situ* experiments in the Yungang Grottoes.

Multi-dimensional T_1, T_2 relaxation maps of parchments presented advances revealing chemical information not available in single relaxation curves with standard methodology, for example, a domain only depending on the gelatinized state of the collagen structures. Moreover, one-dimensional T_1 experiments can follow the damage state of parchments. Multi-variate data analysis proved to be a very powerful tool in analyzing degraded parchment, where a PLS model could reveal similar information present in the two-dimensional experiment but hidden in one-dimension T_1 decays. Also, T_2 was shown to be a fast method to acquire information about the damaged state of parchment, although T_1 explains the case better.

Three different types of Chinese handmade paper were examined with the NMR-MOUSE under the OW4 pulse sequence. The transverse magnetization decay indicated that the bamboo paper is more sensitive to aging by heating than the hemp and rice paper. The data bi-exponential fits did not help to make advanced conclusions, because the NMR signal was very weak and very short. Multi-variate data analysis again proved to be a powerful tool, and enabled the conclusion, for the first time, that hemp paper provides high quality and performance.

Furthermore, this work confirmed the possibility of discriminating different layers of lined canvas samples. The non-destructive analyses were satisfactory and raised the possibility of a future series of measurements to optimize canvas lining techniques in art restoration.

Overall, this thesis work represent a series of progress steps for the single-sided NMR sensor, mainly the NMR-MOUSE, in evaluation and ascertainment of polymers and cultural heritage artifacts. All the measurements were non-invasive and did not require sample destruction. These experiments were very innovative and open doors for many other applications, for example, in polymer production lines of chemical companies, and *in situ* analysis of cultural heritage materials.

A. Regression and multivariate data analysis

After any experimental analysis, a scientist needs to find the right model to explain the results and eliminate the experimental noise. If n samples were explored over m variables, the scientist ends up with the following X matrix data:

$$X = \left[\begin{pmatrix} X_{11} & X_{12} & X_{...} & X_{1m} \\ X_{21} & X_{22} & X_{...} & X_{2m} \\ \vdots & X_{\vdots} & X_{\ddots} & X_{\vdots} \\ X_{n1} & X_{n1} & X_{...} & X_{nm} \end{pmatrix} \right] \tag{A.1}$$

If the experiment is some NMR relaxation, variables would represent the m number of echoes, each column associated with the respective echo acquisition. There are also the p dependent variables, for example concentration or aging condition, represented by a matrix Y, with $n \times p$ elements.

Interpretation of the matrix present in Eq. A.1 is difficult, or almost impossible, thus the scientist need a model to reduce the number of variables and be able to interpret the problem. The most suspect models in NMR relaxation are exponential decays functions. However, the scientist need a good background about the information in order to come with the proper function, being mono, bi or more exponential components. So, several parameters can indicate if the regression model shows good correlation or not. Further, many times good models do not represent the real history behind the data. In this case, all the data variables can be examined separately and do not require a previous model from the user. The sub-area of chemistry which deals with multi-variate analysis is known by *Chemometrics*.

This appendix will be dedicated to explain methodology of data analysis with a proposed model, in Section A.1 and without, in Section A.2, focused on NMR relaxometry analysis.

A.1 Regression analysis

A.1.1 Theory

Once identified the model $f(x)$, data curve fitting may provide the respective function components by minimizing the sum of the squared residuals. Being y_i the measured values, the sum is represented by:

$$S = \sum_{i=1}^{m} r_i^2 = \sum_{i=1}^{m} [y_i - f(x)]^2 \tag{A.2}$$

that is minimized when:

$$\frac{\partial S}{\partial \beta_j} = 2 \sum_{i=1} r_i \frac{\partial r_i}{\partial \beta_j} = 0 \tag{A.3}$$

The most famous modeling curve in NMR relaxation is the exponential decay, with A_0 being its amplitude, T the characteristic decay constant and y_0 an offset related to white noise, in a simple case of mono-exponential function is expressed by:

$$f(x, A, T, y_0) = A_0 \texttt{exp}^{-x/T} + y_0 \tag{A.4}$$

The Eq. A.4 converts Eq. A.1 to 3 vectors: for amplitudes A.5a, for the characteristic decay constants A.5b and for the offsets A.5c.

$$A = \begin{bmatrix} A_1 \\ A_2 \\ \vdots \\ A_n \end{bmatrix} \tag{A.5a}$$

$$T = \begin{bmatrix} T_1 \\ T_2 \\ \vdots \\ T_n \end{bmatrix} \tag{A.5b}$$

$$y_0 = \begin{bmatrix} y_{0_1} \\ y_{0_2} \\ \vdots \\ y_{0_n} \end{bmatrix} \tag{A.5c}$$

Because $^{\partial f}/_{\partial T}$ is not constant in x, modeling Eq. A.4 requires *non-linear least squares* (NLLSQ) regression to determine approximate solutions of A_{0_n}, T_n and y_{0_n}. NLLSQ regressions are usually iterative linear least squares (*LLSQ*) of an initial guess. One possibility of NLLSQ is using the Gauss-Newton algorithm, which expands Eq. A.2 until the first term of a Taylor series for each parameter β ($\beta = A, T, y_0$), iterating k times around an initial guess [121]:

$$f\left(x_i, \beta\right) \approx f\left(x_i, \beta^k\right) + \sum_j \frac{\partial f\left(x_i, \beta\right)}{\partial \beta_j}\left(\beta_j - \beta_j^k\right) \approx f\left(x_i, \beta^k\right) + \sum_j J_{ij}\Delta\beta_j \tag{A.6}$$

where J is the Jacobian. The residuals are now expressed by:

$$r_i = \Delta y_i - \sum_{s=1}^{n} J_{is}\Delta\beta_s; \Delta y_i = y_i - f\left(x_i, \beta^k\right) \tag{A.7}$$

and are minimized at the point where the gradient is zero:

$$-2\sum_{i=1}^{m} J_{ij}\left(\Delta y_i - \sum_{s=1}^{n} J_{is}\Delta\beta_s\right) = 0 \tag{A.8}$$

resulting in m normal equations ($j = 1, \ldots, m$):

$$\sum_{i=1}^{m}\sum_{s=1}^{n} J_{ij}J_{is}\Delta\beta_s = \sum_{i=1}^{m} J_{ij}\Delta y_i \tag{A.9}$$

Which can also be expressed in a matrix form:

$$\left(J^T J\right)\Delta\beta = J^T\Delta y \tag{A.10}$$

The coefficient of determination R-squared (R^2) value quantifies the goodness of the fit and is calculated as a ratio of two sums, the total sum of squares, SS_{tot}, and the residual sum of squares, SS_{res}, where $\bar{y}$ means the mean of the observed data:

$$SS_{tot} = \sum_{i=1}^{n}\left(y_i - \bar{y}\right)^2 \tag{A.11a}$$

$$SS_{res} = \sum_{i=1}^{n}\left(y_i - f_i\right)^2 \tag{A.11b}$$

$$R^2 = 1 - \frac{SS_{res}}{SS_{tot}} \tag{A.12}$$

So R^2 closes to 1 indicates good fit, when close to 0, bad ones. To avoid fake

variations coming from the degrees of freedom of the estimate of the population variance of the dependent variable ($df_{\mathtt{e}}$) and the degrees of freedom of the estimate of the underlying population error variance ($df_{\mathtt{t}}$), the coefficient adjusted R-squared ($\bar{R}^2$) is calculated:

$$\bar{R}^2 = 1 - \frac{SS_{\mathtt{res}}/df_{\mathtt{e}}}{SS_{\mathtt{tot}}/df_{\mathtt{t}}} \tag{A.13}$$

A.1.2 Examples

Two exponential decay data sets, 1 and 2, were generated with Eq. A.4 and fitted with the NLLSQ regression (Fig. A.1). The experimental and predicted parameters are present in Table A.1, which validates the method and affirms that NLLSQ brings more inaccurate results in cases of low signal-to-noise ratio.

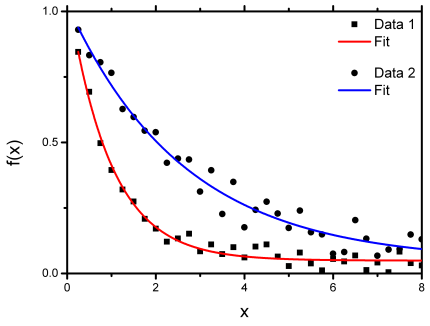

FIGURE A.1: Simulated data and NLLSQ for exponential decay data. The coefficients are present in Table A.1

TABLE A.1: Observed and predicted parameters from NLLSQ data fitting

data	variable	obs. value	pred. value	stand. error	s/n
1	y_0	0	0.049	0.006	10
1	A	1	1.04	0.04	10
1	T	1	0.96	0.05	10
1	$\bar{R}^2$		0.98238		10
2	y_0	0	0.05	0.03	5
2	A	1	0.98	0.03	5
2	T	2	2.6	0.3	5
2	$\bar{R}^2$		0.96689		5

A.2 Multi-variate data analysis

A.2.1 Theory

Nevertheless, the nowadays state of art of many spectrometers enabled acquisition of several thousand different variables in a single experiment, such as absorption in several wave-length in a optical experiment or many chemical shifts in a NMR spectrum, and no models such as Eq. A.4 can be proposed intending to reduce the number of variables. However, new statistical methods have been developed day by day, enabling variables reduction and originating what is called Chemometrics. Chemometrics was firstly defined by Kowalski: "*Chemometrics has been defined as the application of mathematical and statistical methods to chemical measurements*" [122] and currently defined by the International Chemometrics Society (ICS) by "*Chemometrics is the science of relating measurements made on a chemical system or process to the state of the system via application of mathematical or statistical methods*".

Many times the real acquired data written in Eq. A.1 does not have good distribution, which increase interpretation level of difficulty, when a careful pre-processing may be helpful. The most known pre-processing tools are mean-centering, where each variable is subtracted of its averaged value, and variance-scaling, which includes mean-centering and division by the standard deviation [123, 124].

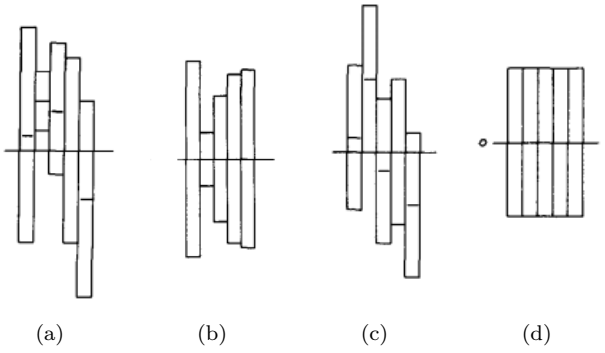

FIGURE A.2: Pre-processing of a data set, with the average in the center and its variance bar [125]. (a) Raw data. (b) Mean-centering. (c) Variance-scaling. (d) Mean-centering and variance-scaling.

There are already several chemometric methods, however two are protruded: Principal Component Regression (PCR) and Partial Least Squares (PLS). Both of them are based in Principal Component Analysis (PCA) that projects the variables to the lowest number of orthogonal axes called Principal Components (PC), in the directions of the maximum variance, and are called scores; the contribution quantity of each variable is

called loadings [125]. Linear least squares is considered one dimensional PCA, so similar approach as Eq. A.12 is used for calculating R^2.

The most common method to decompose the matrix of Eq. A.1 is the singular value decomposition (SVD, Eq. A.14), which decomposes **X** in the matrices U, S and V. The score matrix correspond to the product **U*S** and the nth column of the **V** matrix is the loadings related to the respective PCn; **S** is a diagonal matrix with the singular values [123].

$$\mathbf{X} = \mathbf{USV}^* \tag{A.14}$$

where * indicates the conjugate transpose matrix.

The PCR models use only instrumental responses **X** (Eq. A.1). PLS models taking account also the controlled variables (**Y**), relating the PCs to the maximum variance of **Y**, with the components now called latent variables (LV). The LV's are linear combinations of the PC's. For decomposing the **X** and **Y** matrices, algorithms such as NIPALS and SVD have been used [123, 125]. An important feature of PLS models is predicting some **Y** element from a previous established model.

The PLS models have several regression coefficients. Similar to PCA, it is possible to calculate a goodness of fitting, given by the explained variation of the new LV's, that might be different of the PC's, also through Eq. A.12, and now called R^2x. Other two very important coefficients regarding model performance and evolution are the goodness of fit given by the explained variation R^2y, which relates **X** to **Y**, and the goodness of prediction given by the predicted variation Q^2. They are calculated over again with the regression sum of squares, SSR (Eq. A.11a, and the residual sum of squares, RSS (Eq. A.11a, but also with the predictive residual sum of squares (PRESS):

$$PRESS = \sum_{i=1}^{n} (y_i - \hat{y})^2 \tag{A.15}$$

$$R^2y = 1 - \frac{SS_{res}}{SS_{tot}} \tag{A.16}$$

$$Q^2 = 1 - \frac{PRESS}{SS_{tot}} \tag{A.17}$$

So, without high R^2y is not possible to have high Q^2, $Q^2 > 0.9$ is considered excellent, but $Q^2 > 0.5$ indicates good model. Differences of 0.2 to 0-3 between R^2y and Q^2 implies in a presence of irrelevant model terms or few outlying data points [124].

If there is no knowledge about **Y** variables, but **X** is well distributed in classes, another directions may be more pertinent if using the class information in a discriminant analysis with LV that optimizes the class separation (discrimination), so called Partial Least Squares Discriminant Analysis (PLS-DA), a PCA-based model [124, 126]. Each class assumes a dummy variable in the **Y** matrix, which is a discrete numerical value.

Due the robustness and complexity of the involved numerical calculus, there are several chemometrics software, open source or not. For this work the software SIMCA, version 13.0, was purchased from the Umetrics company. The SIMCA algorithm has by default the code **t** for the latent variables, $\mathbf{c_a}$ for the Y-weights, $\mathbf{u_a}$ for the score vector and $\mathbf{w_a^*}$ for the X-weights directly related to the X-matrix, so the plot $\mathbf{w^*c_a}$ indicates the weight plot, i.e., the loadings.

A.2.2 Examples

Several set of 4×10 mono and bi-exponential decay data, differing in amplitude A or decay constant T, were simulated with spacing of 0.05, amplitude-to-noise ratio of 7 and insert in a chemometrics matrix. After pre-processig by mean-centering, the PLS models resulted in the score and loading graphs present at Fig. A.3, with the latent variable LV coefficients indicated in Table A.2 (norm. means that the decays were normalized by the maximum value):

Table A.2: Simulated chemometrics models with exponential decays

model	exponential	A_1	T_1	A_2	T_2	Y	LV1		LV2	
							R^2	Q^2	R^2	Q^2
M_1	mono (norm.)	0.1 to 1	1			A_1	0	0		
M_2	mono	0.1 to 1	1			A_1	0.998	0.997	0.999	0.998
M_3	mono	1	0.1 to 1			T_1	0.973	0.971	0.993	0.982
M_4	bi (norm.)	0.1 to 1	0.4	0.3	1	A_1	0.994	0.994	0.999	0.993
M_5	bi	0.7	0.1 to 1	0.3	1	T_1	0.964	0.956	0.994	0.972

The model M1, where changes only in the signal-to-noise ratio of the CPMG decay were simulated (due normalization), no model could be fitted. Similar data where explored in the model M2, but without normalization, so this model represents several decays with equal relaxation time, however different amplitude. The M2 PLS model was very useful to separate the different amplitude decays (Fig. A.3(a)), being the LV1 the main latent variable, represented by a curve with decay constant approximately equal to the relaxation time, and LV2 associated only with noise (Fig. A.3(b)).

The data inserted in model M3 had good separation thought the PLS model making groups as present in Fig. A.3(c). The variations in relaxation time of a mono-exponential decay resulted in LV1 with loadings maximized in the time 0.3 ms, as present

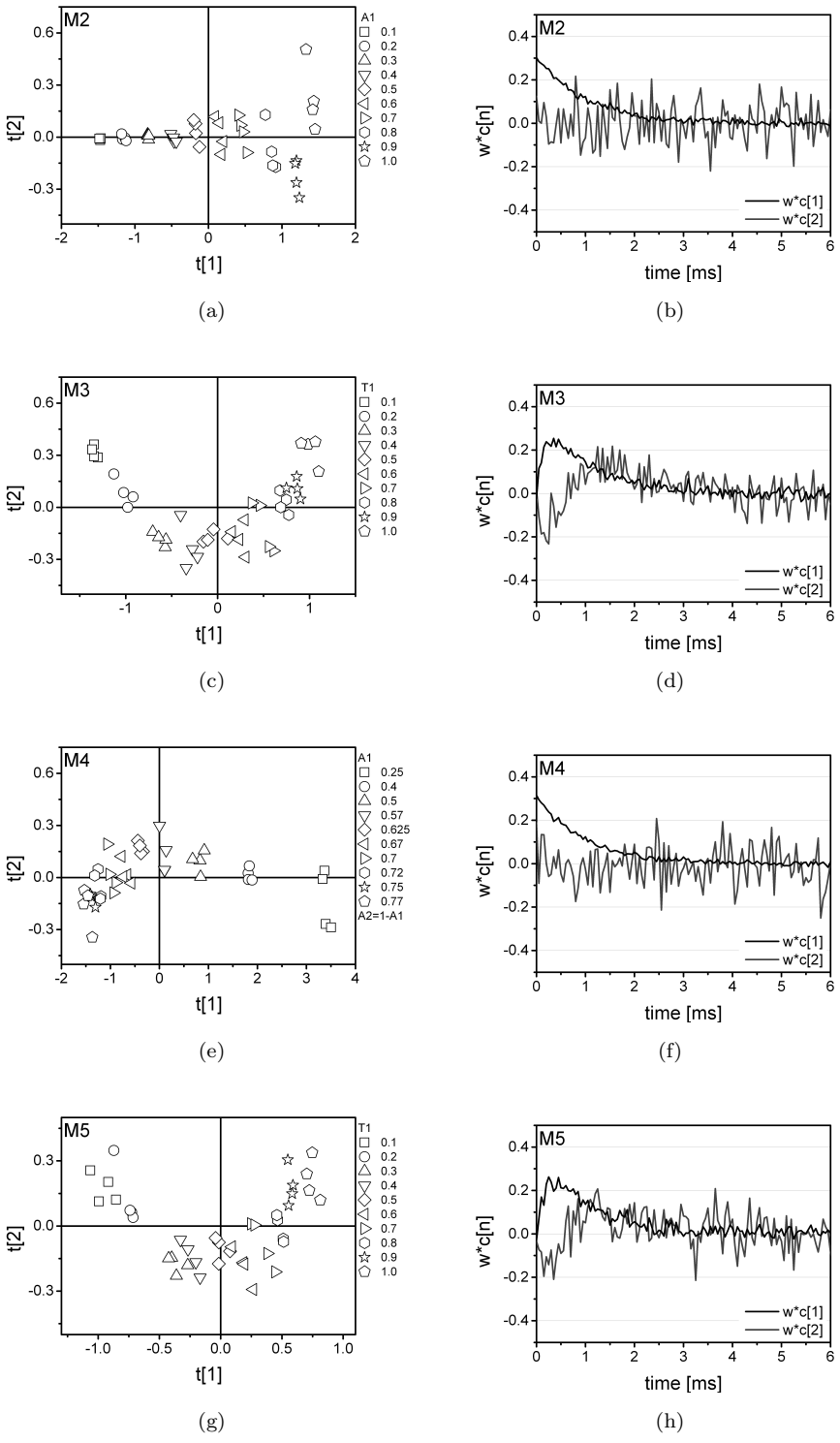

FIGURE A.3: Chemometrics models with exponential decays. (a) M2 score. (b) M2 loading. (c) M3 score. (d) M3 loading. (e) M4 score. (f) M4 loading. (g) M5 score. (h) M5 loading.

in Fig. A.3(d); although LV2 has small significance, it has opposite variance for the short relaxation times, and positive variance for the longer ones, what may be an dead time effect. Changes in the amplitude of one component of a bi-exponential decay, as present in M4, leads to similar understanding as in M2, as shown in Fig. A.3(e), even thought the LV1 now has scope proportional to both relaxation times; LV2 is still noise (Fig. A.3(f)). On the other hand, changes in a relaxation time of only one component of a bi-exponential decay, as performed in M5 leads to results similar the model M3, as can be seen in the scores (Fig. A.3(g)) and loading plots (Fig. A.3(h)), with similar conclusions.

The simulated data evaluated by PLS, as present in Fig. A.3, evidence that MVDA is a powerful tool to analyze decay data as the ones acquired in a relaxation experiment: it is able to separate exponential decays by amplitude and relaxation time. All of the cases the latent variable LV1 explains more than 97% of the variability, and in few cases LV2 added some more explanation. In experimental cases (as several present in Chapter 4) the LVs varies more due to the presence of higher noise.

Bibliography

[1] W. Gerlach and O. Stern. Das magnetische Moment des Silberatoms. *Zeitschrift fuer Physik*, 9(1):353–355, 4 1922.

[2] F. Bloch, W. W. Hansen, and M. Packard. The Nuclear Induction Experiment. *Physical Review*, 70(7–8):474–485, 7 1946.

[3] E. M. Purcell, H. C. Torrey, and R. V. Pound. Resonance Absorption by Nuclear Magnetic Moments in a Solid. *Physical Review*, 69(69):37–38, 7 1946.

[4] J. A. Jackson, L. J. Burnett, and J. F. Harmon. Remote (Inside-Out) NMR. III. Detection of Nuclear Magnetic Resonance in a Remotely Produced Region of Homogeneous Magnetic Field. *Journal of Magnetic Resonance*, 41(3):411–421, 12 1980.

[5] Bernhard Bluemich. The Incredible Shrinking Scanner: MRI-like Machine Becomes Portable [preview]. *Scientific American*, 299:92–98, 11 2008.

[6] G. Eidman, R. Savelsberg, P. Bluemler, and B. Bluemich. The NMR MOUSE, a Mobile Universal Surface Explorer. *Journal of Magnetic Resonance, Series A*, 122:104–109, 1996.

[7] M. D. Huerlimann and D. D. Griffin. Spin Dynamics of Carr– Purcell– Meiboom–Gill-like Sequences in Grossly Inhomogeneous B0 and B1 Fields and Application to NMR Well Logging. *Journal of Magnetic Resonance*, 143:120–135, 2000.

[8] J. Perlo, F. Casanova, and B. Bluemich. Profiles with Microscopic Resolution by Single-Sided NMR. *Berichte der deutschen chemischen Gesellschaft (A and B Series)*, 53(6):1073–1085, 6 1920.

[9] J. Perlo, F. Casanova, and B. Bluemich. Single-Sided Sensor for High-Resolution NMR Spectroscopy. *Journal of Magnetic Resonance*, 180:274–279, 2006.

[10] F. Casanova and B. Bluemich. Two-Dimensional Imaging with a Single-Sided NMR Probe. *Journal of Magnetic Resonance*, 163:38–45, 2003.

[11] C. Hedesiu, D. E. Demco, R. Kleppinger, A. Buda, B. Bluemich, K. Remerie, and V. M. Litvinov. The Effect of Temperature and Annealing on the Phase Composition, Molecular Mobility and the Thickness of Domains in High-Density Polyethylene. *Polymer*, 48(3):763–777, 2007.

[12] A. Adams and B. Blümich. Single-Sided NMR of Semicrystalline Polymers. *Macromolecular Symposia*, 327(1):29–38, 06 2013.

[13] D. Capitani, V. Di Tullio, and N. Proietti. Nuclear Magnetic Resonance to Characterize and Monitor Cultural Heritage. *Progress in Nuclear Magnetic Resonance Spectroscopy*, 64:29–69, 7 2012.

[14] F. Presciutti, J. Perlo, F. Casanova, S. Gloeggler, C. Miliani, B. Bluemich, B. G. Brunetti, and A. Sgamellotti. Noninvasive Nuclear Magnetic Resonance Profiling of Painting Layers. *Applied Physics Letters*, 93:033505, 2008.

[15] B. Bluemich, A. Haber, F. Casanova, E. Del Federico, V. Boardman, G. Wahl, and L. Isolani A. Stilliano. Noninvasive Depth Profiling of Walls by Portable Nuclear Magnetic Resonance. *Analytical and Bioanalytical Chemistry*, 397(7):3117–3125, 8 2010.

[16] F. Presciutti, J. Perlo, F. Casanova, S. Gloeggler, C. Miliani, B. Bluemich, B. G. Brunetti, and A. Sgamellotti. Noninvasive Testing of Art and Cultural Heritage by Mobile NMR. *Accounts of chemical research*, 43(6):761–770, 3 2010.

[17] V. Di Tullio, N. Proietti, D. Capitani, I. Nicolini, and A. M. Mecchi. NMR Depth Profiles as a Non-invasive Analytical Tool to Probe the Penetration Depth of Hydrophobic Treatments and Inhomogeneities in Treated Porous Stones. *Analytical and Bioanalytical Chemistry*, 400(9):3151–3164, 9 2011.

[18] B. Bluemich, S. Anferova, S. Sharma, A. L. Segre, and C. Federici. Degradation of Historical Paper: Nondestructive Analysis by the NMR-MOUSE. *Journal of Magnetic Resonance*, 161(2):204 – 209, 2003.

[19] N. Proietti, D. Capitani, E. Pedemonte, B. Blümich, and A.L. Segre. Monitoring Degradation in Paper: Non-invasive Analysis by Unilateral NMR. Part {II}. *Journal of Magnetic Resonance*, 170(1):113 – 120, 2004.

[20] E. Del Federico, S. A. Centeno, C. Kehlet, P. Currier, D. Stockman, and A. Jerschow. Unilateral NMR Applied to the Conservation of Works of Art. *Analytical and Bioanalytical Chemistry*, 396(1):213–220, 9 2010.

[21] E. Badea, L. Miu, P. Budrugeac, M. Giurginca, A. Masic, N. Badea, and G. D. Gatta. Study of Deterioration of Historical Parchments by Various Thermal Analysis Techniques Complemented by SEM, FTIR, UV-VIS-NIR and Unilateral NMR Investigations. *Journal of Thermal Analysis and Calorimetry*, 91(1):17–27, 2008.

[22] A. Masic, M. R. Chierotti, R. Gobetto, G. Martra, I. Rabin, and S. Coluccia. Solid-State and Unilateral NMR Study of Deterioration of a Dead Sea Scroll Fragment. *Analytical and Bioanalytical Chemistry*, 402(4):1551–1557, 2012.

[23] E. Del Federico, S. A. Centeno, C. Kehlet, K. Ulrich, A. Yamazaki-Kleps, and A. Jerschow. In Situ Unilateral ^{1}H-NMR Studies of the Interaction Between Lead White Pigments and Collagen-Based Binders. *Applied Magnetic Resonance*, 42(3): 363–376, 4 2012.

[24] B. Bluemich, S. Anferova, R. Pechnig, H. Pape, J. Arnold, and C. Clauser. Mobile NMR for Porosity Analysis of Drill Core Sections. *Journal of Geophysics and Engineering*, 1(3):177–180, 8 2004.

[25] V. Bortolotti, M. Camaiti, C. Casieri, F. De Luca, P. Fantazzini, and C. Terenzi. Water Absorption Kinetics in Different Wettability Conditions Studied at Pore and Sample Scales in Porous Media by NMR with Portable Single-Sided and Laboratory Imaging Devices. *Journal of Magnetic Resonance*, 181(2):287–295, 6 2006.

[26] N. Proietti, D. Capitani, S. Cozzolino, M. Valentini, E. Pedemonte, E. Princi, S. Vicini, and A. L. Segre. In Situ and Frontal Polymerization for the Consolidation of Porous Stones: A Unilateral NMR and Magnetic Resonance Imaging Study. *The Journal of Physical Chemistry B*, 110(47):23719–28, 11 2006.

[27] V. D. Tullio, N. Proietti, D. Capitani, I. Nicolini, and A. M. Mecchi. NMR Depth Profiles as a Non-invasive Analytical Tool to Probe the Penetration Depth of Hydrophobic Treatments and Inhomogeneities in Treated Porous Stones. *Analytical and Bioanalytical Chemistry*, 400(9):3151–64, 7 2011.

[28] F. J. Ruhi, T. Boni, J. Perlo, F. Casanova, M. Baias, E. Egarter, and B. Blumich. Non-Invasive Spatial Tissue Discrimination in Ancient Mummies and Bones in situ by Portable Nuclear Magnetic Resonance. *Journal of Cultural Heritage*, 8(3): 257–263, 7-9 2007.

[29] W. Pauli jr. Ueber den Zusammenhang des Abschlusses der Elektronen-gruppen im Atom mit der Komplexstruktur der Spektren. *Zeitschrift fuer Physik*, 31(1): 765–783, 1 1925.

[30] J. M. Kellogg, N.F. Ramsey I. I. Rabi, and J. R. Zacharias. The Magnetic Moments of the Proton and the Deuteron the Radiofrequency Spectrum of H2 in Various Magnetic Fields. *Physical Review*, 56(8):728–743, 10 1939.

[31] W. C. Dickinson. Dependence of the F19 Nuclear Resonance Position on Chemical Compound. *Physical Review*, 77(5):736–737, 3 1950.

[32] G. Proctor and F. C. Yu. The Dependence of a Nuclear Magnetic Resonance Frequency upon Chemical Compound. *Physical Review*, 77(5):717, 5 1950.

[33] R. R. Ernst and W. A. Anderson. Application of Fourier Transform Spectroscopy to Magnetic Resonance. *Review of Scientific Instruments*, 37(1):93–102, 1 1966.

[34] Kurt Wuethrich. *NMR of Proteins and Nucleic Acids*. Wiley, New Jersey, 1st edition, 1986.

[35] P. C. Lauterbur. Image Formation by Induced Local Interactions: Examples Employing Nuclear Magnetic Resonance. *Nature*, 242:190–191, 3 1973.

[36] J. Kaerger P. Fantazzini, V. Bortolotti and P. Galvosas. *Magnetic Resonance in Porous Media: Proceedings of the 10th International Bologna Conference on Magnetic Resonance in Porous Media (MRPM10), Including the 10th Colloquium on Mobile Magnetic Resonance (CMMR10)*. AIP Conference Proceedings / Materials Physics and Applications. American Inst. of Physics, 2011.

[37] A. Abragam. *Principles of Nuclear Magnetism*. International Series of Monographs on Physics. Oxford University Press, 1983.

[38] C. P. Slichter. *Principles of Magnetic Resonance*. Springer Series in Solid-State Sciences. Springer, 1990.

[39] N. Bloembergen, E. M. Purcell, and R. V. Pound. Relaxation Effects in Nuclear Magnetic Resonance Absorption. *Physical Review*, 73(7):679–712, 4 1948.

[40] P. Mansfield and P. G. Morris. *NMR Imaging in Biomedicine*. Advances in magnetic resonance: Supplement. Academic Press, 1982.

[41] H. Y. Carr and E. M. Purcell. Effects of Diffusion on Free Precession in Nuclear Magnetic Resonance Experiments. *Physical Review*, 94(3):630–638, 5 1954.

[42] S. Meiboom and D. Gill. Modified Spin-Echo Method for Measuring Nuclear Relaxation Times. *The Review of Scientific Instruments*, 29(8):688–691, 8 1958.

[43] E. D. Ostroff and J. S. Waugh. Multiple Spin Echoes and Spin Locking in Solids. *Physical Review Letters*, 16(24):1097–1098, 6 1966.

[44] R. L. Vold, J. S. Waugh, M. P. Klein, and D. E. Phelps. Measurement of Spin Relaxation in Complex Systems. *The Journal of Chemical Physics*, 48:3831–3832, 1968.

[45] J. L. Markley, W. J. Horsley, and M. P. Klein. Spin-Lattice Relaxation Measurements in Slowly Relaxing Complex Spectra. *The Journal of Chemical Physics*, 55 (7):3604–3605, 10 1971.

[46] E. L. Hahn. Spin Echoes. *Physical Review*, 80(4):580–594, 11 1950.

[47] J. G. Powles and J. H. Strange. Measurement of J Coupling Using Spin Echo Techniques. *Discussions of the Faraday Society*, 34:30–37, 1962.

[48] F. Casanova, J. Perlo, and B. Bluemich. *Single-Sided NMR*. Springer, 2011.

[49] J. H. Lee, C. Labadie, C. S. Springer, and G. S. Harbison. Two-Dimensional Inverse Laplace Transform NMR: Altered Relaxation Times Allow Detection of Exchange Correlation. *Journal of the American Chemical Society*, 115:7761–7764, 1993.

[50] J. H. Lee, C. Labadie, C. S. Springer, and G. S. Harbison. Quantitative Two-Dimensional Time Correlation Relaxometry. *Magnetic Resonance in Medicine*, 22 (2):425–434, 1991.

[51] S. W. Provencher. COTIN: A General Purpose Constrained Regularization Program for Inverting Noisy Linear Algebraic and Integral Equations. *Computer Physics Communications*, 27:229–242, 1982.

[52] G. C. Borgia, R. J. S. Brown, and P. Fantazzini. Uniform-Penalty Inversion of Multiexponential Decay Data. *Journal of Magnetic Resonance*, 132:65–77, 1998.

[53] P. T. Callaghan, C. H. Arnsb, P. Galvosas, M. W. Hunter, Y. Qiao, and K. E. Washburn. Recent Fourier and Laplace Perspectives for Multidimensional NMR in Porous Media. *Magnetic Resonance Imaging*, 25:441–444, 2007.

[54] Y. Q. Song, L. Venkataramanan, M. D. Huerlimann, M. Flaum, P. Frulla, and C. Straley. T1–T2 Correlation Spectra Obtained Using a Fast Two-Dimensional Laplace Inversion. *Journal of Magnetic Resonance*, 154:261–268, 2002.

[55] K. E. Washburn and P. T. Callaghan. Tracking Pore to Pore Exchange Using Relaxation Exchange Spectroscopy. *Physical Review Letters*, 97(17):175502, 2006.

[56] L. Venkataramanan, Y. Q. Song, and M. D. Huerlimann. Solving Fredholm Integrals of the First Kind with Tensor Product Structure in 2 and 2.5 Dimensions. *IEEE Transactions on Signal Processing*, 50(5):1017–1026, 5 2002.

[57] P. J. McDonald. Stray Field Magnetic Resonance Imaging. *Progress rn Nuclear Magnetic Resonance Spectroscopy*, 30(1):69–99, 3 1997.

[58] A. T. Watson and C.T. P. Chang. Characterizing Porous Media with NMR Methods. *Progress in Nuclear Magnetic Resonance Spectroscopy*, 31(4):343–386, 11 1997.

[59] H. Staudinger. Ueber Polymerisation. *Journal of Magnetic Resonance*, 176:64–70, 2005.

[60] H. Ishida and G. Kumar. *Molecular Characterization of Composite Interfaces*. Polymer Science and Technology Series. Springer, 1985.

[61] K. Ziegler. Neue Entwicklungen der Metallorganischen Synthese. *Angewandte Chemie*, 68(23):721—724, 1956.

[62] B. Wunderlich. *Thermal Analysis of Polymeric Materials*. Springer, 2005.

[63] R. Stakenborghs. New Method to Detect Cold Fusion Joints in High Density Polyethylene Pipe. *Evisive*.

[64] P. Barber and J. R. Atkinson. Some Microstructural Features of the Welds in Butt-Welded Polyethylene and Polybutene-I Pipes. *Journal of Materials Science*, 7(10):1131–1136, 10 1972.

[65] E. Rutherford. Uranium Radiation and the Electrical Conduction Produced by it. *Philosophical Magazine*, 47:109, 01 1899.

[66] Donald Pavia, Gary M. Lampman, George Kriz, and James A. Vyvyan. *Introduction to Spectroscopy*. International student edition. Brooks/Cole, Cengage Learning, 2009.

[67] F. A. Rueggeberg. State-of-the-art: Dental Photocuring—A Review. *Dental Materials*, 27(1):39–52, 01 2001.

[68] N. Moszner and U. Salz. New developments of polymeric dental composites. *Progress in Polymer Science*, 26(4):535–576, 05 2001.

[69] L. G. Lovell, K. A. Berchtold, J. E. Elliott, H. Lu, and C. N. Bowman. Understanding the Kinetics and Network Formation of Dimethacrylate Dental Resins. *Polymers for Advanced Technologies*, 12(6):335–345, 01 2011.

[70] Y. C. Chen, J. L. Ferracane, and S. A. Prahl. A Pilot Study of a Simple Photon Migration Model for Predicting Depth of Cure in Dental Composite. *Dental Materials*, 21(11):1075–1086, 11 2005.

[71] D. C. Watts and A. J. Cash. Determination of Polymerization Shrinkage Kinetics in Visible-Light-Cured Materials: Methods Development. *Dental Materials*, 7(4): 281–287, 10 1991.

[72] D. C. Watts. Reaction Kinetics and Mechanics in Photo-Polymerised Networks. *Dental Materials*, 21(1):27–35, 01 2005.

[73] I. Sideridou, V. Tserki, and G. Papanastasiou. Effect of Chemical Structure on Degree of Conversion in Light-Cured Dimethacrylate-Based Dental Resins. *Biomaterials*, 23(8):1819–1829, 04 2002.

[74] L. Musanje, J. L. Ferracane, and R.L. Sakaguchi. Determination of the Optimal Photoinitiator Concentration in Dental Composites Based on Essential Material Properties. *Dental Materials*, 25(8):994–1000, 08 2009.

[75] J. L. Ferracane, P. Aday, H. Matsumoto, and V. A. Marker. Relationship Between Shade and Depth of Cure for Light-Activated Dental Composite Resins. *Dental Materials*, 2(2):80–84, 04 1986.

[76] R.B.T. Price, C.A. Felix, and P. Andreou. Knoop Hardness of Ten Resin Composites Irradiated with High-Power LED and Quartz-Tungsten-Halogen Lights. *Biomaterials*, 26(15):2631–2641, 05 2005.

[77] J. Vaidyanathan, T.K. Vaidyanathan, Y. Wang, and T. Viswanadhan. Thermoanalytical Characterization of Visible Light Cure Dental Composites. *Journal of Oral Rehabilitation*, 19(1):49–69, 01 1992.

[78] D. C. Watts and A. S. Marouf. Optimal Specimen Geometry in Bonded-disk Shrinkage-strain Measurements on Light-cured Biomaterials. *Dental Materials*, 16(6):447–451, 11 2000.

[79] J.R. Condon and J.L. Ferracane. Assessing the Effect of Composite Formulation on Polymerization Streess. *The Journal of the American Dental Association*, 131 (4):497–503, 04 2000.

[80] M. Cadenaro, M. Biasotto, N. Scuor, L. Breschi, C.L. Davidson, and R. Di Lenarda. Assessment of Polymerization Contraction Stress of Three Composite Resins. *Dental Materials*, 24(5):681–685, 05 2008.

[81] M. Rosentritt, A.C. Shortall, and W.M. Palin. Dynamic Monitoring of Curing Photoactive Resins: A Methods Comparison. *Dental Materials*, 26(6):565–570, 06 2010.

[82] J. Steinhaus, B. Moeginger, M. Grossgarten, and B. Hausnerova. Evaluation of Dielectric Curing Monitoring Investigating Light-Curing Dental Filling Composites. *Materials Engineering*, 18:30–35, 05 2011.

[83] V. Litvinov and A. A. Dias. Real-Time NMR. How Fast Can We Do It? *Macromolecular Symposia*, 230(1):20–25, 12 2005.

[84] J.M.G. Cowie and V. Arrighi. *Polymers: Chemistry and Physics of Modern Materials*. CRC Press, 2007.

[85] P.C. Hiemenz and T. P. Lodge. *Polymer Chemistry*. CRC Press, 2007.

[86] F. Kohlrausch. Ueber die Elastische Nachwirkung bei der Torsion. *Annalen der Physik*, 195(7):337–368, 1863.

[87] R. Kohlrausch. Theorie des Elektrischen Rückstandes in der Leidener Flasche. *Annalen der Physik*, 167(1):56–82, 1854.

[88] G. W. Scherer and G. S. Wheeler. Silicate Consolidants for Stone. *Key Engineering Materials*, 391:1–25, 10 2009.

[89] R. Giorgi, M. Ambrosi, N. Toccafondi, and P. Baglionii. Nanoparticles for Cultural Heritage Conservation: Calcium and Barium Hydroxide Nanoparticles for Wall Painting Consolidation. *Chemistry - A European Journal*, 16(31):9374–9382, 8 2010.

[90] N. Agnew and M. Demas. *Principles for the Conservation of Heritage Sites in China*. The Getty Conservation Institute, 2004.

[91] M. Ambrosi, L. Dei, R. Giorgi, C. Neto, and P. Baglioni. Colloidal Particles of ca(oh)2: Properties and Applications to Restoration of Frescoes. *Langmuir*, 17: 4251–4255, 2001.

[92] J. H. Larson, C. Madden, and I. Sutherland. Ince Blundell: the Preservation of an Important Collection of Classical Sculpture. *Journal of Cultural Heritage*, 1: 79–87, 2000.

[93] J. H. Larson, C. Madden, and I. Sutherland. Effects of Hydrophobic Treatments of Stone on Pore Water Studied by Continuous Distribution Analysis of NMR Relaxation Times. *Magnetic Resonance Imaging*, 19:509–512, 2001.

[94] N. Proietti, D. Capitani, S. Cozzolino, M. Valentini, E. Pedemonte, E. Princi, S. Vicini, and A. L. Segre. In Situ and Frontal Polymerization for the Consolidation of Porous Stones: A Unilateral NMR and Magnetic Resonance Imaging Study. *The Journal of Physical Chemistry*, 110:23719–23728, 9 2006.

[95] L. Huizhi, L. Hong, and X. Yinghui. Study on Modification of Calcium Hydroxide with Isopropanol. *Inorganic Chemical Industry*, 9(0):12, 2008.

[96] P. Baglioni and R. Giorgi. Soft and Hard Nanomaterials for Restoration and Conservation of Cultural Heritage. *Soft Matter*, 2:293–303, 2 2006.

[97] L. Dei and B. Salvadori. Nanotechnology in Cultural Heritage Conservation: Nanometric Slaked Lime Saves Architectonic and Artistic Surfaces from Decay. *Journal of Cultural Heritage*, 7(2):110–115, 4-6 2006.

[98] F. Presciutti, D. Capitani, A. Sgamellotti, B. G. Brunetti, F. Costantino, S. Viel, and A. Segre. Electron Paramagnetic Resonance, Scanning Electron Microscopy with Energy Dispersion X-ray Spectrometry, X-ray Powder Diffraction, and NMR Characterization of Iron-rich Fired Clays. *The Journal of Physical Chemistry B*, 109(47):22147–22158, 12 2005.

[99] L. Frydman and J. S. Harwood. Isotropic Spectra of Half-Integer Quadrupolar Spins from Bidimensional Magic-Angle Spinning NMR. *Journal of the American Chemical Society*, 117(19):5367–5368, 05 1995.

[100] C Fernandez and J. P. Amoureux. Triple-Quantum MAS-NMR of Quadrupolar Nuclei. *Solid State Nuclear Magnetic Resonance*, 5(4):315–321, 01 1996.

[101] L. Pel, K. Kopingaj, G. Bertram, and G. Lang. Water absorption in a fired-clay brick observed by nmr scanning. *Journal of Physics D: Applied Physics*, 28(4): 675–680, 04 1995.

[102] C. Casieri an C. Terenzi and F. De Luca. Two-dimensional Longitudinal and Transverse Relaxation Time Correlation as a Low-resolution Nuclear Magnetic Resonance Characterization of Ancient Ceramics. *Journal of Applied Physics*, 105 (3):034901, 02 2009.

[103] C. Terenzia, C. Casierib, A. C. Felicid, Mario Piacentini, M. Vendittellid, and F. De Luca. Characterization of Elemental and Firing-Dependent Properties of Phlegrean Ceramics by Non-destructive ED-XRF and NMR Techniques. *Journal of Archaeological Science*, 37(7):1403–1412, 07 2010.

[104] V. Tudisca, C. Casieri, F. Demma, M. Diazd, L. Pinole, C. Terenzia, and F. De Luca. Firing Technique Characterization of Black-Slipped Pottery in Praeneste by Low Field 2D NMR Relaxometry. *Journal of Archaeological Science*, 38(2): 352–359, 02 2011.

[105] D. McKitterick. *Print, Manuscript and the Search for Order, 1450-1830*. Cambridge University Press, 2005.

[106] A. Masic, L. Bertinetti, R Schuetz, L. Galvis, N. Timofeeva, J. W. C. Dunlop, J. Seto, M. A. Hartmann, and P. Fratzl. Observations of Multiscale, Stress-Induced Changes of Collagen Orientation in Tendon by Polarized Raman Spectroscopy. *Bio Macromolecules*, 12(11):3989–3996, 2011.

[107] C. J. Kennedy and T. J. WESS. The Structure of Collagen within Parchment – A Review. *Restaurator*, 24(2):61–80, 2003.

[108] A . E. Aliev. Solid-State NMR Studies of Collagen-Based Parchments and Gelatin. *Biopolymers*, 77(4):230–245, 2005.

[109] R. Larsen. *Improved Damage Assessment of Parchment*. Assessment, data collection and sharing of knowledge. European Communities, 2007.

[110] D. Capitani, A. L. SEGRE, D. Attanasio, B. Blicharska, B. Focher, and G. Capretti. ^{1}H NMR Relaxation Study of Paper as a System of Cellulose and Water. *Tappi Journal*, 79(6):113–122, 1996.

[111] D. Capitani, M. C. Emanuele, A. L. Segre J. Bella, D. Attanasio, B. Focher, and G. Capretti. ^{1}H NMR Relaxation Study of Cellulose and Water Interaction in Paper. *Tappi Journal*, 82(9):117–124, 1999.

[112] D. Capitani, N. Proietti, F. Ziarelli, and A. L. Segre. NMR Study of Water-Filled Pores in One of the Most Widely Used Polymeric Material: The Paper. *Macromolecules*, 35(14):5536–5543, 06 2002.

[113] D. Attanasio, D. Capitani, C. Federici, M. Paci, and A. L. Segrei. Electron Paramagnetic Resonance and ^{1}H and ^{13}C NMR Study of Paper. *ACS Symposium Series*, 598:333–353, 05 1995.

[114] 2012 Magritek. Nmr-mouse specifications, 10 2013. URL `http://www.magritek.com/products-nmr-mouse-specifications`.

[115] 2013 Bruker Corporation. the minispec mq series, 10 2013. URL `http://www.bruker.com/products/mr/td-nmr/minispec-mq-series.html`.

[116] 2012 Magritek. Kea specifications, 10 2013. URL `http://www.magritek.com/products-kea-specifications`.

[117] E. Fukushima and S. B. W. Roeder. *Experimental Pulse NMR: A Nuts and Bolts Approach*. Westview Press, 1993.

[118] A. Masic. *Applicazione di Tecniche Innivative nello Studio dei Processi di Degrado dei Manufatti di Interesse Artistico-Culturale*. Dipartimento Di Chimica. Universita Degli Studi Di Torino, 2005.

[119] S. Herbert Y. Lu, D. M. Shinozaki. Inhomogeneous deformation in welded high density polyethylene. *Journal of Applied Polymer Science*, 86(1):43–52, 10 2002.

[120] F. Zhang, Y. Gong, and T. He. Multiple Melting Behavior of Isotactic Polypropylene and Poly(propylene-co-ethylene) after Stepwise Isothermal Crystallization. *European Polymer Journal*, 39(12):2315–2322, 12 2003.

[121] E. Reis. *Estatistica Descritiva*. Edicoes Silabo, 2008.

[122] B. R. Kowalski. Chemometrics. *Analytical Chemistry*, 52(5):112R–122R, 04 1980.

[123] M. S. Melgo e P. L. O. Volpe M. M. C. Ferreira, A. M. Antunes. Quimiometria i: Calibracao Multivariada, Um Tutorial. *Química Nova*, 22(5):724 – 731, 09 1999.

[124] L. Eriksson, E. Johansson, N. Kettaneh-Wold, J. Trygg, C. Wikstrom, and S. Wold. *Multivariate and Megavariate Data Analysis Basic Principles and Applications (Part I)*. Umetrics, 2006.

[125] P. Geladi and B. R. Kowalski. Partial Least-Squares Regression: a Tutorial. *Analytica Chimica Acta*, 185:1–17, 1986.

[126] L. Stahle and S. Wold. Partial Least Squares Analysis with Cross-Validation for the Two-class Problem: A Monte Carlo Study. *Journal of Chemometrics*, 1(3): 185–196, 07 1987.

List of Figures

List of Tables

Acknowledgements

It was not an easy task to remember and recognize everyone who provided me with this amazing opportunity to live a big part of my life in Europe. In the year 2009, I was 22 and found myself like a kid, not knowing the unknown world outside my dear hometown. After this long journey, I am 27, and feel that this time has not only improved my scientific skills, but also developed me as person, opening doors to my future. Afraid of forgetting someone, I would like to acknowledge and thank:

- The Brazilian National Council of Technological and Scientific Development (*Conselho Nacional de Desenvolvimento Científico e Tecnológico* - **CNPq**) for financially supporting this work through the process number 290010/2009-8. Beyond that, I also point out its tireless efforts to promote and improve scientific research in Brazil.

- No less important than CNPq, the German Academic Exchange Service (*Deutscher Akademischer Austauschdienst* - **DAAD**) for all the attention during the selection process, the amazing time in Mannheim and all the support during the PhD time. I do not forget the kindness and helpfulness of Mrs. **Rebeca Mendonça** from DAAD-Rio de Janeiro;

- Nothing would have been possible without Prof. Dr. **Bernhard Blümich** accepting me and allowing me to work in the best laboratory for low field NMR in the world. Also, his motivation and influence, together with his intelligence and culture, were fundamental to the realization of this work;

- The co-authors' participation in the respective subjects: Dr. **Josefina Perlo** (pipes); M.Sc. **Johannes Steinhaus** and his supervisor, Prof. Dr. **Bernhard Möginger** (dental resins); Prof. Dr. **Hua Zhou** (sandstones, handmade papers); Prof. Dr. **Mihai Vasilescu** (pottery); Mrs. **Sarah Turnhoff** (canvas).

- Acting as more than just a supervisor in my Master's work, Dr. **Luiz Alberto Colnago** has shown me a friend and an example of a researcher and person to follow;

- The classes taken at the Instituto de Física de São Carlos (**IFSC - USP**) prepared me to start this challenge, so every single teacher is here acknowledge and I emphasize the useful advice of and fruitful discussions with Prof. Dr. **Vanderlei Salvador Bagnato**;

- My first contact with Prof. Blümich's NMR group, made by Prof. Dr. **Daniel Pusiol** and Dr. **Federico Casanova**, is also acknowledged. It was a pleasure to absorb some of Federico's huge experience in NMR sensors;

- To M.Sc. **Fabio Lamon Sofri**, from **Braskem S.A.**, acknowledgment for accepting me as part of the Polymer Science Team, trusting in my skills and assisting in my repatriation; Moreover, I thank everybody in the Technology and Innovation Center of Braskem (RS - Brazil) for the warm reception.

- I thank my **friends at MC** for being in touch during these 4 years, sharing friendship and some of their skills. I would emphasize the Brazilians, Dr. **Mario Killner** and Mr. **Geovanni Dal-Ri Junior** and my new friends of the last year, M.Sc. **Yadollah Teymouri** and M.Sc. **Kawarpal Singh**;

- Of central importance are the friendships realized outside the ITMC, either with **foreigners** or **Brazilian exchange students**; names are omitted as they are more than a hundred;

- My personal friends at University of São Paulo, emphasizing M.Sc. **Sebastião Pratavieira**, M.Sc. **Anderson Silva Chaves** and the physics students of the year 2004 and "neighbors" who always provided me an excellent environment to learn, discuss and produce;

- I could not forget the staff of the **Doces Marchi** Company that taught me several points of life that we do not learn in books;

- Last but not least I would like to acknowledge **my family**, every single individual, my sweet **mother** (Valderez Marchi) and my dear **father** (Waldecir Marchi), my lovely **sisters** (Vanessa Marchi and Viviani Marchi), my admirable **uncles** (Walter Bagnato, Vanderley Bagnato and Walter Marchi) and **aunts** (Wilma Marchi, Wilneide Marchi, Wirley Marchi and Wilcerley Marchi) as well as my wonderful **cousins** (long list *sic*) and my loving **grandparent**s (Antonio and Zuleika Marchi, Walter and Antonia Bagnato, *in memoriam*), and the **true long-time friends** (another long list *sic*), for giving all the needed support, for trusting in me and making each visit home the best moments of my life abroad;

Muito Obrigado!